

The Skyrme Interaction in finite nuclei and nuclear matter

J. R. Stone^{1,2,3} and P.-G. Reinhard^{4,5}

¹ Department of Physics, University Oxford,
Oxford OX1 3PU / United Kingdom

² Physics Division, Oak Ridge National Laboratory,
P.O. Box 2008, Oak Ridge, TN 37831, USA

³ Department of Chemistry and Biochemistry,
University of Maryland, College Park, MD 20742, USA

⁴ Institut für Theoretische Physik, Universität Erlangen,
D-91054 Erlangen, Germany

⁵ Joint Institute for Heavy Ion Research, Oak Ridge National Laboratory,
P. O. Box 2008, Oak Ridge, TN 37831, USA

Abstract

Self-consistent mean-field models are a powerful tool in the investigation of nuclear structure and low-energy dynamics. They are based on effective energy-density functionals, often formulated in terms of effective density-dependent nucleon-nucleon interactions. The free parameters of the functional are adjusted to empirical data. A proper choice of these parameters requires a comprehensive set of constraints covering experimental data on finite nuclei, concerning static as well as dynamical properties, empirical characteristics of nuclear matter, and observational information on nucleosynthesis, neutron stars and supernovae. This work aims at a comprehensive survey of the performance of one of the most successful non-relativistic self-consistent method, the Skyrme-Hartree-Fock model (SHF), with respect to these constraints. A full description of the Skyrme functional is given and its relation to other effective interactions is discussed. The validity of the application of SHF far from stability and in dense environments beyond the nuclear saturation density is critically assessed. The use of SHF in models extended beyond the mean field approximation by including some correlations is discussed. Finally, future prospects for further development of SHF towards a more consistent application of the existing and promisingly newly developing constraints are outlined.

1 Introduction

1.1 General overview of nuclear structure models

There is a great variety of nuclear structure models at very different theoretical levels. At the most fundamental level are *ab initio* theories which start from a nucleon-nucleon force as input [1] and compute the equation of state for nuclear matter by diagrammatic techniques (for reviews see, e.g., [2, 3]) or from low-energy quantum-chromodynamics (see e.g. [4, 5, 6, 7]). These microscopic approaches have made considerable progress over the past decades. One is even performing *ab initio* calculations for finite nuclei, e.g. in the no-core shell model [8, 9, 10], coupled cluster calculations [11], or in the unitary correlator method [12]. Nonetheless, the actual precision in describing nuclear properties is still

limited, typically 5% precision when *ab initio* two-body forces are used[11] (better quality of about 1% can be achieved when invoking effective three-body forces). Moreover, the application to finite nuclei are computationally very demanding, e.g. the largest no core shell model calculations go at most up to $A=20$ [13]. Thus fully microscopic methods are presently not used for large-scale nuclear structure calculations.

At the most phenomenological level are the macroscopic approaches which are inspired by the idea that the nucleus is a drop of nuclear liquid, giving rise to the liquid-drop model (LDM) or the more refined droplet model, for a recent review see e.g. [14]. With a mix of intuition and systematic expansion in orders of surface effects (the leptodermous expansion) one can write down the corresponding energy functional [15]. There remain a good handful of free parameters, i.e the coefficients for volume energy, symmetry energy, incompressibility, or surface energy. These have to be adjusted to a multitude of nuclear bulk properties with the results that modern droplet parameterizations deliver an excellent description of average trends [16]. Actual nuclei, however, deviate from the average due to quantum shell effects, so that shell corrections have to be added. They are related to the level density near the Fermi surface and can be computed from a well tuned, empirical nuclear single-particle potential. Macroscopic energy plus shell corrections constitute the macroscopic-microscopic (mac-mic) approach which is enormously successful in reproducing the systematics of known nuclear binding energies [17]. One has to admit, though, that the mac-mic method relies strongly on phenomenological input. This induces uncertainties when extrapolating to exotic nuclei. Particularly uncertain is the extrapolation of the single-particle potential used in this model (Nilsson, Yukawa) because this is not determined self-consistently but added as an independent piece of information.

An intermediate level of nuclear models consists in microscopic theories employing effective interactions or effective energy-density functionals. There exist two basically different approaches. On the one hand, one has large scale shell model calculations which aim at a fully correlated description of ground state and excitations up to about 10 MeV, for a review see e.g. [18]. These employ the wave functions of a single-particle basis from empirical shell model potentials complemented by experimental single-particle energies. The effective interaction in the valence space (two-body matrix elements) is taken often from microscopic information, namely the G -matrix from *ab initio* calculations, with a bit of final fine-tuning. Some calculations rely fully on a phenomenological adjustment of the matrix elements. On the other hand, there are the self-consistent mean-field models which aim at a prejudice-free, self-consistent determination of the nuclear ground state and low-energy collective dynamics. The present review concentrates on this latter class of models.

Self-consistent mean-field models, as compared to the mac-mic method, take one big step towards a microscopic description of nuclei. They produce the appropriate single-particle potential corresponding to the actual density distribution for a given nucleus. Still, they cannot be regarded as an *ab initio* treatment because the genuine nuclear interaction induces huge short-range correlations that are not naturally included in a Hartree-Fock model. Self-consistent mean-field models deal with effective energy functionals [19, 20]. The concept has much in common with the successful density-functional theory for electronic systems [21]. The difference is, however, that electronic correlations are well under control and that reliable electronic energy-density functionals can be derived *ab initio* because the electron-electron interaction is well known. The nuclear case is much more involved because the nucleon as such is a composite particle and a nucleon-nucleon interaction is already an approximate concept. Thus, nuclear many-body theories, as discussed above, have not yet reached sufficient descriptive power to serve as direct input for effective mean-field models. They serve as guidance to develop the basic features of the energy-density functionals [19]. The open model parameters are adjusted phenomenologically. The three most prominent schemes are the Skyrme energy functional, traditionally called Skyrme-Hartree-Fock (SHF), the Gogny model, and the relativistic mean field model (RMF), for a recent review see [22]. The present review refers mainly to SHF whilst establishing occasionally relations to the two other schemes (see also Section 2.4).

As said above, the self-consistent mean-field models lie between *ab initio* theories and the mac-mic method. The link between *ab initio* and SHF is still under development, as will be discussed briefly in Section 2.4. The connection between SHF and the mac-mic method is much better developed. There are attempts from both sides. The extended Thomas-Fermi Skyrme interaction scheme (ETFSI) starts from SHF and derives an effective mac-mic model by virtue of a semi-classical expansion [23, 24]. This has been exploited up to a quantitative level [25]. From the macroscopic side there is an attempt to include more self-consistency by virtue of a Thomas-Fermi approach [26, 27]. The investigation of these links turns out to be useful to gain more insight into the crucial constituents of either model.

One of the concerns in applying mean-field models is uncertainty in the phenomenological determination of the free parameters in the effective energy functionals [28]. Many tens of different parameter sets have evolved in the course of the development. The main problem is that one does not have available a one-to-one correspondence between individual parameters and a specific piece of experimental information. It follows that there is a continuum of parameter sets which would fit the experiment with a comparable degree of accuracy. One of the important tasks in the development of mean field models is to devise ways of constraining the free parameters of interaction used. For example, new data from exotic nuclei are an enormous help in that respect. One more recently identified benchmark is the application of SHF to asymmetric nuclear matter [28]. This development is related to an increasing demand for microscopic nuclear structure input into models of stellar matter, occurring in neutron stars and core-collapse supernovae. Realistic description of asymmetric nuclear matter under conditions of extreme density, pressure and temperature poses a new constraint to nuclear theory. It offers an extensive laboratory for testing the applicability of effective mean field models, fitted to properties of finite nuclei close to the beta-stability line, to the limits of nuclear binding at the neutron and proton drip-line. The role of the SHF in providing such input to nuclear astrophysics models and its implication is discussed in this work.

The present review aims to survey the current status of SHF theory as applied in both nuclear and astrophysics areas. The basic concepts and formalism of the Skyrme approach, the choice of parameters and links to the other models of nuclear interactions are detailed in Section 2. Section 3 is devoted to applications in finite nuclei divided into subsections covering static properties (3.1) (binding energies, spin-orbit effects, neutron radii, super-heavy elements and fission barriers), dynamic properties (3.2) (giant resonances, Gamow-Teller resonances, heavy ion collisions and rotational bands) and nucleosynthesis (3.3) (r-process and rp-process). There is a final subsection devoted to discussion of collective correlations beyond the mean field (3.4) (large amplitude collective motion, soft modes and low energy quadrupole states). Section 4 focuses on nuclear matter and astrophysical applications with subsections discussing the relevance of SHF to construction of EOS for compact objects (4.2), the key properties of nuclear matter, models of cold neutron stars (4.3) and hot matter in type II (core-collapse) supernova models. Constraints on parameters of SHF functionals are summarized in Section 5 and conclusions are drawn in Section 6.

2 The Skyrme energy functional

2.1 *A priori* correlations

2.1.1 On the description of correlations

The ultimate goal of a theory is, of course, an *ab initio* description which starts from the basic microscopic understanding of the constituents of the system and predicts finally the properties of a complex compound. The microscopic theory of nucleons and nuclei is quantum chromodynamics (QCD) using quarks and gluons as constituents [29]. However, QCD is a very involved theory and it is already formidable work to compute the properties of single nucleons or mesons. The description of a whole

nucleus is presently far out of reach. Approximate QCD at the level of a low-energy limit or chiral perturbation theory allows approach finite nuclei and nuclear matter and it has been applied with increasing success in recent years [4, 5, 6, 7]. It should be noted, however, that these *ab initio* theories still allow for a few free parameters to achieve fine-tuning of the results. But the field is still in a developing stage and steady improvement may be expected.

Traditional nuclear *ab initio* theories start from nucleons and two-body interactions between them as the basic building blocks. The interaction is determined from an exhaustive analysis of nucleon-nucleon scattering, see e.g. [1]. The aim is a microscopic description of the fully correlated nuclear state. It is called correlated as opposed to the mean-field state (Slater determinant or BCS state) which is the prototype uncorrelated state. One distinguishes several types of correlations. Short-range correlations are related to the hard repulsive core of the nuclear interaction which develops at short inter-nucleon distances below 0.5 fm. Long-range correlations are mediated by the pronounced nuclear resonance modes, the giant resonances; they mediate correlations over distances because their propagator has large coherence length (longer than any existing nucleus). Finally, there are the collective correlations induced by the soft modes with large amplitude such as center-of-mass motion, rotation, or low-lying quadrupole vibrations. Each one of these types of correlation requires its own approach. We will summarize them briefly here. For an extensive review of these very different methods see [30].

The family of conceptually simpler approaches is based on an obvious ansatz for the correlated many-body wavefunction. Examples are the Jastrow ansatz [31], the $\exp(S)$ method [32], and the unitary correlator technique [12]. These three methods have, in principle, much in common but differ in the details of the practical evaluation. They start from a closed expression for the wavefunction and evaluate the expectation values approximately by elaborate expansion techniques (often called coupled cluster expansion). They are designed to describe the short-range correlations associated with the series of two-particle-two-hole (*2ph*) excitations. A more general ansatz is used in the ‘no core shell model’ (NCSM) calculations which have been developed recently, see e.g. [8]. Here one aims at an expansion of the exact many-body wavefunction in a basis of given shell model wavefunctions. This method should in principle embrace all correlations, short as well as long range and to some extent also collective ones.

Alternatively to the NCSM, one has the diagrammatic techniques which are derived most often from the hierarchy of many-body Greens functions [33]. The short-range correlations are related to the series of ladder diagrams. The most widely used method is here the Brueckner-Hartree-Fock (BHF) theory, for a recent review see [2] and for its relativistic cousin, Dirac-Brueckner-Hartree-Fock (DBHF) models [34]. The long-range correlations stem from the series of bubble diagrams (polarization propagators). They play the dominant role in electronic systems [21]. There exist also noteworthy polarization correlations in a nuclear environment, e.g., from the various giant resonance modes [35, 36]. A combined treatment of short- and long-range correlations has been tried in the theory of parquet diagrams [37]. The enormous complexity of these methods has so far hindered widespread applications of this approach. In practice, diagrammatic *ab initio* calculations in nuclear physics deal only with the short-range correlations. That is to some extent legitimate because they yield by far the dominant contributions due to the huge short-range repulsion in the nucleon-nucleon interaction.

Collective correlations require very different methods. The effect of zero-energy modes (center-of-mass, rotation, particle-number) is handled by projection [38]. Low energy modes, as e.g. quadrupole fluctuations, are usually treated by the generator-coordinate method (GCM) [39] and approximations therein [40]. Other methods to deal with large amplitude motion in a wavefunction picture are re-quantized time-dependent Hartree-Fock (TDHF) or path integrals [41, 42, 43]. Alternatively, one can describe a system in terms of operator algebra and large amplitude motion is covered here by boson expansion techniques [44].

The above short summary indicates that collective correlations differ strongly from short- and long-range correlations and appear at a different level of description. The collective correlations are related to shape and surface of finite nuclei and are very sensitive to shell effects which makes them vary

strongly from nucleus to nucleus. On the other hand, short- and long-range correlations are fully active in the nuclear volume and persist up to nuclear matter. Their effect is smoothly varying with proton and neutron number. The latter feature justifies summarizing these correlations implicitly in an effective energy-density functional, or effective interaction respectively. The way this is done and its consequences is sketched in the following subsections. The main message to be kept in mind is that these short- and long-range correlations have been *a priori* built into the mean-field model and they should not be computed again with these effective interactions (although there exist techniques to recover carefully some of those correlations in the T -matrix approach [45]). The collective correlations, on the other hand, cannot be transferred to a simple effective functional because they do not obey smooth trends and rather vary strongly with proton and neutron number. They need to be left for *a posteriori* treatment. The danger of double counting correlations is small because strongly fluctuating effects cannot be included already in a smooth energy functional. Examples for collective correlations will be discussed in Section 3.4.

Finally, we want to address again the limitations of *ab initio* in a nuclear context. The starting assumption of nucleons as basic constituents is only approximately correct. It is then no surprise that all strict *ab initio* calculations starting from measured nucleon-nucleon interactions fail to reproduce nuclear binding and radii at a quantitative level (with typical errors of about 5% [46]). This fact has inhibited so far a parameter-free deduction of effective energy-functionals. The quality of *ab initio* calculations can be significantly enhanced by introducing effective three-body forces. These, however, introduce free parameters in the treatment which spoil the ideal of an *ab initio* derivation. As a consequence, the free parameters of nuclear energy-density functional are directly fitted to empirical data, see Section 2.3.

2.1.2 Motivation of the Skyrme functional

The formally most transparent way to explain the construction of an effective interaction is provided by the unitary correlator method. The fully correlated state is written as a unitary transformation \hat{U} of a mean field state $|\Phi\rangle$, i.e.

$$|\Psi\rangle = \hat{U}|\Phi\rangle \quad . \quad (1)$$

At the lowest level, the unitary transformation is composed from exponentiated two-body correlations

$$\hat{U} = \exp\left(i \sum c_{abcd} \hat{a}_a^+ \hat{a}_b^+ \hat{a}_c \hat{a}_d\right) \quad (2)$$

where \hat{a}^+ , \hat{a} are Fermion operators [12]. The energy expectation value is regrouped as

$$E = \langle \Psi | \hat{H} | \Psi \rangle = \langle \Phi | \hat{U}^+ \hat{H} \hat{U} | \Phi \rangle = \langle \Phi | \hat{H}_{\text{eff}} | \Phi \rangle \quad . \quad (3)$$

This defines the effective Hamiltonian

$$\hat{H}_{\text{eff}} = \hat{U}^+ \hat{H} \hat{U} \quad (4)$$

by associating the correlators to the Hamiltonian. Note that the expectation value with \hat{H}_{eff} is well defined only in connection with mean-field states $|\Phi\rangle$ and for nothing else. The price for the ‘effectiveness’ is the restriction of the legitimate Hilbert space. Such restrictions are best handled in variational formulations and it is thus natural that effective mean-field models come along in this fashion. Thus far the principle of building an effective interaction looks simple and is well established in the derivation of effective charges (for a discussion in diagrammatic terms see [47]). The practical evaluation, however, is extremely tedious and not very enlightening.

More details about the desirable structure of a Skyrme-like effective functional are disclosed by the technique of the density-matrix expansion [48]. Many *ab initio* models deliver at the end an effective

two-body interaction as an involved integral operator \hat{G} . This holds, in particular, for the Brückner-Hartree-Fock method (BHF) whose G -matrix serves finally as effective force for the Hartree-Fock part, for a recent review see e.g [2]. An effective force as integral operator can also be extracted from many other *ab initio* models, as e.g. the above mentioned unitary correlator method. In any case, the most general total energy becomes

$$E_{\text{pot}} = \int dx dx' dy dy' \rho(x, x') G(x, x'; y, y') \rho(y, y') \quad (5)$$

where $\rho(x, x')$ is the one-body density matrix which falls off quickly with increasing $|x - x'|$ with a typical range of k_F^{-1} where k_F is the Fermi momentum. More importantly, the integral kernel G is also non-zero only for small differences in all pairs of coordinates with typical ranges mostly below k_F^{-1} . This suggests an expansion in orders $(x - x')^n$ around $\bar{x} = (x + x')/2$ in the form

$$\rho(x, x') \approx n(\bar{x}) + i(x - x') \cdot j(\bar{x}) + \frac{1}{2}(x - x')^2 \left(\tau - \frac{1}{4} \Delta n \right) \quad , \quad (6)$$

where n is the local density, j the local current, and τ the kinetic-energy density, see Section 2.2.1. It is obvious that this expansion in $x - x'$ and similarly in $y - y'$ yields properly the τ terms in the functionals. The G matrix is also well localized in the differences $x - y$ and $x' - y'$. An expansion of the G matrix with respect to these differences yields the gradient terms $\propto \Delta n$ in the effective functional. Altogether, the density-matrix expansion demonstrates how a zero-range effective interaction emerges from the initially given involved operator structure. We are dealing with a typical low-energy or low- q expansion. It becomes apparent that this puts even more constraints on the legitimate mean-field states. The spatial structure should be sufficiently smooth. A safe estimate takes the pion wavelength as the largest range in G . This complies with the spatial variations in the wavefunctions and densities of order of k_F^{-1} at normal nuclear density. The validity of effective functionals exceeds often the range of such safe estimates. But one should be warned about extension to high densities. Sooner or later, effective functionals of zero range will become inappropriate. There exist methods to extend the range to a broader span of densities which have been worked out, e.g., for ${}^3\text{He}$ systems [49] but not yet for nuclear systems.

Density functional theory provides the conceptually and technically simplest way to derive an energy-density functional from *ab initio* calculations. This is the much celebrated local-density approximation (LDA) [21]. We sketch it briefly for the case of one component. A nuclear LDA deals, of course, with two components, for protons and for neutrons separately. The basic steps can be summarized as follows:

$$n \implies \frac{E}{N} = \epsilon(n) \implies E = \int d^3r n \epsilon(n) \xrightarrow{n \rightarrow n(r)} E^{(\text{LDA})} = \int d^3r n(r) \epsilon(n(r)) \quad . \quad (7)$$

One performs first a series of *ab initio* calculations in bulk matter for many different (homogenous) densities n . This yields an energy per particle E/N as function of n . It is rewritten as a spatial integral which is still exact for homogenous densities. The crucial step comes when allowing for spatially varying densities $n \rightarrow n(r)$. This assumes that the finite and inhomogeneous system can be treated as a succession of pieces of bulk. This is an approximation for sufficiently smooth density distributions. What “sufficiently smooth” means in practice remains an open question as has been discussed already at the end of the previous paragraph. We will reconsider that question with a realistic application in Section 2.4.3.

2.2 The composition of the energy functional

2.2.1 The wavefunctions and densities

The key idea in a mean field theory is that one seeks to describe the many-body system exclusively in terms of a set of single-particle wavefunctions $\{\varphi_\alpha, \alpha = 1, \dots, A\}$. These constitute the many-body state

as a Slater determinant which is the anti-symmetrized product of all occupied single-particle states. A pure Slater state is simply applicable only to doubly-magic nuclei which, however, are a small minority in the table of isotopes. All others have partially open shells with a high density of almost degenerated states which gives the residual two-body interaction a chance to mix these states in order to produce a unique ground state [50]. This can be handled very efficiently and to a reasonable approximation by a nuclear pairing scheme, see e.g. [38, 22] for details. At the end, this amounts associating an occupation amplitude v_α with each single-nucleon state φ_α . This amplitude can take values continuously in the interval $[0, 1]$. The complementary non-occupation amplitude is $u_\alpha = \sqrt{1 - v_\alpha^2}$. Thus the typical mean-field state is a BCS state

$$|\Phi\rangle = \Pi_\alpha (u_\alpha + v_\alpha \hat{a}_\alpha^+ a_\alpha) |0\rangle \quad (8)$$

where $|0\rangle$ is the vacuum state. This BCS state comprises all the information carried in the set $\{\varphi_\alpha, v_\alpha; \alpha=1, \dots, \Omega\}$. The limit $\Omega > A$ denotes the size of the pairing-active space. The dynamical degrees-of-freedom are the single-particle wavefunctions φ_α and the occupation amplitudes v_α . The mean field equations are obtained by variation of the total energy with respect to these both quantities. The expression for the total energy is the key ingredient in the modeling. We will employ here the Skyrme energy-density functional as given in Section 2.2.2 together with a pairing functional, see Section 2.2.4. The equations for the Hartree-Fock mean field are obtained by variation with respect to the wavefunctions φ_α while the gap equations for the pairing mean field come from variation of the v_α .

Wavefunctions and occupations amplitudes uniquely define all one-body densities. Energy-density functionals should require the knowledge of only a few local densities and and currents, such as the local density $n(\mathbf{r})$. For nuclei, we have to distinguish proton and neutron density, n_p and n_n . Note that we are using here the symbol n for the local particle number density. This differs from the standard usage in the SHF community of the symbol ρ for this quantity. But it complies with the usage in nuclear astrophysics where the symbol ρ is reserved for the mass density (see Section 4.2), and it agrees also with the standards of electronic density-functional theory [21]. Furthermore, nuclear energy functionals invoke also the kinetic-energy density τ , the spin-orbit density \mathbf{J} , the current \mathbf{j} , the spin density $\boldsymbol{\sigma}$, and the kinetic spin density $\boldsymbol{\tau}$. These read in detail

$$n_q(\mathbf{r}) = \sum_{\alpha \in q} |v_\alpha^2| |\varphi_\alpha(\mathbf{r})|^2 \quad q \in \{p, n\} \quad , \quad (9a)$$

$$\tau_q(\mathbf{r}) = \sum_{\alpha \in q} |v_\alpha^2| |\nabla \varphi(\mathbf{r})|^2, \quad (9b)$$

$$\mathbf{J}_q(\mathbf{r}) = -i \sum_{\alpha \in q} |v_\alpha^2| \varphi_\alpha^+(\mathbf{r}) \nabla \times \hat{\sigma} \varphi_\alpha(\mathbf{r}) \quad , \quad (9c)$$

$$\mathbf{j}_q(\mathbf{r}) = -\frac{i}{2} \sum_{\alpha \in q} |v_\alpha^2| (\varphi_\alpha^+(\mathbf{r}) \nabla \varphi_\alpha(\mathbf{r}) - \nabla \varphi_\alpha^+(\mathbf{r}) \varphi_\alpha(\mathbf{r})) \quad , \quad (9d)$$

$$\boldsymbol{\sigma}(\mathbf{r}) = \sum_{\alpha \in q} |v_\alpha^2| \varphi_\alpha^+(\mathbf{r}) \hat{\sigma} \varphi_\alpha(\mathbf{r}) \quad , \quad (9e)$$

$$\boldsymbol{\tau}(\mathbf{r}) = \sum_{\alpha \in q} |v_\alpha^2| \sum_{i \in \{xyz\}} \nabla_i \varphi_\alpha^+(\mathbf{r}) \hat{\sigma} \nabla_i \varphi_\alpha(\mathbf{r}) \quad . \quad (9f)$$

It is often useful to recouple to sum and difference, e.g.

$$n = n_p + n_n \quad , \quad \tilde{n} = n_p - n_n \quad , \quad (9g)$$

and similarly for all other densities and currents. The sum plays a role in the isoscalar terms of the energy functional and we will call it the isoscalar density n . In a similar manner, the difference plays the role of an isovector density \tilde{n} .

2.2.2 Basic formalism

The Skyrme force was first introduced by Skyrme in [51, 52] as an effective force for nuclear Hartree-Fock calculations. Its widespread application started with the revival by Vautherin and Brink in [53, 54]. It used to be formulated as an effective interaction

$$\begin{aligned}
\hat{V}_{\text{eff}}(\mathbf{r}_1, \mathbf{r}_2) &= t_0(1+x_0\hat{P}_\sigma)\delta(\mathbf{r}_1-\mathbf{r}_2) + \frac{t_3}{6}(1+x_3\hat{P}_\sigma)\delta\left(\frac{1}{2}(\mathbf{r}_1+\mathbf{r}_2)\right)\delta(\mathbf{r}_1-\mathbf{r}_2) \\
&\quad - \frac{t_1}{2}(1+x_1\hat{P}_\sigma)((\nabla_1-\nabla_2)^2\delta(\mathbf{r}_1-\mathbf{r}_2) + h.c.) \\
&\quad - t_3(1+x_2\hat{P}_\sigma)((\nabla_1-\nabla_2)\delta(\mathbf{r}_1-\mathbf{r}_2)(\nabla_1-\nabla_2)) \\
&\quad - it_4(\nabla_1-\nabla_2)\times\delta(\mathbf{r}_1-\mathbf{r}_2)(\nabla_1-\nabla_2)\cdot(\hat{\boldsymbol{\sigma}}_1+\hat{\boldsymbol{\sigma}}_2) \quad , \quad (10) \\
\hat{P}_\sigma &= \frac{1}{2}(1+\hat{\boldsymbol{\sigma}}_1\cdot\hat{\boldsymbol{\sigma}}_2) \quad ,
\end{aligned}$$

where \hat{P}_σ is the spin-exchange operator. It is a zero-range interaction with kinetic and density-dependent terms. The zero range is an idealization which is consistent with the smoothly varying dependence of the mean field state on spatial coordinates. Such a force makes sense only in connection with such smooth wavefunctions and should never be used to regenerate short-range correlations [53]. The density dependent term $\propto t_3$ is of particular importance as it provides appropriate saturation and thus secures the success of SHF in description of finite nuclei. It is motivated by the concept of effective forces between nucleons in nuclear environment in contrast to the forces between bare nucleons. It can be seen as arising from either the concepts of effective forces or energy functionals, resulting from the variation with density of the underlying microscopic effective interaction or of the energy (see [48] and Section 2.1.2). It was originally formulated as a zero-range three-body force which is equivalent to the density-dependent interaction (DDI) when used in calculations of ground state properties. However, the two interpretations of the $\propto t_3$ differ when excitations are considered and the DDI approach is found to be more stable [55]. On the other hand, the concept of a DDI leads to inconsistencies in a variational formulation in that the variationally derived two-body interaction is not identical to the initially given interaction from which the energy was computed as expectation value. What is done in practice, is to compute the total energy as expectation value of the interaction first (10) and then derive the Hartree-Fock equations and solve them using the standard variational procedure. This is precisely the concept of an effective energy-density functional. And this is the line of development which we will pursue in the following.

Our starting point is then the most general Skyrme energy functional which reads

$$E = \int d^3r n \{ \mathcal{E}_{\text{kin}} + \mathcal{E}_{\text{Skyrme}} + \mathcal{E}_{\text{Skyrme,odd}} \} + E_{\text{Coulomb}} + E_{\text{pair}} + E_{\text{cm}} \quad , \quad (11a)$$

$$n\mathcal{E}_{\text{kin}} = \frac{\hbar^2}{2m} \int d^3\tau \quad , \quad (11b)$$

$$\begin{aligned}
n\mathcal{E}_{\text{Skyrme}} &= \frac{B_0 + B_3 n^\alpha}{2} n^2 - \frac{B'_0 + B'_3 n^\alpha}{2} \tilde{n}^2 \\
&\quad + B_1(n\tau - \mathbf{j}^2) - B'_1(\tilde{n}\tilde{\tau} - \tilde{\mathbf{j}}^2) - \frac{B_2}{2}n\Delta n + \frac{B'_2}{2}\tilde{n}\Delta\tilde{n} \\
&\quad - B_4 n \nabla \cdot \mathbf{J} - (B_4 + B'_4)\tilde{n} \nabla \cdot \tilde{\mathbf{J}} + \frac{C_1}{2}\mathbf{J}^2 - \frac{C'_1}{2}\tilde{\mathbf{J}}^2 \quad , \quad (11c)
\end{aligned}$$

$$\begin{aligned}
n\mathcal{E}_{\text{Skyrme,odd}} &= -\frac{C_0 + C_3 n^\alpha}{2}\boldsymbol{\sigma}^2 + \frac{C'_0 + C'_3 n^\alpha}{2}\tilde{\boldsymbol{\sigma}}^2 + \frac{C_2}{2}\boldsymbol{\sigma} \cdot \Delta \boldsymbol{\sigma} - \frac{C'_2}{2}\tilde{\boldsymbol{\sigma}} \cdot \Delta \tilde{\boldsymbol{\sigma}} \\
&\quad - C_1 \boldsymbol{\sigma} \cdot \boldsymbol{\tau} + C'_1 \tilde{\boldsymbol{\sigma}} \cdot \tilde{\boldsymbol{\tau}} - B_4 \boldsymbol{\sigma} \cdot (\nabla \times \mathbf{j}) - (B_4 + B'_4)\tilde{\boldsymbol{\sigma}} \cdot (\nabla \times \tilde{\mathbf{j}}) \quad , \quad (11d)
\end{aligned}$$

$$E_{\text{Coulomb}} = e^2 \frac{1}{2} \int d^3r d^3r' \frac{n_{\text{p}}(\mathbf{r})n_{\text{p}}(\mathbf{r}')}{|\mathbf{r}-\mathbf{r}'|} - \frac{3}{4}e^2 \left(\frac{3}{\pi}\right)^{1/3} \int d^3r [n_{\text{p}}]^{4/3} \quad . \quad (11e)$$

The B (B') parameters determine the strength of the isoscalar (isovector) forces. The spin-orbit term $\propto B_4, B'_4$ has only one free parameter B_4 in the standard Skyrme functionals where one fixes $B'_4 = 0$. The need for full isovector freedom in the spin-orbit term, i.e. for a non-zero B'_4 , was raised by the systematics of isotopic shifts in Pb isotopes [56]. The principle Skyrme functional $\mathcal{E}_{\text{Skyrme}}$ contains just the minimum of time-odd currents and densities which is required for Galileian invariance [57], namely the combinations $n\tau - \mathbf{j}^2$ and $n\nabla \cdot \mathbf{J} + \boldsymbol{\sigma} \cdot (\nabla \times \mathbf{j})$. Further conceivable time-odd couplings are collected in the optional terms in $\mathcal{E}_{\text{Skyrme,odd}}$. In case of a derivation from the zero-range two-body force (10), they are related to the B parameters of $\mathcal{E}_{\text{Skyrme}}$ and the relation is given implicitly in eq. (12). All these C -terms are optional from the perspective of a pure energy-density functional and they are not yet well determined. The pure spin terms $\propto C_0, C_2$ play a role only in truly time-odd situations such as, odd- A nuclei or the Gamow-Teller excitations (see Section 3.2.2); they are not yet well investigated. The tensor spin-orbit terms $\propto C_1, C'_1$ can contribute in most standard situations although no specific consequence of their inclusion or need for them has not yet been unambiguously identified. The Coulomb functional (11e) depends only on the charge density and stays outside this distinction. Its second term approximates exchange in the Slater approximation [58]. Note that we use the proton density in place of the charge density. This is a widely used, more or less standard, approximation. The center of mass (c.m.) term E_{cm} will be discussed in Section 2.2.3 and the pairing energy E_{pair} in 2.2.4.

The energy-functional (11) leaves the time-odd part (11d) open for free adjustment. The viewpoint of an effective interaction as formulated in eq. (10) establishes unique relations between the frequently used interaction parameters t_i, x_i and the functional parameters B_i, C_i :

$$\begin{aligned}
B_0 &= \frac{3}{4}t_0 \quad , & B'_0 &= \frac{1}{2}t_0(0.5 + x_0) \quad , \\
B_1 &= \frac{3}{16}t_1 + \frac{5}{16}t_2 + \frac{1}{4}t_2x_2 \quad , & B'_1 &= \frac{1}{8} \left[t_1(0.5 + x_1) - t_2(0.5 + x_2) \right] \quad , \\
B_2 &= \frac{9}{32}t_1 - \frac{5}{32}t_2 - \frac{1}{8}t_2x_2 \quad , & B'_2 &= \frac{1}{16} \left[3t_1(0.5 + x_1) + t_2(0.5 + x_2) \right] \quad , \\
B_3 &= \frac{3}{16}t_3 \quad , & B'_3 &= \frac{1}{8}t_3(0.5 + x_3) \\
B_4 &= b_4 - 0.5b'_4 \quad , & B'_4 &= 0.5b'_4 \quad ,
\end{aligned} \tag{12a}$$

$$\begin{aligned}
C_0 &= -0.5t_0(0.5 - x_0) \quad , & C'_0 &= \frac{1}{4}t_0 \quad , \\
C_1 &= \frac{1}{8} \left[t_1(0.5 - x_1) - t_2(0.5 + x_2) \right] \quad , & C'_1 &= -\frac{1}{16}(t_1 - t_2) \quad , \\
C_2 &= -\frac{1}{16} \left[3t_1(0.5 - x_1) + t_2(0.5 + x_2) \right] \quad , & C'_2 &= \frac{1}{32}(3t_1 + t_2) \quad , \\
C_3 &= -\frac{1}{8}t_3(0.5 - x_3) \quad , & C'_3 &= \frac{1}{16}t_3 \quad ,
\end{aligned} \tag{12b}$$

There is a one-to-one correspondence between the B and the t, x -parameterizations. The C -parameters are a consequence of the interaction ansatz and can in this connection be considered as function of the B s. At first glance, this feature looks like an advantage of the interaction model. However, this imposed restrictions may lead to conflicting requirements as worked out in Section 3.1.2 in connection with the isovector spin-orbit force. The zero-range two-body spin-orbit interaction in the ansatz (10) forces $B'_4 = 0$ while the energy functional takes B'_4 as a free parameter which is found desirable to be adjusted independently.

Empirical information for the other terms in the time-odd part (11d) is much harder to obtain. These terms are not active in the ground state of even-even nuclei. Odd nuclei could supply useful information, however mixed with pairing properties [59]. This has not yet been explored in a systematic manner. Excitations probe time-odd terms and the spin-couplings are particularly crucial in modes with unnatural parity, see Section 3.2.2. Again, this is an area where systematic explorations are still ahead. Theoretical assistance can be obtained from the RMF where spin properties are fixed by the Dirac

equation. A study of the non-relativistic limit suggests a minimalistic model $C_i = 0$ [60] which delivers the correct isovector structure for the spin-orbit coupling [56].

2.2.3 The center of mass correction

Electron clouds in an atomic or molecular system are bound by the external Coulomb forces of the ionic background. Nuclei are different in that their center of mass moves freely through space without confining fields (at least at nuclear scale). Thus the nuclear ground state should be projected on center-of-mass (c.m.) momentum zero [38]. The exact projection is tedious and a hindrance to large scale calculations. Fortunately, the c.m. projection is well behaved and can be approximated by simple expressions [61]. Two different approximate expressions for the c.m. correction are in use:

$$E_{\text{cm}} = E_{\text{cm}}^{(\text{full})} = -\frac{1}{2mA} \langle (\sum_i \hat{p}_i)^2 \rangle, \quad (13a)$$

$$E_{\text{cm}} = E_{\text{cm}}^{(\text{diag})} = -\frac{1}{2mA} \langle \sum_i \hat{p}_i^2 \rangle, \quad (13b)$$

where the brackets mean the expectation value over the BCS state (8). The full correction (13a) is a second order approximation to the exact c.m. projection and works very well for nuclei with $A \geq 40$ and is still a fair approximation for lighter nuclei [61]. It encompasses effectively a two-body operator which adds complications to the variational mean field equations. Thus it is usually added *a posteriori*, i.e. after the solution of the mean field equations (projection after variation). The correction (13b) takes only the diagonal parts of the two-body operator and so yields a one-body operator. This allows it to be included in the mean field equations (variation after projection) which is the standard for that variant of the theory. However, the form (13b) is a rather poor approximation to the full correction (13a) and should be avoided. An attempt to cure the defects of this approach by a simple fit formula was made in [62] where the term (13b) is augmented by a factor $f(A) = 2/(t + 1/3t)$ with $t = (\frac{3}{2}A)^{1/3}$. There is also a center-of-mass correction for the nuclear density distribution and quantities deduced therefrom. This will be discussed in Section 2.2.6.

2.2.4 Pairing interaction

Pure Slater states are distinguished by occupation weights $n_\alpha \in \{0, 1\}$. Such states are appropriate, however, only for doubly magic nuclei. All others have partially open shells with a high density of almost degenerated states which gives the residual two-body interaction a chance to mix these states in order to produce a unique ground state [50]. This can be handled very efficiently and to a reasonable approximation by a nuclear pairing scheme, see e.g. [38, 22] for details. In the end, this amounts to associating an occupation amplitude $v_\alpha \in [0, 1]$ with each single-nucleon state φ_α . The complementing non-occupation amplitude is $u_\alpha = \sqrt{1 - v_\alpha^2}$. Assuming a zero-range residual interaction leads to the pairing energy functional

$$E_{\text{pair}} = E_{\text{pair}}^{(\text{DI})} = \frac{1}{4} \sum_{q \in \{p, n\}} V_q^{(\text{pair})} \int d^3r \chi_q^2, \quad \chi_q(\mathbf{r}) = \sum_{\alpha \in q} w_\alpha u_\alpha v_\alpha |\varphi_\alpha(\mathbf{r})|^2, \quad (14a)$$

where DI stands for δ -interaction and w_α is some phase-space weight. This pairing acts without prejudice throughout the whole nuclear volume. There are good reasons to assume that most of the pairing takes place near the nuclear surface [63]. That is accounted for by the density-dependent δ -interaction (DDDI) with the functional [64]

$$E_{\text{pair}} = E_{\text{pair}}^{(\text{DDDI})} = \frac{1}{4} \sum_q v_{0,q} \int d^3r \chi_q^2 \left[1 - \left(\frac{n}{n_0} \right)^\gamma \right], \quad (14b)$$

where n_0 is the nuclear saturation density, typically $n_0 = 0.16 \text{ fm}^{-3}$ and γ models the surface profile of the interaction. A standard value is $\gamma = 1$. For a discussion of the effects of varying γ see, e.g., [65]. The two forms of the pairing functional (14a,14b) are practically standard in modern SHF calculations. The strength parameters $V_p^{(\text{pair})}$ and $V_n^{(\text{pair})}$ are universal in that they can be adjusted to hold for the whole nuclear landscape. There are more elaborate treatments using the pairing part of the Gogny force [66] which is, of course, compulsory in Gogny mean-field calculations and which is also often used in RMF approaches, see e.g. [67]. Most older calculations use simpler schemes for pairing such as, a constant pairing matrix element of a constant gap [68, 67]. These recipes depend very sensitively on the pairing phase space and their parameters change substantially over the nuclei. They do not meet the high standards of modern mean field calculations.

The results of HFB or HFBCS calculations (see Section 2.2.5) depend on the space of single-nucleon states taken into account, called here pairing phase space. The convergence with increasing phase space is extremely slow [69] so some cut-off procedure is compulsory to obtain a manageable scheme. In fact, the cut-off is part of the pairing description. It is provided by the phase-space weights w_α in the above pairing functionals. The simplest way is to use a sharp cut with $w_\alpha \in \{0, 1\}$. This works well in connection with large pairing spaces reaching up to 50 MeV above the Fermi surface [70]. Practicability often requires cuts at lower energy. The sharp cutoff then raises ambiguities if the level density near the cutting edge is high. Much more elegant and stable is a soft cutoff profile such as, $w_\alpha = [1 + \exp((\epsilon_\alpha - (\epsilon_F + \epsilon_{\text{cut}}))/\Delta\epsilon)]^{-1}$ where typically $\epsilon_{\text{cut}} = 5 \text{ MeV}$ and $\Delta\epsilon = \epsilon_{\text{cut}}/10$ [71, 72]. This works very well for all stable and moderately exotic nuclei. For better extrapolability away from the valley of stability, the fixed margin ϵ_{cut} may be modified to use a band of fixed particle number $\propto N^{2/3}$ instead of a fixed energy band [73].

A basic problem with pairing is particle-number conservation. The BCS state (8) is adjusted to reproduce the correct *average* number of protons and neutrons. But it comes with some uncertainty in proton and neutron number as soon as $u_\alpha v_\alpha \neq 0$. This uncertainty is embodied in the mean field approximation. Nonetheless, one often sees a need for restoring exact particle numbers. This can be achieved by particle-number projection [38] although this is a bit cumbersome and, even worse, is not necessarily consistent in connection with energy-density functionals [74]. As in the case of c.m. projection, one can resort to approximate projection which is done usually in terms of the Lipkin-Nogami (LN) prescription (for a detailed discussion with comprehensive references see [22]). Most of the results presented here use simple BCS or HFB unless otherwise indicated.

2.2.5 The mean field and pairing equations

The energy functional (11) once fully specified determines everything. The mean field plus pairing equations are obtained in a straightforward manner. Variation with respect to the single-nucleon wavefunctions φ_α^+ yields the mean-field equations and variation with respect to the occupation amplitudes v_α provides the Bogoliubov equations, both together comprising the Hartree-Fock-Bogoliubov scheme (HFB). In practice, the feedback of v_α variation on the mean field is neglected, yielding the Bardeen-Cooper-Schrieffer (BCS) approximation to pairing. We skip the detailed mean field and pairing equations for reasons of brevity. A comprehensive description is found in the recent review [22].

Numerical implementation of the HFB(CS) equations requires further consideration. There are two different ways to represent wavefunctions and fields. On the one hand are the basis expansions which usually employ harmonic oscillator wavefunctions (for a recent detailed application see [75]). On the other hand are grid techniques where the wavefunctions and fields are represented on a grid in coordinate space. Depending on the symmetry, this can be a radial 1D, an axial 2D, or a Cartesian 3D grid. Coordinate-space grids are well suited for self-consistent mean fields which employ local densities. For the kinetic energy, various approximations are available: Fourier representation or finite difference formulae at various orders. The optimum choice depends on the dimensionality, see e.g. [76]. A detailed

example of implementation on a spherical one-dimensional grid is presented in [77].

2.2.6 Computation of basic observables

The most prominent observable is, of course, the total energy. It is the starting point of the description (see Section 2.2.2) and thus naturally results from any mean field calculation. The best possible reproduction of the energies is, of course, the most important feature in the development of the model, see Section 2.3.1. A more refined view emerges when looking at energy differences which may reveal information on the underlying shell structure (see Section 3.1.1) or lead to effects beyond a mere mean-field description (see Section 3.4). A further energy-related quantity is the single particle spectrum. It is a natural outcome of mean field calculations. There is, however, no direct relation to experimental observables. One usually deduces single particle energy from neighboring odd-A nuclei which means that the results are masked by polarization and correlation effects. But differences of single-particle energies, in particular spin-orbit splittings, can be extracted fairly well [78].

Next to the energy, the density distribution is a key feature of nuclear structure. Elastic electron scattering allows a more or less model free experimental determination of the nuclear charge formfactor $F_{\text{ch}}(\mathbf{k})$ [79]. The formfactor is related to the density by a simple Fourier transformation $F_q(\vec{k}) = \int d^3r \exp i\vec{k} \cdot \vec{r} n_q(\vec{r})$ where the variable index $q \in \{\text{ch}, \text{p}, \text{n}\}$ indicates that this one-to-one relation holds for any distribution, charge, proton or neutron like. It depends only on $k = |\vec{k}|$ for spherical systems. We will base the following discussion on the less intuitive but formally simpler formfactor and assume spherical symmetry. Mean field calculations yield proton and neutron formfactors. The charge formfactor is obtained by multiplying these with the intrinsic proton and neutron formfactors (equivalent to folding of the densities) [80]

$$F_{\text{ch}}(k) = \sum_q [F_q G_{E,q} + F_{ls,q} G_M] \exp\left(\frac{\hbar^2 k^2}{8 \langle \hat{P}_{\text{cm}}^2 \rangle}\right) \quad (15)$$

where $F_{ls,q}$ is the form factor of $\nabla \cdot \vec{J}_q$ augmented by a factor $\mu_q/4m^2$ with μ_q being the magnetic moment of the nucleon, $G_{E,q}$ is the electric form factor and G_M the magnetic form factor of the nucleons (assumed to be equal for both species). The overall exponential factor takes into account the center-of-mass correction for the formfactor complementing the corresponding energy correction as discussed in Section 2.2.3. It employs the same variance of the total momentum $\langle \hat{\mathbf{P}}_{\text{cm}}^2 \rangle$ and its physical interpretation is an unfolding of the spurious vibrations of the nuclear center-of-mass in harmonic approximation [61]. The nucleon form factors $G_{E,q}$ and G_M are taken from nucleon scattering data [81, 82], for details see [22].

Energy density functionals should, in principle, provide a reliable description of all density distributions, or, equivalently, formfactors. Actual functionals employ analytically simple forms which are smooth functions of the densities as motivated by a local-density approximation. It has been shown that this limits the predictive value to the regime $k < 2k_F$ in the formfactor where k_F is the Fermi momentum [83]. Fortunately, the salient features of the nuclear shape are determined in that low k range. They can be characterized in terms of three form parameters: r.m.s. radius r_{ch} , diffraction radius R_{ch} , and surface thickness σ_{ch} [79]. They are computed as [79]

$$r_{\text{ch}} = \frac{3}{F_{\text{ch}}(0)} \left. \frac{d^2}{dk^2} F_{\text{ch}}(k) \right|_{k=0}, \quad (16a)$$

$$R_{\text{ch}} = \frac{4.493}{k_0^{(1)}} \quad , \quad F_{\text{ch}}(k_0^{(1)}) = 0 \quad (16b)$$

$$\sigma_{\text{ch}} = \frac{2}{k_m} \log\left(\frac{F_{\text{box}}(k_m)}{F_{\text{ch}}(k_m)}\right) \quad , \quad F_{\text{box}}(k) = 3 \frac{j_1(k_m R_{\text{ch}})}{k_m R_{\text{ch}}} \quad , \quad k_m = 5.6/R_{\text{ch}} \quad (16c)$$

The diffraction radius R_{ch} parameterizes the overall diffraction pattern which resembles those of a filled sphere of radius R_{ch} . It is called the box equivalent radius [79]. The actual nuclear form factor decreases faster than the box form factor F_{box} due to the finite surface thickness σ of nuclei which is thus determined by comparing the height of the first maximum of the box equivalent form factor and of the mean-field result F_{ch} . The simple combination $\sqrt{\frac{3}{5}R_{\text{ch}}^2 + 3\sigma_{\text{ch}}^2} - r_{\text{ch}}$ of these three form parameters serves as a nuclear halo parameter which is found to be a relevant measure of the outer surface diffuseness [84].

The charge distribution is mostly sensitive to the proton distribution. Useful complementing information is contained in the neutron distribution which is discussed briefly in Section 3.1.3.

2.3 Basic features

The form of the energy functional as presented in Section 2 is based on a low momentum expansion of many-body theory [48] which leads naturally to local point couplings with some density dependence. The parameters of the functional are universal in the sense that they apply unmodified to all conceivable nuclei however they have to be determined by fit to experimental data since nuclear many-body theories are not yet precise enough to allow an *ab initio* computation of nuclear properties with the precision which we need for practical applications. Thus it is still state of the art to adjust the parameters of the functional phenomenologically. Typical strategies for the adjustment will be discussed in Section 2.3.1 and its practical consequences subsequently. Thereby we include also the RMF in the considerations as the relativistic cousin of SHF because similarities and differences between SHF and RMF are often quite instructive. The connection to BHF and the importance of each parameter is discussed briefly in 2.4.3.

2.3.1 Fitting strategies

The parameters of the functional are adjusted such that a certain set of observables is optimally reproduced. Different groups have different biases in selecting these observables. Fits are usually restricted to a few semi- or doubly-magic spherical nuclei (an exception is a recent large-scale fit to all known nuclear masses [85]). All fits take care of binding energy E_{B} and r.m.s. charge radii r_{ch} after which different tracks are pursued. SHF fits include extra information on spin-orbit splittings while RMF incorporates the spin-orbit interaction automatically as a relativistic effect, see Section 2.4.1. Pairing properties are usually adjusted to the odd-even staggering of binding energies, see e.g. [86, 73]. Some fits add information on nuclear matter, the series [87] even on neutron matter. Others make a point to include information from the electromagnetic formfactor [88] (see Section 2.2.6). Differences exist also in the bias and weight given to the various observables; e.g., the force BSk1 fits exclusively to binding energies (\equiv atomic masses). Recently, attention has been brought to possible corrections for proton-neutron correlations in $N = Z$ nuclei, often called the Wigner energy [89] (see e.g. the fits of [85]). A detailed discussion of fitting strategies can be found, e.g., in [22].

In view of these different prejudices entering the fits, there exist many different parameterizations for SHF as well as RMF. We confine the discussion to a few well adjusted and typical sets. They are summarized together with their citations, actual options, and fit bias (last two columns) in Table 1. A few further explanations are in order. They expand mainly the key words in the column ‘comments’. SkM* belonged to the second generation of Skyrme forces which delivered for the first time a well equilibrated high-precision description of nuclear ground states. It was developed with an explicit study of surface energy and fission barriers in semiclassical approximation. SkP aimed at a simultaneous description of the mean field and of pairing. The set SLy6 and its cousins (see [87]) have been developed with a bias to neutron rich nuclei and neutron matter aiming at astrophysical applications. SkI3 and SkI4 exploit the freedom of an isovector spin-orbit force to obtain an improved description of isotopic

force	ref.	c.m.	l*s T=1	η_s	Coul.ex.	nuc.mat.	comments
SkM*	[90]	diag	no	no	yes	yes	fission barriers
SkP	[70]	diag	no	no	yes	yes	pairing
SLy6	[87]	full	no	no	yes	yes	neutron matter
SkI3/4	[56]	full	yes	no	yes	no	isotopic shift Pb
BSk1	[85]	diag	no	no	yes	no	deformed nuclei
PC-F1	[91]	full			no	no	
NL-Z	[92]	diag			no	no	
NL3	[93]	guess			no	yes	isovector bias

Table 1: The selection of parameterizations used throughout this paper with their actual options (‘ref.’ = first publication, ‘c.m.’ = center-of-mass correction, ‘l*s T=1’ = isovector spin-orbit, η_s = switch for spin-orbit tensor term, ‘Coul.ex.’ = Coulomb exchange in Slater approximation, ‘nuc.mat.’ = some nuclear matter properties had been included in the fit). The entry ‘guess’ for NL3 means that the c.m. correction had been used in the simple form as $E_{\text{cm}} = 30.75 A^{1/3}$. The diagonal c.m. correction for BSk1 is augmented with the recipe from [62].

shifts of r.m.s. radii in neutron rich Pb isotopes which posed a severe problem to all conventional Skyrme forces, see Section 3.1.2. BSk1 (and subsequent variants) fit exclusively to binding energies (computed in HFB), but employ an considerable pool of even-even nuclei including the majority of those with deformation. As for the c.m. correction in spherical nuclei, a simple correction for the rotational projection had been employed in deformed systems and an ad-hoc correction for the Wigner energy in $N=Z$ nuclei was applied [89]. The RMF parameterizations need no adjustment for the spin-orbit force because that is implied in the four-spinor structure of the relativistic wavefunctions [94]. Coulomb exchange is rarely included in the RMF, probably for reasons of formal similarity with the meson-field terms in the model. PC-F1 is a point-coupling model [91] whereas NL3 [95] and NL-Z [92] use the standard RMF with finite range couplings. PC-F1 as well as NL-Z are fitted with the same strategy and data pool as SkI3/4 [56], i.e. information of the electro-magnetic formfactor is included. NL3 takes care of the incompressibility and puts weight on correct isovector trends.

2.3.2 Quality on gross properties

Figure 1 shows the quality of the reproduction of energy, radii and surface thickness as delivered by three forces from our selection and for a chains of spherical semi-magic nuclei spread over the nuclear chart. The dashed horizontal lines indicate the typical average deviation which can be achieved, being approximately ± 1 MeV for the energy and ± 0.025 fm for radii and surface thickness. Note that these limits are demanding requiring, e.g., for ^{208}Pb a relative deviation from experiment of 0.006% for the energy and of 0.003% for the radii. Larger relative deviations are natural for lighter nuclei because correlation effects become relatively larger. The figures shows indeed a nearly constant absolute deviation throughout all sizes, even with a slight tendency to larger errors for small systems (particularly for the r.m.s. radii). The errors are not statistically distributed but show unresolved trends. The large isotopic and isotonic trends, for example for SkM* results, may suggest missing correlations effects. But BSk1 resolves those trends to a large extent. Thus we see here largely limits of a functional, probably with a remaining smaller part from irreducible correlations. The example indicates that the capabilities of nuclear energy functionals are not yet fully exhausted and that improvements can still be expected. For example, BSk1 was fitted with strong bias on atomic masses and performs best in that respect. The forces from the BSk family could achieve an average error of 0.7 MeV for the energies [85] which is the best result amongst the self-consistent models. Even though, the present performance of the mean

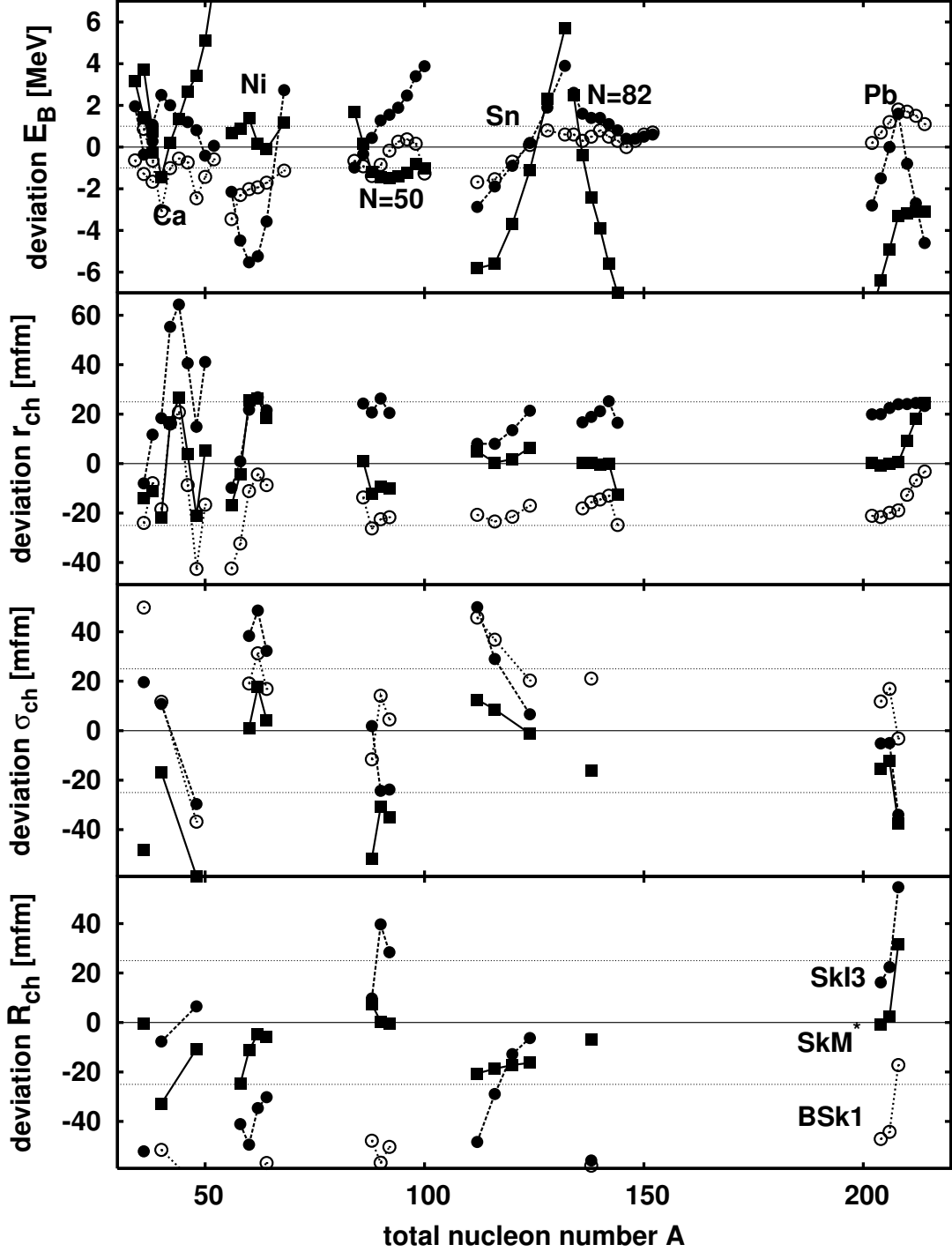


Figure 1: Distributions of deviations $\mathcal{O}^{(\text{exp})} - \mathcal{O}^{(\text{model})}$ for the four key observables in the description of nuclear ground states: binding energy E_B , charge r.m.s. radius r_{ch} , charge surface thickness σ_{ch} , and charge diffraction radius R_{ch} . Results are shown for three forces: SkM* (filled squares), SkI3 (filled circles), and BSk1 (open circles). The typical deviations which can be achieved by good fits are indicated by the band of dashed horizontal lines.

field models is already very satisfactory as can be seen from the overall quality shown in the figure. Moreover, the models provide also a reliable description of many other observables as we will see later in Section 4.

The extrapolation of gross properties, energies and radii, to infinity relates these to the key properties of nuclear matter as they are saturation point, incompressibility, and symmetry energy. There is no direct experimental access to these “observables” and thus the quality of different parameterizations cannot be discussed as directly as done here for finite nuclei. However, compliance with other extrapolations to bulk matter, particularly those within the liquid-drop model [96], is usually checked. However, some empirical evidence can be obtained from astro-physical considerations such as, properties of neutron stars. We thus have placed the discussion of nuclear matter properties in Section 4. The discussion of basic properties of nuclear matter in relation to SHF is found in particular in Section 4.2.1.

2.4 Links to other nuclear forces

2.4.1 Relation to RMF

The relativistic mean-field model (RMF) was developed to give a competitive description of nuclei in the seventies [97, 98], at about the same time as SHF, for reviews see e.g. [99, 94, 67, 100]. The RMF is conceived as a relativistic theory of interacting nucleonic Dirac fields and mesonic mean fields with the anti-particle contributions in the nucleon wavefunctions being suppressed (‘no-sea’ approximation). However, the mean-field approximation would not be valid in connection with the true physical meson exchange fields. Thus the meson fields of the RMF are effective fields at the same level as the forces in SHF are effective forces. The RMF is the relativistic cousin of SHF, and the same strategy applies: the model is postulated from a mix of intuition and theoretical guidance with parameters to be fixed phenomenologically. For the modeling, one chooses the most basic meson fields, one scalar (σ) and one vector (ω) field in the isoscalar channel, and a vector-isovector field (n). The pion does not contribute at Hartree level because the pseudo-scalar density vanishes. A second isovector meson (δ) is conceivable but was found to be ineffective [92]. The necessary density dependence is introduced through non-linear terms (cubic and quartic) in the scalar meson field [97]. This leads to a model with about the same descriptive power as SHF [22]. The indirect modeling of density-dependence was originally motivated by the aim to maintain renormalizability of the theory [99]. There are variants of the RMF which proceed differently in this respect. The point-coupling RMF (PRMF) employs covariant zero-range couplings plus non-linear terms in the density, in a way similar to SHF [101] and it reaches a competitive descriptive power [91]. Much more elaborate density dependences are sometimes discussed to enhance the flexibility of the model, see e.g. [102, 103, 104].

It is possible to draw straight connections between RMF and SHF by considering a twofold expansion, a non-relativistic (v/c) and a zero-range limit of RMF [94, 105]. The (v/c) expansion applies to the scalar density n_s and reads

$$n_s = n + \frac{1}{2m^*} \left\{ \tau - \vec{j}^2/n_0 + \nabla \cdot \vec{J} \right\} \quad (17)$$

where m^* is the nucleon effective mass. It is obvious that a kinetic term $\propto \tau$ and a spin-orbit term $\propto \vec{J}$ emerge naturally, appearing as a specific combination. The one extra parameter for the scalar coupling in RMF is equivalent to the one extra parameter for the kinetic term in the SHF functional (11c). We reiterate that the spin-orbit coupling is built into the RMF and needs no extra adjustment. This ‘spin-orbit for free’ is the major difference between RMF and SHF. Moreover, the RMF-like spin-orbit force is predominantly isoscalar which differs from the conventional SHF form ($B'_4 = 0$ in the SHF functional). An example of measurable consequences of this difference is discussed in Section 3.1.2. The (v/c) expansion suffices to map the PRMF into SHF. The conventional RMF needs as a further step

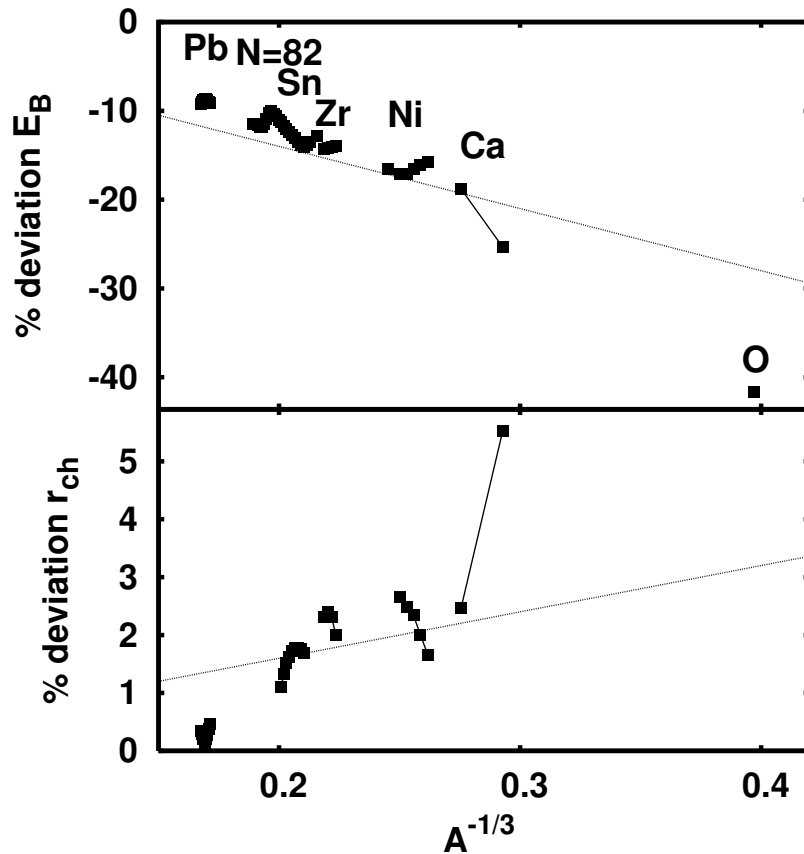


Figure 2: Distributions of deviations $\mathcal{O}^{(\text{exp})} - \mathcal{O}^{(\text{model})}$ for charge r.m.s radii and energies as computed from LDA using an equation of state for nuclear matter from BHF calculations in [107]. Beyond strict LDA, a pairing and a spin-orbit force have been added, but they have a negligible effect on the results. The fine dotted lines indicate an average trend $\propto A^{-1/3}$.

an expansion of the finite range of the meson field into a leading zero-range coupling and subsequent gradient correction. This provides formally the structure of the surface terms $\propto \Delta n$ in the functional (11c). Thus far the equivalence is straightforward. The density dependence, however, is hard to map. It is built into conventional RMF by using a non-linear meson coupling and this mechanism is very different from the SHF where a term with higher power (than two) in the density is used. PRMF with its straightforward expansion in powers of density n is much closer to SHF in that respect.

2.4.2 Relation to the Gogny model

The breakthrough of self-consistent nuclear models in the seventies has generated not only the SHF and the RMF, but also the Gogny model as a third and equally powerful option [106, 66]. The Gogny model is an effective interaction as SHF or RMF and its parameters are adjusted to empirical data. It is a non-relativistic model as SHF, but employs a finite range two-body interaction with all exchange terms correctly treated. The density dependence and spin-orbit force are added in the same functional forms as in the Skyrme functional (11c), namely as zero-range effective interactions. It could perhaps be more properly named Gogny-Hartree-Fock. The Gogny functional can be mapped formally to SHF with the general techniques of the density-matrix expansion [48] which was discussed in a more general context in the second paragraph of Section 2.1.2.

2.4.3 Local Density Approximation and conformity with BHF

The formal aspects of the derivation of an energy-density functional from *ab initio* input by means of the LDA were outlined in the third paragraph of Section 2.1.2. We will discuss here its performance in a realistic example. Starting from from BHF calculations of nuclear matter [107] we calculate binding energies and r.m.s radii of finite nuclei across the nuclear chart in LDA. Figure 2 shows the average deviation from experiment that can be achieved in this model. The good news is that LDA provides at

once a basically pertinent view of nuclear size and energy. At second glance, however, one realizes that the deviations are much too big for practical applications, e.g., in astrophysical scenarios. That failure is partially due to the fact that strict *ab initio* calculations (using only nucleon-nucleon interactions) never reach the proper saturation point of nuclear matter, leaving a principle error of about 5% on energies (see Section 1.1). However, the errors in the LDA calculation presented here exceed the deviation in energy by much more, particularly for smaller nuclei. This is a clear insufficiency of the LDA applied to finite nuclei. The key for quantitative success of LDA lies in the gradient terms which allow modeling of the nuclear surface energy. These terms are by far the most important terms on the way to the excellent description documented in Figure 1. The situation is to some extent similar to electronic density functional theory where gradient corrections enhance the descriptive power to chemical precision [108, 21]. Recall, however, that the crucial first step remains LDA which delivers a sound basis for further refinement. It is conceivable to develop a partially *ab initio* determination of the SHF functional where the density dependent terms are derived with LDA from given microscopic calculations. The problem however is that the microscopic understanding is limited so that there exists an uncomfortably large variety of predictions for nuclear matter properties, see e.g. [46]. A study in somewhat similar spirit is found in [109]. It goes beyond the strict grounds of the LDA in that it also adjusts the effective nucleon mass, and with it the kinetic terms $\propto \tau$. This yields ground state binding energies within 5% precision, better than above but still far from the goal of 0.5% reliability. Once more the need to include gradient term is clear.

For completeness, we mention that there exist also several attempts to map relativistic Brueckner-Hartree-Fock calculations onto an effective RMF, for most recent examples see e.g. [110, 111]. The formal relations are to some extent more direct than in nonrelativistic models. The basic obstacle, however, remains the fact that all nuclear *ab-initio* models up to now have a limited descriptive value.

2.4.4 Nuclear effective forces and subnuclear degrees of freedom

Although nuclear models of point-like nucleons interacting via effective forces have proven quite successful in the description of nuclear properties, the predictive power of all nuclear models is not sufficient as yet and new, more fundamental approaches are sought for, that would improve the situation. Application of QCD to nucleon systems is more frequently examined in dense (hot) matter such as the cores of compact stars where the physical conditions for a partial or full quark deconfinement are satisfied and quark effects, at least to some approximation, must be included, (see e.g. [112, 113, 114]).

The question of the effect of quark degrees of freedom in finite nuclei is still treated as tentative. Their consideration in nuclear systems at low energy challenges the application of non-perturbative QCD, but progress has been made. A recent example of a model aiming towards understanding the role of subnucleonic degrees of freedom in many-body effective Hamiltonians [115] utilizes the quark meson coupling model (QMC) in non-relativistic approximation [116]. The main idea of the model is to express the response of the quark structure of the nucleon to the nuclear environment. The interaction between the quarks of *different* nucleons (assumed to be non-overlapping bags) in the nuclear medium is represented by exchange of σ , ω and ρ mesons, with coupling constants treated as free parameters. In the zero-range limit of the model, the effective Hartree-Fock QMC Hamiltonian can be written in a form which is directly comparable with the Hartree-Fock Hamiltonian corresponding to the Skyrme effective force. The three free parameters of the QMC model, the coupling constants G_σ , G_ω and G_ρ were fitted to reproduce correctly the binding and symmetry energy and the saturation density of nuclear matter. The remaining four parameters, the meson rest masses and the bag radius R are fixed to experimental masses for the ω and ρ mesons, taking $R=0.8$ fm as an empirical value. The mass of the scalar σ meson m_σ , not known well enough from experiment, is allowed to vary in the expected region 500–600 MeV. Comparing corresponding terms in the QMCHF and SHF Hamiltonians, the Skyrme parameters $t_0, x_0, t_3, 5t_2 - 9t_1$ and t_4 can be expressed in terms for the parameters of the QMC model.

The parameters show a close resemblance to those of the SIII Skyrme force that is rather impressive.

The QMC model in the form defined in [115] did not give good properties of nuclear matter at densities above nuclear saturation density, which limited its applications to the physics of nuclear matter and compact objects. This deficiency has been removed in the current version of the model ([117] and references therein) where a density-dependent, effective nucleon-nucleon force of the Skyrme type has been derived using a new version of the QMC model that leads to an effective Hamiltonian with a density-dependent two-body force for finite nuclei and allows a treatment of high density nuclear matter consistent with relativity. It has been demonstrated that, following a procedure similar to that in [115], the Skyrme parameters t_0, t_1, t_2, t_3, t_4 and x_0 are calculated from the QMC formalism in quite close agreement with those obtained from fitting to experimental data in the SHF model with essential just one adjustable parameter, the mass of the σ meson. When the QMC Hamiltonian is used in the HF approximation for doubly-closed-shell nuclei, it yields binding energy per particle, charge and neutron radii and spin-orbital splittings for ^{16}O , ^{40}Ca , ^{48}Ca and ^{208}Pb in a very good agreement with experiment considering that the model depends only on three adjustable parameters (meson coupling constants). For application of the model far from stability, the QMC-HFB approach was used with density dependent contact interaction acting in the particle-particle channel. As an example, it yielded the position of the neutron drip-line at around $N=60$ for Ni and $N=82$ for Zr, similar to predictions provided by the SLy4 Skyrme parameterization. Calculation of two-neutron and two-proton separation energies suggests strong shell quenching at $N=28$ around $Z=14$ (proton drip-line region) and $Z=32$ (neutron drip-line region) as also predicted by HFB calculations with the SLy family [87] of Skyrme forces. Detailed application of the new QMC model to nuclear matter and neutron stars is expected in a forthcoming publication. This development can be seen as an interesting attempt to relate the Skyrme interactions to an effective model based on subnuclear degrees of freedom.

We mention for completeness that another many-body model of the nucleus, inspired by QCD quantum field theory, where the strong coupling regime is controlled by a three-body string-type force and the weak coupling regime is dominated by a pairing force, has been recently proposed [7]. This model has however so far more of conceptual than practical interest as, although it yields reasonable results for the surface density of finite nuclei, and correct properties of symmetric nuclear matter, it needs more development before it is applicable to a wide range of properties of finite nuclei.

3 Applications to finite nuclei

3.1 Static properties

Basic bulk properties such as ground state binding energies and radii of magic and only a few semi-magic nuclei have been used as input to the adjustment of the parameterizations. The quality achieved in calculations of these properties in a broad range of nuclei is very good, as discussed in Section 2.3.2. Thus experience shows that SHF and RMF have a good interpolating power in the valley of stability but extrapolations are much less certain. It is the great challenge for the further development of mean field models to accommodate simultaneously more data in order to enhance the predictive power into unknown regions such as nuclei appearing in various processes of nucleosynthesis or super-heavy elements. One option is to investigate more detailed ground-state observables as a part of this effort. This will be discussed in this Section. Going deeper into details is a very critical test of mean field models and it often turns out that one needs to go beyond a mere mean-field description. This will be sketched briefly in Section 3.4 dealing with correlations from soft modes. Another option is to look for excitation properties in a regime still accessible to mean-field models. That will be addressed in Section 3.2.

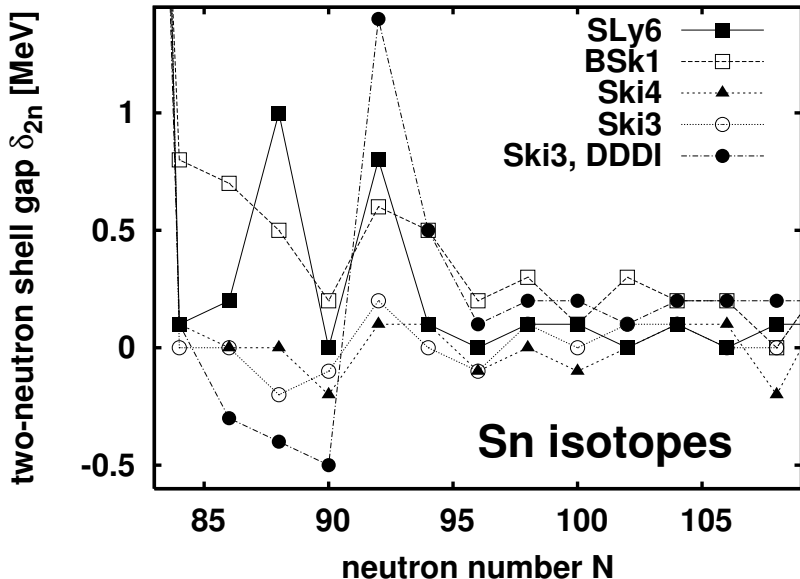


Figure 3: The two-neutron shell gap δ_{2n} along the chain of neutron rich exotic Sn isotopes computed in spherical mean field calculations for various SHF parameterizations.

3.1.1 Trends of ground state binding energies

Ground state binding energies as such are very well described in properly adjusted effective functionals, as discussed in Section 2.3. A closer look at Figure 1 reveals that the remaining discrepancies between theory and experiment are not statistically distributed but show systematic and as yet not well understood trends. It is to be expected that energy *differences* constitute a much more critical observable. In fact, we will see in Section 3.4 that correlations can play a role there. In the present Section, we concentrate on the basic mean field effects. The observed variations will remain typical, even if polarization and correlation are to be added later.

Energy differences give indirect access to underlying pairing and shell structure. The odd-even staggering of binding energies carries information on the pairing gap although care has to be taken to sort out effects due to interferences with shape fluctuations [86, 73]. Differences between even-even nuclei are related to the shell structure at the Fermi energy. The first order difference yields the two-nucleon separation energies, $S_{2n} = E(Z, N) - E(Z, N - 2)$ and $S_{2p} = E(Z, N) - E(Z - 2, N)$. Shell gaps are associated with jumps in the separation energies (as long as shape fluctuations are absent, see Section 3.4). These jumps appear in a more pronounced manner as steep spikes in the second differences, the two-nucleon shell gaps

$$\delta_{2n} = E(Z, N + 2) - 2E(Z, N) + E(Z, N - 2) \quad , \quad \delta_{2p} = E(Z + 2, N) - 2E(Z, N) + E(Z - 2, N) \quad . \quad (18)$$

These differences play a crucial role in identifying magic shell closures [118] and ‘can serve as indicators for waiting points in the r -process [119]. However, they have to be viewed with care for two reasons: first, the relation to the underlying single-particle spectrum can be masked by shape effects, and second, they are a measure of a single shell gap and not of the level density in a whole region around the Fermi energy. Thus a study of two-nucleon shell gaps should be combined with complementary considerations of shapes and level structure. An example for shape fluctuations is discussed in Section 3.4. The computation of level densities is discussed in Section 3.1.4 with the example of shell stabilization of super-heavy elements.

Shell effects play a crucial role for estimating the abundance of elements as produced in the r -process and traditional mean field models seem to call for corrections [120]. Before going that far, one has first to explore the predictive power or, more properly, the variance of existing models. Figure 3 shows the two-neutron shell gaps δ_{2n} along the neutron rich Sn isotopes for a variety of SHF parameterization. This chain plays a crucial role in the r -process and δ_{2n} is a useful indicator, particularly for differences

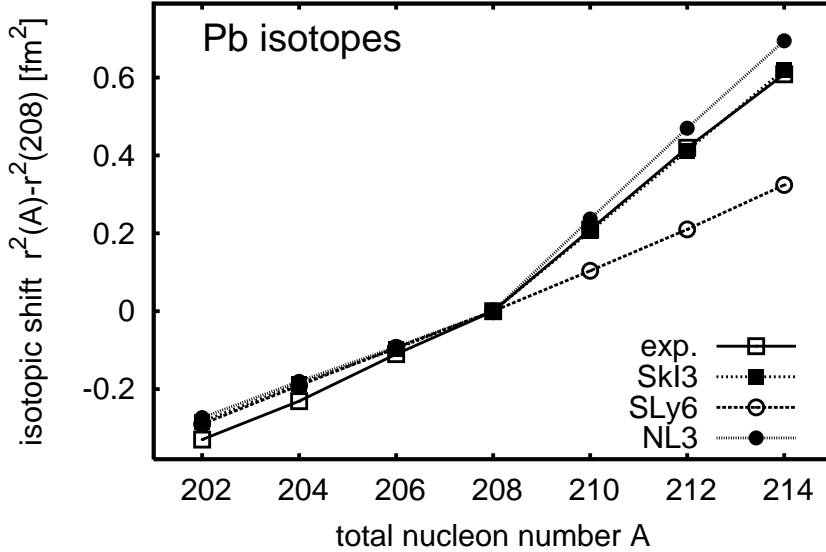


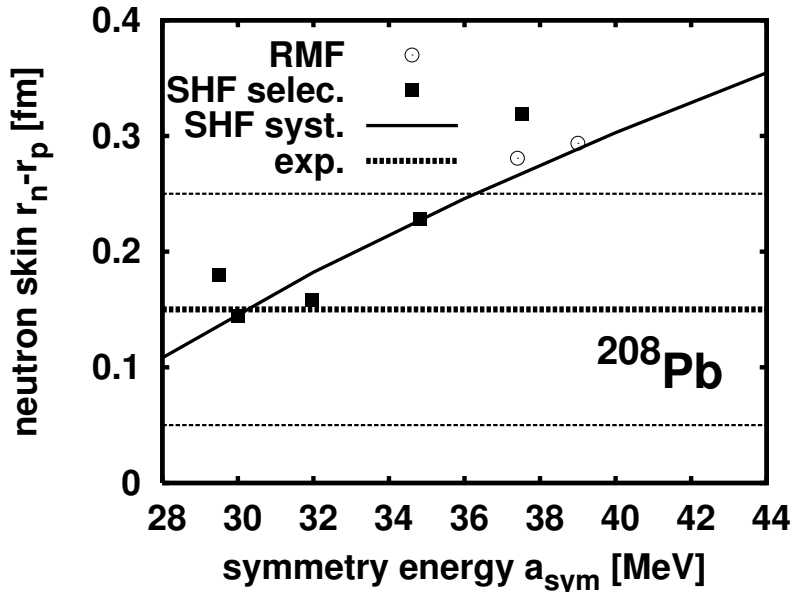
Figure 4: The isotopic shifts of charge r.m.s. radii, $r^2(^A\text{Pb}) - r^2(^{208}\text{Pb})$, for the chain of Pb isotopes around double magic $^{208}\text{Pb}_{82}^{126}$. Results for the SHF parameterizations SLy6, SkI3, and the RMF parameterization NL3 are compared with experimental data [121].

between the parameterizations. One realizes immediately that the different SHF parameterizations yield very different predictions. Not only that, the variation of the pairing treatment adopted (see Section 2.2.4) has an equally dramatic effect. This example shows that predictions of waiting points from mean-field model are still rather vague. It is a great challenge to improve the predictive power of the models. This calls in particular for a better control of shell structure as well as of pairing. The strategy for improvement is to take more and more observables into consideration in fitting of the Skyrme parameters. Potential additions will be addressed briefly in the following parts of the present Section.

3.1.2 Spin-orbit effects

New data from exotic nuclei reveal often hitherto unexplored features of self-consistent mean-field models. One prominent example is provided by the isotope shifts of charge radii in neutron rich Pb isotopes [121]. The trend shows a pronounced kink at doubly magic ^{208}Pb , see Figure 4. It was found that SHF fails to reproduce this kink but continues uninterrupted with the slope from the isotopes below ^{208}Pb [122]. The example of SLy6 in Figure 4 is typical for all conventional SHF parameterizations, i.e. those with fixed $B'_4 = 0$ in the SHF functional (11e). All RMF parameterizations, on the other hand, deliver the observed discontinuity [123], see the example of NL3 in Figure 4. A comparison of the models in detail revealed the mechanisms underlying this systematic difference [56, 124]. It was found that the spin-orbit splittings of high lying neutron shells are substantially larger in SHF than in RMF. As a consequence, the $2g_{9/2}$ neutron level which is gradually filled when adding neutrons to ^{208}Pb , is more deeply bound and has a smaller radius in SHF. This is the level which determines the outer tail of the density for $N > 126$. Thus the RMF produces larger neutron radii in isotopes above ^{208}Pb than SHF. The proton radii, in turn, are stretched due to the large nuclear symmetry energy which is, in fact, particularly large in the RMF (see Figure 18). And that is what produces in the RMF results the kink above ^{208}Pb , in agreement with the data. Now the source of the difference between SHF and RMF is traced back to the difference in the spin-orbit splitting. This difference, in turn, can be associated with the different isovector structure of the spin-orbit coupling in RMF and conventional SHF, see Section 2.2.2. The RMF corresponds to a spin-orbit functional without isovector terms, for which $B_4 + B'_4 \approx 0$ whereas the conventional SHF form has $B'_4 = 0$. A minor extension of the SHF to the full form (11e) allows to reproduce the kink also with SHF. The Figure 4 shows the force SkI3 as example in which the relativistic variant $B_4 + B'_4 = 0$ was chosen [56]. It seems that the isotopic shifts in the Pb region are the

Figure 5: Neutron skin, $r_{\text{neut}} - r_{\text{prot}}$ for ^{208}Pb for various parameterizations, drawn versus the symmetry energy a_{sym} . Results for selected parameterizations (RMF and ‘SHF selec.’) and the trend from systematically fitted SHF forces (‘SHF syst.’) are shown. The experimental value is indicated by heavy dotted horizontal line [125]. The assumed error on the data is indicated by faint dotted lines.



by far the most sensitive observable for the isovector spin-orbit force. Many other observables which are, in principle, sensitive to shell effects, as e.g. level densities in super-heavy elements (see Sections 3.1.4 and 3.1.5) did not yet show such specific evidence.

3.1.3 Neutron radii

Neutron radii provide additional very valuable information complementing the rich pool of data from charge radii. Unfortunately, their experimental determination is more model dependent than for charge radii because the strong interaction is involved [126]. More experimental information on neutron radii would improve models in several respects. For example, there is a close connection between the equation of state of neutron matter and the neutron r.m.s. radius of ^{208}Pb , see [127] for the SHF and [128] for the RMF. Other interesting phenomena related to the neutron density are the neutron skins defined as the difference between neutron and proton radii (or even neutron halos developing towards the drip lines [84]). One can establish a direct relation between isovector forces and the neutron skin. A systematic variation of SHF parameterizations with respect to all conceivable bulk properties has shown that there exists a unique one-to-one relation between neutron skin and symmetry energy a_{sym} [129]. This is demonstrated in Figure 5 for ^{208}Pb . The symbols show results for a variety of mean-field parameterizations. They line up in a way which indicates a systematic increase of the skin thickness with increasing a_{sym} . In order to check that trend thoroughly, a set of SHF forces was fitted all to the same set of ground state data but with an additional constraint on a_{sym} that was systematically varied [129]. The result corroborates the trend and shows an almost linear connection between neutron skin and a_{sym} . Such a unique correspondence can be established for all nuclei. The trends are particularly pronounced in neutron rich exotic nuclei. Furthermore, neutron radii have strong influence on the reaction cross section of exotic nuclei. This indicates that a correct symmetry energy and its density dependence, as discussed in Section 4, is crucial for understanding nucleosynthesis and some other astrophysical phenomena dependent on reaction rates involving neutron rich nuclei.

A different and complementing access to neutron radii has been brought up in [130] by exploiting a combined knowledge about the position of the Gamow-Teller resonance and of the isobaric analogue state.

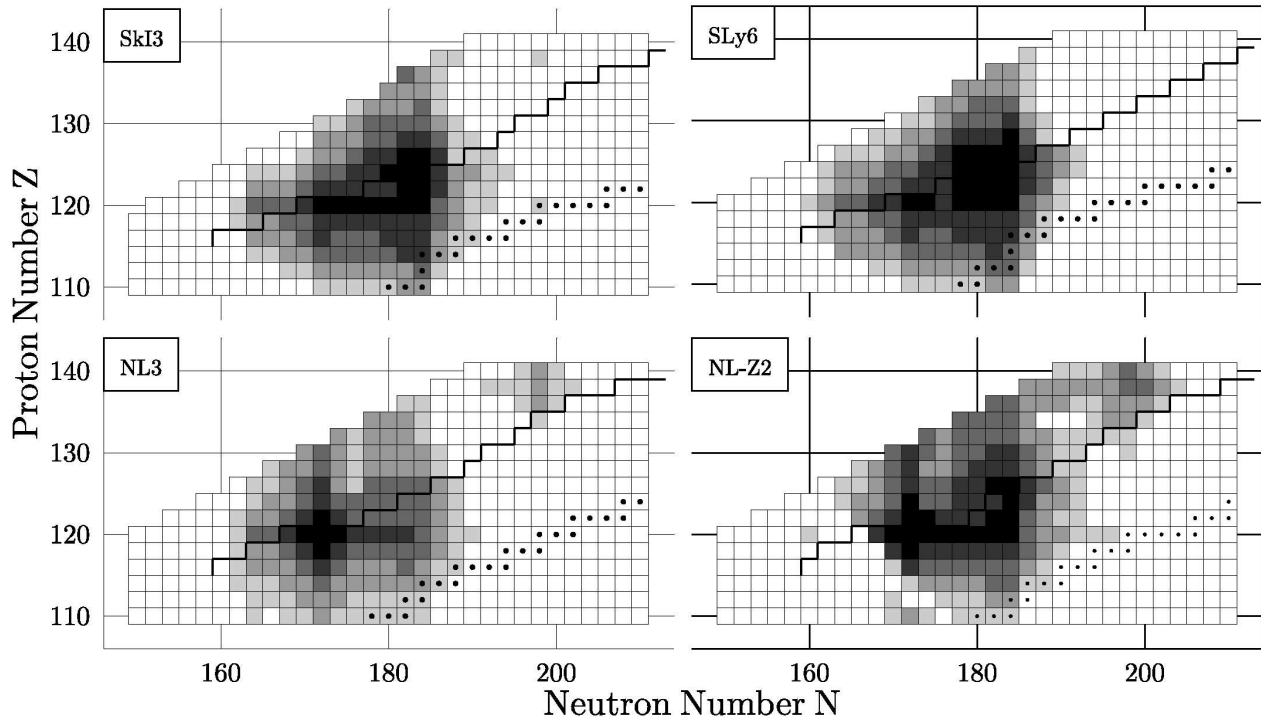


Figure 6: The shell correction energies (19) of super-heavy elements for various SHF and RMF parameterizations as indicated. There are five gray values for five intervals of width 3 MeV. The black boxes stand for corrections below -12 MeV, the next gray value for -9 to -12 MeV and the lightest gray for 0 to -3 MeV. (Adapted from [131].)

3.1.4 Super-heavy elements

The key question in the study of super-heavy elements is their stabilization, through shell effects, against spontaneous fission. A first estimate of where stability may be found can be drawn from the shell correction energy given approximately as

$$E_{\text{shell}} = \sum_{\alpha} w_{\alpha} \varepsilon_{\alpha} - \int d\varepsilon g(\varepsilon) \quad (19)$$

where the ε_{α} are the single particle energies, w_{α} the associated multiplicities, and $g(\varepsilon)$ represents a smooth energy distribution generated from the set $\{\varepsilon_{\alpha}\}$ by an appropriate shell averaging procedure which has to include continuum states in case of SHF spectra (for details of the prescription see e.g. [131]). Figure 6 shows a summary of shell correction energies for the landscape of super-heavy elements. Note that the results are based on spherical mean-field calculations which somewhat underestimates stabilization in case of deformed nuclei. One finds broad islands of shell stabilization rather than narrow and deep valleys as they are typically found for lighter nuclei. This means that the notion of magic nucleon numbers fades away for super-heavy nuclei. This is due to the fact that the level density increases with $A^{-1/3}$ and with it the gaps in the spectrum which are the key features for defining magic shells. Seen from that perspective, it seems rather surprising that such large shell correction energies still emerge. The reason is a separation of states with low from those with high multiplicity. There arise broad spectral regions which carry only a few low-multiplicity states. These inhibit large spectral gaps but still allow for large shell corrections in a broad range of isotopes. The emergence of large regions of stable nuclei is good news for the potential experimental accessibility as it should not be necessary to hit precisely a single longer-lived final isotope. Rather there is a broad choice of more stable final isotopes in a heavy-ion fusion experiment which enhances the chances for finding successful collision

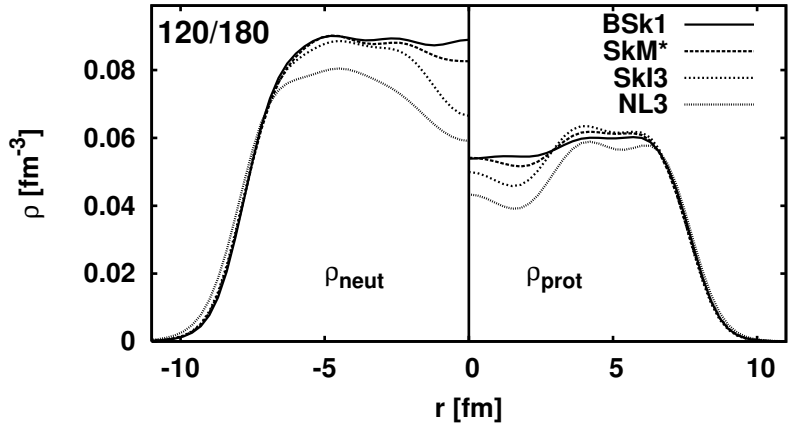


Figure 7: The proton (right) and neutron (left) density distributions for the super-heavy element $Z=120$, $N=180$ for different Skyrme forces and one RMF parameterization as indicated.

combinations to produce them. We are still a long way from assessing the super-heavy elements and even farther away from measuring their detailed properties. Let us, nonetheless, speculate a bit about their density distribution. Strong Coulomb repulsion should reduce the proton density in the interior producing a more or less deep dip as indicated in Figure 7 for the fictive nucleus $^{300}\text{XX}_{120}^{180}$, where proton densities show indeed all some dip at the center. However, this dip differs very much between the different parameterizations. It is interesting to note that the neutron distributions show the same succession of dip depths. The depth increases with decreasing effective mass and BSk1, with effective mass ≈ 1 , has practically a flat distribution. This indicates that the variation of dips is a shell effect. Forces with low effective mass tend to cut a hole in the nuclear center. For proton densities, the situation is less clear with the simple Coulomb effect probably well seen for BSk1 and amounting to about 10% reduction at the center. Larger reductions are induced by shell effects. The results of figure 7 are typical for region of nuclei with $A \sim 300$ with similar effects predicted and discussed for $^{292}\text{XX}_{120}^{172}$ in [118]. Taking the predictions bit further, the next region of shell stabilization, around $^{480}\text{XX}_{160}^{320}$ [132], opens the possibility of bubble nuclei which are almost proton-empty at the center.

3.1.5 Fission barriers

Spontaneous fission becomes a crucial decay channel for actinides and super-heavy nuclei. There exists a wealth of information about fission in actinide nuclei, for a review see [133]. The most remarkable feature is the double-humped barrier. The ground state is usually prolate deformed with a typical deformation of $\beta_2 \approx 0.3$. As deformation increases, the energy passes a first (inner) barrier which leads to an elongated fission isomer at around $\beta_2 \approx 0.9$ and finally goes to fission through a second (outer) barrier. The first barrier explores triaxial deformation which lowers the barrier by about 3 MeV as compared to the axial value. The second barrier explores reflection-asymmetric shapes. The double-humped fission barrier of ^{240}Pu has often served as a benchmark for mean-field models, see Ref. [134] for results obtained using Skyrme interactions, [135] using Gogny forces and [136, 137] for the RMF, see also [138]. Collective correlations (see Section 3.4) modify the fission path significantly [139, 39]. The typical corrections are a lowering by 0.5–1 MeV of the first barrier and about by 2 MeV for the second. The triaxial shape lowers the first barrier by another 1–2 MeV such that both (axial) barriers are subject to correction by about 2–3 MeV.

Figure 8 compares calculated (SHF and RMF) and experimental heights of the barriers. One has to take into account that the theoretical values are deduced from axially symmetric shapes without triaxial and correlation corrections, however several conclusions can be safely drawn. At first glance, we see that both models yield the correct order of magnitude for the barriers, which is not a trivial achievement in view of the various counteracting effects (shell effects versus collective trends from symmetry and surface energy). On closer inspection, we see that the RMF yields systematically lower barriers than

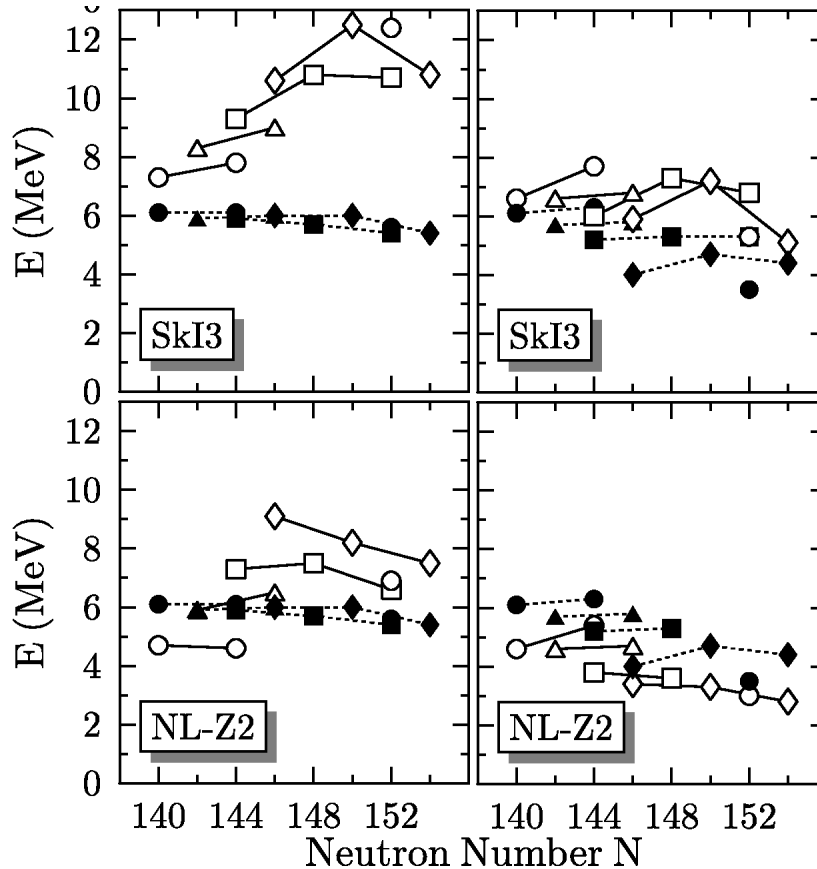


Figure 8: The first (left panels) and second (right panels) fission barriers from axial and reflection-symmetric calculations with SkI3 or NL-Z2. Th ($Z = 90$), U ($Z = 92$), Pu ($Z = 94$), Cu ($Z = 96$), and Cf ($Z = 98$) isotopes are denoted by open circles (for $N = 140, 142$), open triangles, open squares, open diamonds, and again open circles ($N = 152$), respectively. Experimental data (full symbols) are taken from [140]. Data points for the same element are connected by lines.

SHF. Both are generic features which persist when comparing a broader selection of parameterizations [141]. Accounting for typical reductions of about 2–3 MeV, the RMF tends to underestimate fission stability. The SHF looks more successful for the first barrier but also predicts second barriers somewhat too low.

The fission landscape of super-heavy nuclei differs from that in the actinides through the disappearance of the fission isomer and the second barrier. On the prolate side, only the first barrier needs to be considered. For the heaviest nuclei there may be an alternative fission channel which goes through oblate and then triaxial shapes [142]. We confine the discussion here to the axially symmetric first barrier at the prolate side. The systematics of barriers for the landscape of super-heavy elements and for two mean field models is shown in Figure 9. The results are typical for a broader variety of forces [141]. All models and forces agree that there is a regime of low fission barriers around $Z = 110$ and that the (axial) barriers increase again when going towards $N = 184$. There are again significant differences in that RMF yields systematically lower barriers than SHF. Taking into account a possible lowering by triaxiality and correlations, we conclude that the RMF predicts fission instability practically everywhere in that landscape. The SHF provides a much more optimistic outlook for ultra-heavy element stability, qualitatively in accordance with experiments which indeed managed to identify nuclei up to $Z = 116$ [143, 144, 145]. The reason for this systematic difference has not yet been identified uniquely. It comes probably from several sources, amongst them the much higher symmetry energy in the RMF and the somewhat different shell structure.

3.2 Dynamic properties

Self-consistent mean-field models allow also dynamical applications. From the given energy functional, one can equally well derive time-dependent mean-field equations. The SHF functional 11 provides already the time-odd couplings involving current \mathbf{j} and spin-density $\boldsymbol{\sigma}$ which are now activated in

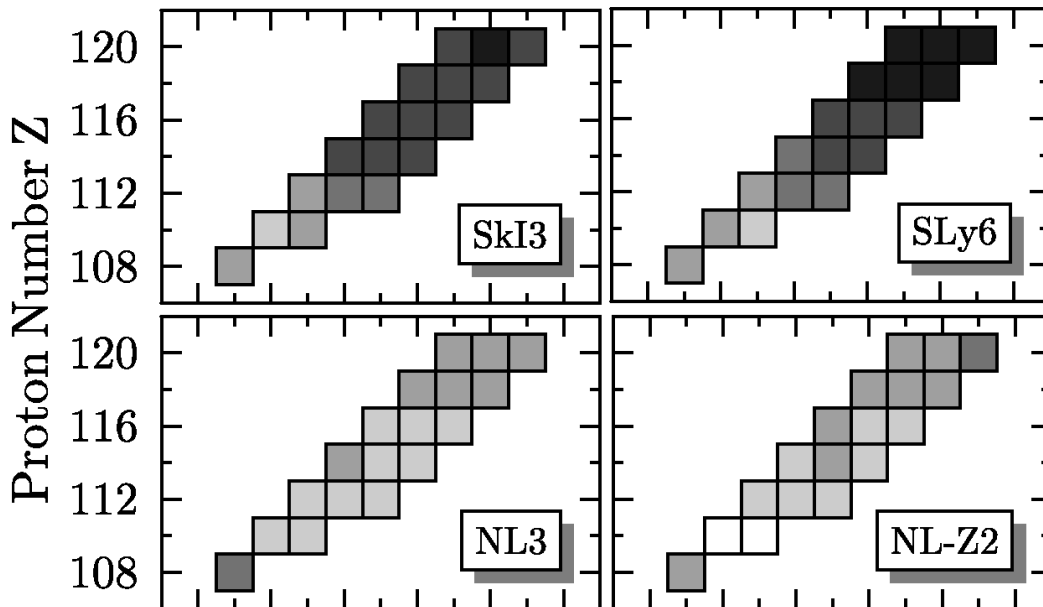


Figure 9: Fission barriers of super-heavy elements for various SHF and RMF parameterizations. The grey scale proceeds in bins of 2 MeV width. The black boxes indicate barriers higher than 12 MeV and the lightest grey denotes barriers between 2–4 MeV. (Adapted from [141].)

dynamical situations with non-vanishing net flow. The dynamic extension of SHF is often called time-dependent Hartree-Fock (TDHF) and it has enjoyed great attention three decades ago as a tool for analyzing the principle mechanisms of heavy-ion collisions, for reviews see [146, 147]. But TDHF covers much more. Many excitation properties can be derived from TDHF. An important class of excitations deals with small amplitude motion, i.e. in the limit of harmonic oscillations. This applies to the basic nuclear resonance modes (e.g., giant resonances or Gamow-Teller resonances), in fact, any excitation in the spectral range from 2–30 MeV. The small amplitude limit of TDHF yields the much celebrated random-phase approximation (RPA). Examples in that regime will be discussed in Sections 3.2.1 and 3.2.2. Low-energy excitations are associated with soft modes (quadrupole surface oscillations, rotation, c.m. motion) and explore large amplitudes. These modes proceed very slowly and can be dealt with in various adiabatic approximations. Examples will be discussed in Section 3.2.4 and 3.4.1, and the example of fission was already sketched in Section 3.1.5. And there is finally the regime of heavy-ion collision which employs large amplitudes and is not necessarily slow. This will be discussed in Section 3.2.3. In all cases, one should consider, in principle, an inclusion of pairing in a TDHF with BCS states (TDHFB). This is rarely done at the level of full TDHFB. It is a standard choice in the adiabatic situations. The small amplitude limit of TDHFB yields the quasi-particle RPA (QRPA) which is the method of choice for computing excitations in non-magic nuclei.

3.2.1 Giant resonances

Prominent features of the nuclear excitation spectrum are the giant resonances of which the most striking is the isovector dipole resonance. The isovector dipole couples strongly to photons and thus provides the largest photo-reaction cross sections. A correct description of these is crucial for estimating astrophysical reaction chains. The isovector dipole excitations can be described within a mean field theory utilizing a time-dependent mean field in the limit of small amplitudes, often called the random-phase approximation (RPA). There exists a large body of RPA calculations in the context of self-consistent models, for SHF see recent compilations [148, 129], for Gogny forces [149, 150], and for the RMF [151, 152]. The dipole spectra in heavy nuclei show one prominent resonance peak with some

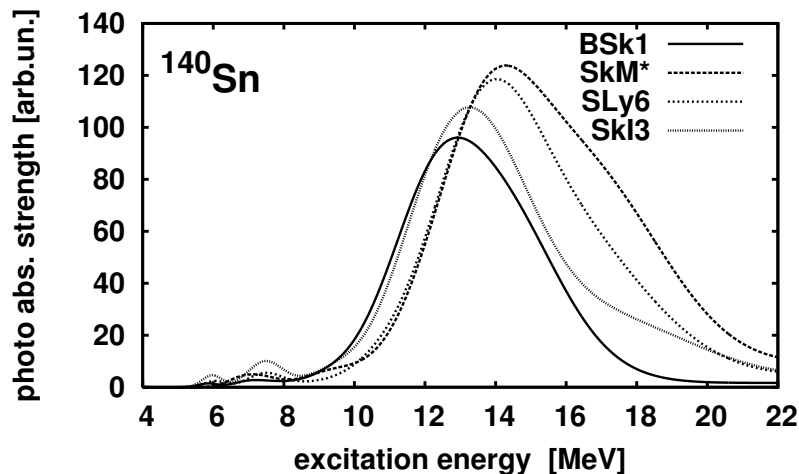


Figure 10: The photo-absorption strength for ^{140}Sn computed with RPA using four different Skyrme parameterizations as indicated. The self-consistent RPA techniques from [157, 158] have been used. The spectra are folded with a Gaussian width of $\Gamma = (E_n - \varepsilon_{F,\text{neutr}}) * 0.2$ MeV to simulate escape and collisional broadening.

small broadening due to neutron escape, Landau damping and two-body correlations [153, 154, 155]. This peak is well described by most of the existing mean-field parameterizations. A small part of dipole strength is found at lower energies giving rise to what is called a pygmy resonance [156]. The pygmy peak is sensitive to shell structure and depends strongly on the particular mean field model. The spectral fragmentation increases towards lighter nuclei and when going towards the drip lines.

The giant dipole resonance in ^{208}Pb shows one clear, although broad, peak and can be well characterized by the peak position. It is interesting to see how this peak position depends on the bulk properties of the model. One expects naturally a strong relation to the symmetry energy a_{sym} which is associated with a given parameterization (see Section 4.2.1). For such studies, we have developed a set of SHF parameterizations where one bulk parameter was fixed in addition to the otherwise same fitting to gross properties of a selection of finite nuclei [129]. This systematics had already been used for the discussion of neutron radii in Figure 5. It is now applied to a study of the giant dipole resonance. Figure 11 shows the trend of the peak energy of the resonance in ^{208}Pb with varied symmetry energy. The result is at first glance surprising. The energy decreases with increasing a_{sym} . One would have expected the opposite trend because a_{sym} represents the spring constant for isovector motion. Note, however, that a_{sym} represents a feature at bulk equilibrium density. The actual nuclear density varies about that value and it is significantly lower than that in the nuclear surface where the transition density ($\propto \nabla\rho$ [159]) of the resonance mode has its maximum. We have to consider the density dependence of a_{sym} . It can be characterized by the slope at bulk equilibrium, i.e.

$$a'_{\text{sym}} = \left. \frac{d}{dn} a_{\text{sym}} \right|_{n=n_0} . \quad (20)$$

The trend of a'_{sym} is shown in the lower panel of Figure 11. The slope is basically positive and it increases dramatically with increasing a_{sym} . The subsequent decrease of the effective symmetry energy with decreasing density more than counterweights the increase of the bulk-equilibrium value. Thus we find at the end this curious counter-trend observed in the upper panel of Figure 11. As an example, we show in Figure 10 the predicted photo-absorption spectra for the neutron rich exotic nucleus ^{140}Sn . Its neutron emission threshold $\varepsilon_{F,\text{neutr}}$ is about 4 MeV. The spectra show the dominant giant dipole resonance with several well separated pygmy resonances a few MeV above threshold. The four chosen Skyrme parameterization all reproduce stable ground state properties well and yield comparable giant dipole resonance peaks in ^{208}Pb . However the predictions in ^{140}Sn differ visibly, particularly what the pygmy strength is concerned. The proper description of these details in fragmented spectra and for low-lying dipole strength remains a great challenge to mean-field models and requires further thorough exploration.

Despite the good agreement with experiment in heavy nuclei, a most puzzling feature appears for the

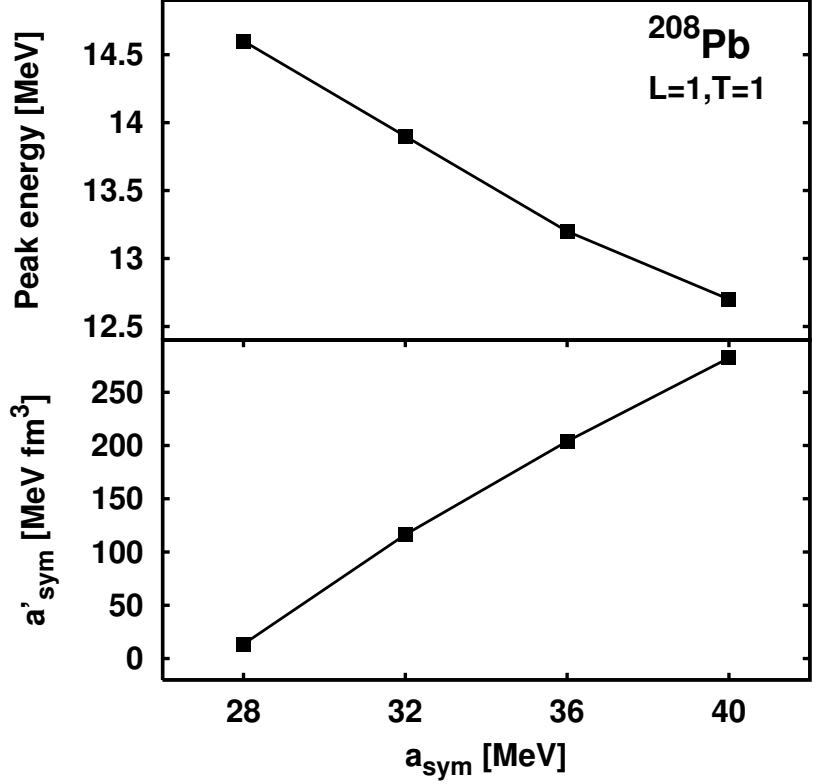


Figure 11: Upper panel: Energy of the giant dipole resonance peak in ^{208}Pb as function of the symmetry energy a_{sym} . The resonances were computed with a set of Skyrme forces where a_{sym} was systematically varied [129]. Lower panel: The slope of density dependence for symmetry energy.

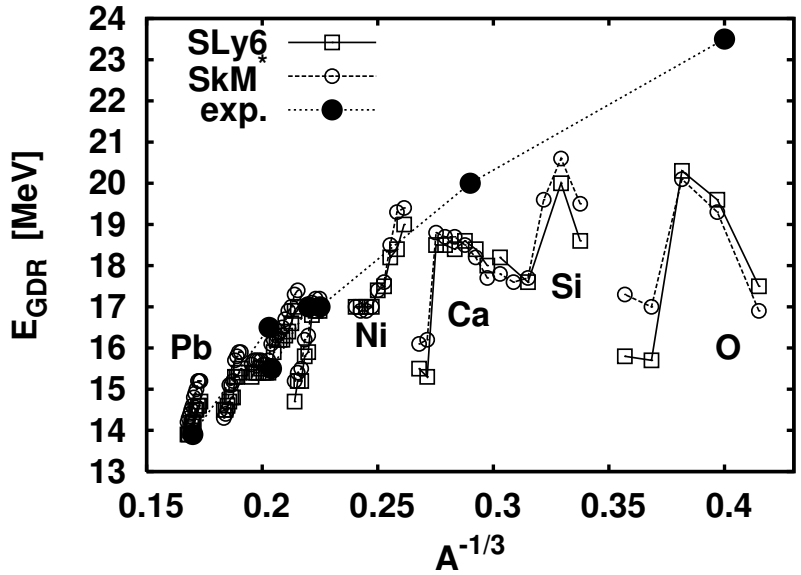


Figure 12: The average peak position of the giant dipole resonance in a broad range of spherical nuclei drawn versus $A^{-1/3}$ (which is proportional to the inverse radius). Results are shown for two different Skyrme forces as indicated and compared with experimental data where available.

average peak position in the giant resonance region on moving to light nuclei. The average resonance energy is underestimated dramatically and systematically for light nuclei, such as e.g. ^{16}O and as yet no SHF parameterization can describe adequately the resonance both in ^{208}Pb and ^{16}O [129]. As a first step towards an understanding of this problem, we illustrate in Fig. 12 the trend of the average resonance frequency over a broad range of nuclei from ^{16}O to ^{208}Pb . Results for two conventional SHF forces, typical for any other force investigated so far, are shown. They are drawn versus $A^{-1/3}$ which helps to spot trends. The Goldhaber-Teller model predicts an $A^{-1/3}$ law while the Steinwedel-Jensen model indicates an $A^{-1/6}$ dependence [160] while experiment is closer to the $A^{-1/6}$ law. The SHF theoretical predictions deviate from both these estimates and find a constant resonance energy for the light nuclei (large $A^{-1/3}$). The clear deviation for $Z < 28$ nuclei is presently unexplained, thus SHF predictions can only be considered acceptable for $Z \geq 28$.

So far, we have discussed the spectra of small-amplitude modes. The lowest excitations in nuclei are often related to large amplitudes, e.g. rotations and soft quadrupole vibrations. Time-dependent mean-field theory is also capable to describe these large amplitude modes. The case of heavy-ion collisions is discussed in the now following Section. Low-energy spectra require some additional steps for proper re-quantization of the semi-classical mean-field dynamics. This will be discussed in Section 3.4, particularly in the part 3.4.3.

3.2.2 Gamow-Teller resonances

Giant resonances (see Section 3.2.1) and low-energy quadrupole modes (see Section 3.4.3) access mainly the flow part of the time-odd functional in subequation (11c) of the Skyrme functional. This part is basically fixed by Galileian invariance. Excitations with unnatural parity ($\Pi = (-1)^{L+1}$) probe the other time-odd parts in subequation (11d) which are not yet so well fixed. Thus unnatural parity states carry a lot of new information. In this family, the dominant isoscalar excitations have magnetic dipole ($M1$) structure. Orbital $M1$ strength is related to the nuclear scissors mode which has been observed by [161], see [162] for a review. The most prominent isovector mode is the Gamow-Teller (GT) resonance, for a review see [163]. The spectrum in the GT channel plays a role in computing the probabilities for β -decay which, in turn, is a crucial ingredient in the reaction chains of the r -process. Furthermore, the energy distribution of GT strength is a vital information needed for calculation of electron capture rates at densities and temperatures appropriate for core-collapse supernovae models. Existing shell model calculations ([164, 165] and references therein) are not applicable for all needed neutron-heavy nuclei and extrapolation techniques have to be applied. Self-consistent SHF models are not subject to this limitation and may prove to be a versatile tool in this context. Thus a proper modeling of these modes is a desirable feature in a self-consistent description.

While many time-odd terms contribute to isoscalar $M1$ excitations, GT excitations are determined exclusively by the time-odd isovector spin-spin part of the effective interaction, see the terms $\propto C'_0, C'_2$ in eq. (11d). These terms are only loosely fixed in usual parameterizations at present. Studies of GT resonances may supply useful data for the further development of the forces. Fully self-consistent calculations in the SHF framework are still rare, for a thorough discussion of previous work see [166]. The volume properties of the residual interaction in the GT channel are characterized by the Landau parameter g'_0 [38]. The lack of predictive power becomes obvious from the fact that different SHF parameterizations shows a large spread just for this parameter. The g'_0 becomes, e.g., for the present selection of forces: SkM* \leftrightarrow 0.31, SkP \leftrightarrow 0.06, SLy6 \leftrightarrow -0.04, SkI3 \leftrightarrow 0.20, SkI4 \leftrightarrow 1.38, BSk1 \leftrightarrow 0.22. Note that negative Landau parameters signify an instability of the ground state, for g'_0 a spin-isospin instability. It is to be reminded, however, that the volume parameters serve only as a first guidance. The actual situation in finite nuclei is additionally much influenced by the surface terms, in the GT channel then by the C'_2 term in eq. (11d). There exist already a few attempts to look for more suitable forces. The force SGII has been tailored for this particular purpose [167] and a Skyrme force SkO'

was found to perform fairly well in the GT channel [168]. Large scale systematic studies and a proper adjustment of these features are necessary and have still to come. There exist also recent studies of GT states within the RMF, see e.g. [169]. The advantage is here that RMF has less uncertainties in the spin channel. It seems, however, that the modeling of the density-dependent couplings leave some freedom yet to be fixed.

3.2.3 Heavy ion collisions

As mentioned above, fully fledged TDHF with Skyrme forces helped a lot to elucidate the principles of heavy-ion collisions [146, 147]. It gave information on basic properties such as the bifurcation between fusion and inelastic scattering at a certain critical impact parameter and the typical pattern of a Wilczynski plot (double differential cross section with respect to scattering angle and energy). The early studies were all hampered by restrictions and approximations due to numerical limitations. One of the open problems was that too little dissipation emerged from these calculations thus underestimating fusion cross sections and energy loss in inelastic collisions. A large part of dissipation could be regained including the spin-orbit force properly [170, 171]. Explicit dissipation mechanisms through dynamic two-body correlations beyond mean-field have been intensively investigated, as reviewed in [172]. But the full degrees of freedom of a pure TDHF description had not been explored so far. Only recently has ever-increasing computing power allowed fully fledged TDHF calculations without compromises to be explored. Glimpses of a new generation of TDHF studies are emerging, offering in assessing more precisely the borderline between mean field and correlation effects. [155, 173].

3.2.4 Rotational bands

Nuclear spectra exhibit extended rotational bands which disclose a variety of interesting phenomena, such as the breakdown of pairing due to the coriolis force, or the phenomenon of backbending caused by the crossing of two rotational bands with very different moment of inertia. It is no surprise then that one can find a large body of literature on that topic, for some experimental reviews see [174, 175, 176].

Rotation is a large amplitude motion for which TDHF is the appropriate tool. However, rotational symmetry allows to simplification of the treatment. A transformation from the intrinsic to the laboratory frame shows that the rotating wavefunction is correctly described by constrained Hartree-Fock (CHF) calculation in which the mean-field Hamiltonian \hat{h} is augmented by a constraint for each angular momentum \hat{J}_i , i.e.

$$\hat{h} \longleftrightarrow \hat{h} - \omega_i \hat{J}_i \quad (21)$$

where ω_i is the Lagrange parameter (corresponding to the associated rotational frequency) and \hat{J}_i is a component of the total angular momentum orthogonal to one of the principle axes of the deformed nucleus. One considers usually axially symmetric nuclei and the rotation axis has then to be chosen orthogonal to the symmetry axis. This then yields unavoidably a fully triaxial problem. Moreover, time-reversal symmetry is broken by the rotation which complicates the treatment of pairing. Although conceptually straightforward, the technical side of these CHF calculations for rotational bands is extremely involved, for details see e.g. [38]. Nonetheless, the high interest in rotational dynamics has motivated several groups to admirable efforts in that direction leading subsequently to the large body literature as mentioned above. A detailed report would go far beyond the limits of the present review.

Mean-field theories are well suited to deal with that phenomenon since the high quantum number involved validate the semi-classical limit which is implied in TDHF and self-consistency eliminates the need for further free parameters. SHF was employed in early studies on rotating nuclei, see e.g. [177], and since then a widespread literature about rotational bands on the grounds of mean-field models, mainly SHF emerged, for reviews see e.g. [178, 179]. As discussed above, the Skyrme functional is somewhat uncertain in the time-odd domain, particularly concerning the spin couplings. This carries

over to the rotation studies, because rotation breaks time-reversal symmetry and thus accesses the time-odd components of a model. The RMF method, is thought to be better suited to analyzing spin properties since they are automatically included within the lower components of the Dirac wavefunctions, has been used also, however the computations are much more involved than in SHF, see for example [180].

3.3 Nucleosynthesis

It is the present understanding that all elements in nature, apart from ^1H , ^2H , ^3He , ^4He and ^7Li which originated from the Big Bang [181], are made during stellar evolution and stellar explosions. The main influence of nuclear physics on element synthesis is given in calculation and predictions of cross sections of nuclear reactions and decay rates in the stellar environment. This environment is not stable but changes on a timescale much longer than the typical time scale of the strong and weak interactions, dominating nuclear transmutation. The environment, characterized by density, temperature and properties of nuclei present in the medium is crucial for type, rate and products of nucleosynthesis. This Section reviews the role of the Skyrme interaction in simulations of the two major ways of creation of heavy elements, the r- and rp- processes.

3.3.1 The r-process

Very neutron rich environments at high temperature permit neutron captures, much faster than competing β -decay, to occur up to the neutron drip-line and are sites of the rapid neutron capture (r-process) which is thought to be responsible for creating about half of all nuclei with $A \geq 70$. Observational data on elemental and isotopic solar abundances of nuclei (see [182] and references therein) serve as a stringent test of the r-process models concerning both the characteristics of the stellar environment and the nuclear physics input. Details of the r-process models are beyond the scope of this review and are given elsewhere [182, 119, 181]. Here we only point out that the current understanding is that in the high temperature and high density environment, leading to the r-process, chemical equilibrium between neutron capture and the reverse photodisintegration develops within each isotopic chain (for a given Z) and the flow along the r-process path is governed by β -decay from one isotopic chain to another. It follows that in equilibrium conditions the r-process path is uniquely determined by the neutron number density n_n , temperature T and neutron separation energy $S_n(n_n, T)$ (Q-value) [119] and cross sections of individual capture processes are not important. The process is slowed down when it reaches nuclei with magic number of neutrons ($N=50, 82$ and 126) and β -decay becomes comparable or faster than neutron capture. Then a series of β -decays and (n, γ) processes takes place each changing Z and A by one [183]. The nuclei in this series are called the waiting point nuclei. As these nuclei approach stability, β -decay lifetimes get longer and the process gradually breaks off and proceeds with more favored neutron capture (competing at some cases with β -delayed neutron emission) towards the next neutron closed shell.

The nuclear masses (in particular neutron separation energies S_n) and gross β -decay properties (half-lives and β -delayed neutron emission probabilities) along the contour line of constant S_n are the key nuclear inputs into r-process modeling. Another important piece of information comes from investigations of shell structure far from stability, in particular the strength of shell gaps which affect r-process abundances in the vicinity of magic numbers. At the endpoint of the r-process path when fissionable nuclei are reached, β -delayed fission becomes important. The fission fragments may alter heavy element abundances and also increase general r-process abundances [181]. The important nuclear physics input to modeling of this final phase of the r-process includes fission probabilities of nuclei at highly excited states and precise calculation of fission barriers.

Calculation of nuclear masses has been of major interest for decades. The major contribution to this

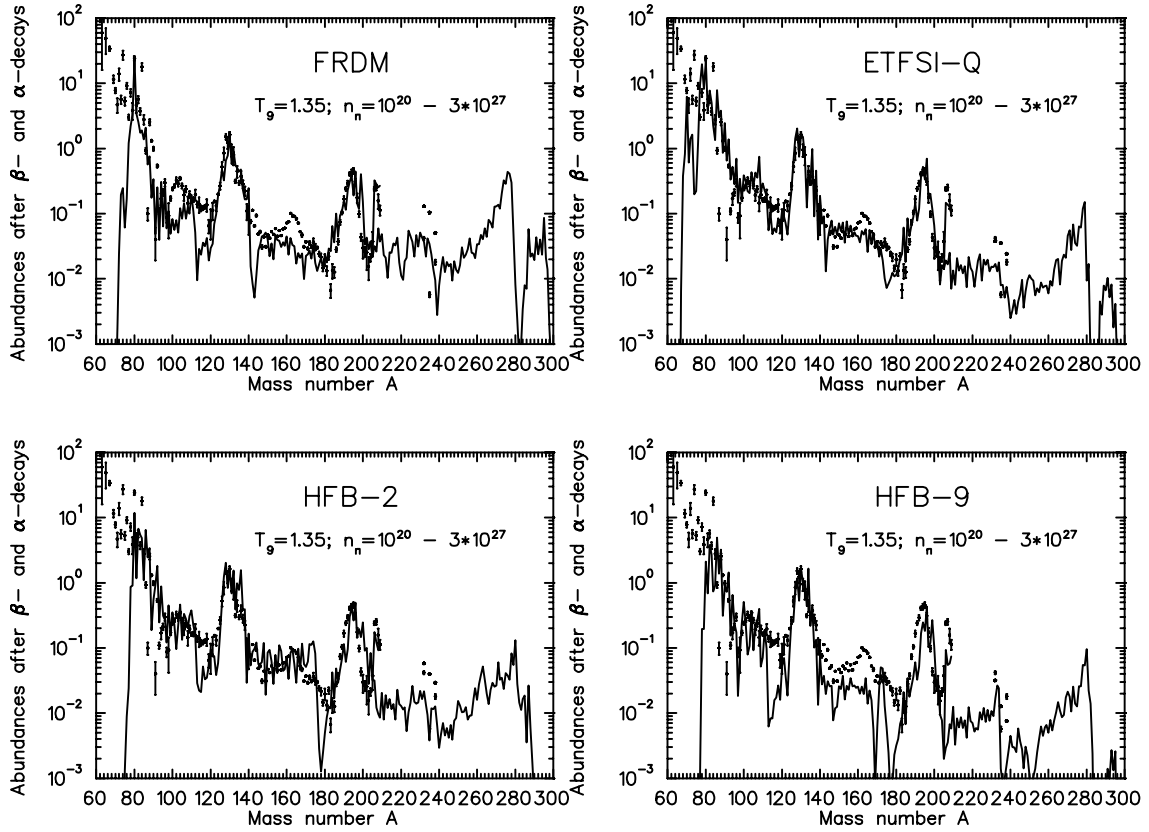


Figure 13: Observational solar abundance distribution $N_{r,\odot}$ (dots) in comparison with calculation [192] $N_{r,calc}$ (full line), using four different mass models, FRDM [14], ETFSI-Q [185], HFB-2 [187] and HFB-9 [189]. Except for the S_n energies, all other nuclear physics and astrophysics parameters we kept the same in the calculations.

field has been achieved in the Finite Range Droplet Model (FRDM) of Moller et al. [14]. An extensive attempt to employ microscopic models using the Skyrme interaction in the Extended Thomas-Fermi Strutinsky Integral [184, 185], HF+BCS [186] and HFB [187, 188, 189] mean-field models in precise ground state mass calculations has been made in recent years. A number of new Skyrme parameterizations have been developed for this purpose (SkSC, MSk and BSk families) by optimizing fitting to all known mass-data only, not taking into account any other experimental constraints. Examination [190] of the results that these microscopic calculations did not improve on the best r.m.s error of 0.633 MeV achieved by FRDM in fitting the latest table of experimental masses [191] and did not show an improved predictive power, especially in the region of neutron-heavy nuclei. We display results of calculations of the r-abundance distribution $N_{r,calc}$ using two representative HFB models, the FRDM model and ETFSI-Q model (with SkSC4 Skyrme parameterization) in Fig. 13 in comparison with observational data $N_{r,\odot}$. It is seen that in particular the HFB-9 predictions give serious differences from observational data, especially in the $A=120$ and $A=140-180$ regions. It was concluded [190] that is very unlikely that the present HF mass models will ever yield atomic masses with the precision required by the r-process and related applications, unless a very different approach is explored. It is important to realize that not only atomic masses but derived observables, dependent on mass *differences*, like one- and two-nucleon separation energies and Q_β values are also required. Very careful exploration of the real sensitivity of the mean field Hamiltonian to particular aspects of available experimental information on nuclei is needed. Then the most sensitive data should be fitted together to find truly optimized Skyrme parameter sets. Furthermore, it is clearly desirable that the correlations between parameters of the Skyrme functional, individually or in groups, are systematical examined and their role unambiguously understood. This

may provide a very powerful and decisive constraint in the search for meaningful Skyrme functionals.

Gross β -decay properties have been treated in a variety of models (see, e.g. [193]) that range from phenomenological to large scale microscopic calculations. At this point all models have some deficiency and it is not yet possible to calculate the whole r-process. The limitations are mainly in restriction to spherical shapes, Gamow-Teller (GT)-transitions only, or too small shell model spaces. One of the key issues is as-correct-as-possible treatment of nucleon-nucleon correlations in a model. The only fully self-consistent HFB+QRPA calculation of β decay rates of the r-process waiting-point nuclei utilized the Skyrme parameterization SkO' [194]. An important extension of the Skyrme-HFB model employed here was the incorporation of time-odd terms in the Hamiltonian, needed for the correct treatment of the GT excitation. These terms contribute to the energy of polarized states, i.e. those with non-zero angular momentum, including the 1^+ states populated in the β -decay. They are usually neglected in Skyrme-HF calculations which are then strictly speaking applicable only to even-even nuclei. The consequence of consideration of the T-odd terms is the introduction of additional variable parameters and their relationship with the parameters of the T-even part of the Hamiltonian has to be established [195]. The results of this calculation include a study of the GT-strength distribution over the spectrum of excited states and the effect of the strength of the pn particle-particle interaction. It was shown that the HFB-QRPA model [194] in all but very heavy nuclei calculates half-lives that are shorter than predictions of the FRDM+QRPA [196] and EFTSI+QRPA [197] in some cases in improved agreement with experiment. Unfortunately, a full study of the impact of the calculation on the r-process could not be completed because not all waiting point nuclei were calculated and the no deformation effects were included in the model. It would be desirable to follow up this issue and establish the origin of the difference in predictions of β -decay half-lives.

The presence and strength of neutron shell closures affects the rate of the r-process flow through the waiting point nuclei. This information comes from mean field or other mass model calculations and, to large extent, from experiment (see e.g. [193] and references therein). It has been shown [198] that, for example, abundance deficiencies around $A=120$ and $A=140$, calculated using mass predictions from global macroscopic-microscopic models, indicated too strong $N=82$ shell closure. When the masses were calculated locally in the vicinity of the shell closure using an HFB model with SkP force which predicted quenching of the $N=82$ gap, the agreement between calculated and observed solar r-process abundances seriously improved. At the present time it is clear that existence of yet unknown changes in the shell structure at the neutron drip-line region may have a profound impact on the flow of the r-process.

3.3.2 The rp-process

Hot environments with a large surplus of hydrogen (protons) permit proton capture on seed nuclei close to the stability line up to proton drip-line - in a process called the rapid proton capture (rp-process) [199]. It originates in explosive hydrogen burning at temperatures high enough that a break-out of the hot CNO cycle is possible. It proceeds by a series of proton capture reactions and β^+ -decays and at sufficiently high density and temperature can get well beyond $A=64$ and $Z=32$ [200] until the rp-process reaches the proton drip line. The rp-process is thought to be the dominant source of type I X-ray bursts and responsible for the nuclear composition of the crust of an accreting neutron star [201]. The key nuclear input includes proton separation energies S_p to determine proton capture and reverse photodisintegration, alpha separation energies S_α for treatment of back-processing via α emission or (γ, α) disintegration and $Q_{\beta^+} = Q_{EC} - 2m_e c^2$ for calculation of the rate of weak processes along the rp-process path.

As for the r-process, the lack of experimental data in important regions of the rp-process path forces us to turn to theoretical models. The mass models play, as usual, a key role. Weak interaction rates are usually known experimentally for nuclei with $Z \leq 34$. For β -decay of isotopes heavier than $A = 20$

the decay from thermally populated excited states has to be taken into account and the temperature dependence of the decay rate has to be calculated. The standard approach is to calculate these rates within QRPA [196] and, wherever possible, in the shell model.

An interesting attempt to calculate properties of nuclei along the rp-process path close to the proton drip-line has been reported by Brown et al., [202] who calculated one-proton and two-proton separation energies in the spherical Skyrme HF model. They calculated Coulomb displacement energies of mirror nuclei and utilized known masses of the neutron rich partner of a mirror pair. The newly developed SkX Skyrme parameterization with a especially added charge symmetry breaking (CSB) term was used [203]. The results in the region of $A = 41-75$, given with the error dependent on the experimental error of the neutron-rich nucleus and assumed 100 keV theoretical error, were extensively tested in rp-process simulation and models for the x-ray burst. It has been clearly shown that the x-ray burst tails are sensitive to nuclear masses at and beyond the $N = Z$ line between Ni and Sr. The new calculation leads to a tighter constraint on proton capture Q values as compared to extrapolation of experimental masses [191]. The authors connect this success with the special parameterization of the SkX_{CSB} force to account for charge-symmetry breaking. The results are indeed better in comparison with the original SkX force. However the question remains how unique is this extension of the SkX force and, whether some other parameterizations than SkX would behave similarly if the CSB term was added to them.

3.4 Beyond the mean-field: Collective correlations

3.4.1 Large amplitude collective motion

As outlined in Section 2.1.1, correlations cover anything beyond mean field and embrace very different mechanisms. Short-range and long-range correlations are assumed to be incorporated into the effective energy-density functional. Collective correlations, however, cannot be accounted for in a simple energy-density functional and need to be considered as explicit correlations in addition to the mean field calculations.

The effective energy functionals can still be used for that task since low-energy (and thus large amplitude) collective motion can be derived as the adiabatic limit of time-dependent mean fields. This applies exactly to center of mass motion which perfectly decouples from internal excitations but to a good approximation also. This applies to rotation whose ground state has zero energy and where the excitation energies are by far the smallest in the nuclear spectrum. The approach has been usually applied to low-energy modes associated with surface vibrations of quadrupole type, sometimes also of octupole nature. The zero-energy modes (center of mass in Section 2.2.3, rotation in Section 3.2.4) are related to symmetry breaking through the mean field and restoration through correlations. In the same spirit, this includes also particle-number projection in connection with BCS states although the associated collective ‘deformation’ corresponds to a motion through phase angles and does not have any geometrical interpretation.

Somewhat in analogy to the Born-Oppenheimer picture in molecular physics, the adiabatic motion is thought to evolve along a collective path which is set of mean-field states $\{|\Phi_q\rangle\}$ where q labels the collective deformation (e.g., rotation angle or quadrupole momentum). In the ideal case, the path is generated by adiabatic TDHF (ATDHF) [204, 205, 39]. In practice, one approximates that by a constrained Hartree-Fock (CHF) calculation in which a wanted deformation $q = \langle \Phi_q | \hat{Q} | \Phi_q \rangle$ is achieved by adding a constraining operator to the mean field Hamiltonian, i.e. $\hat{h} \longrightarrow \hat{h} - \lambda \hat{Q}$ where λ is the Lagrange multiplier. The dynamical properties are explored by self-consistent cranking taken over from the ATDHF scheme. The collective spectrum (correlated ground state and excitations) is usually described within generator-coordinate method (GCM) as a coherent superposition of these deformed mean-field states i.e.

$$|\Psi_n\rangle = \int dq |\Phi_q\rangle f_n(q) \quad . \quad (22)$$

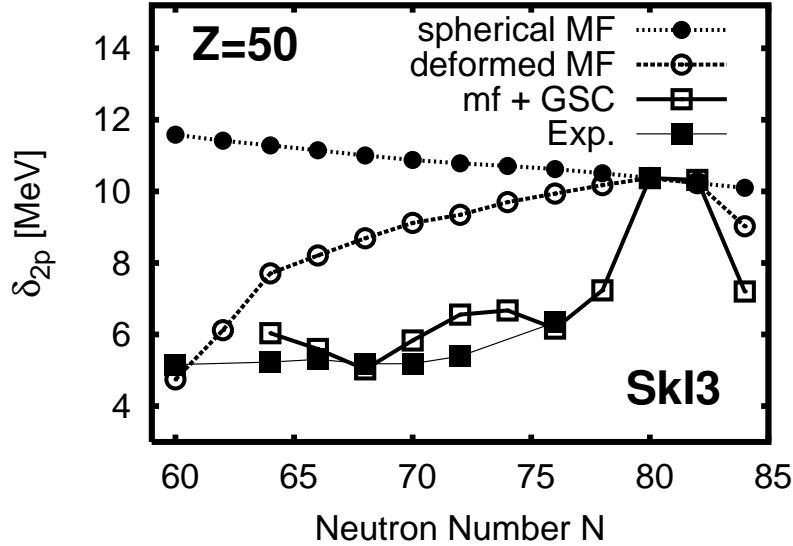


Figure 14: The two-proton shell gap δ_{2p} calculated for the interaction SkI3 at various levels of the model: spherical mean field, deformed mean field, and with collective ground state correlations from quadrupole vibration and rotation. The experimental data are taken from [209].

The equations for the superposition functions $f_n(q)$ are obtained by variation. The machinery of the GCM and the various approximations invoked in actual calculations are a large topic, far beyond the scope of this review. We refer to summaries in [39, 206, 38, 22] and mention only the two basically different solution schemes: some groups go for a direct numerical attack on a finite grid of $|\Phi_q\rangle$, other groups deduce a collective Hamiltonian in terms of the q and solve that.

The deformation coordinates q embrace all the typical low energy modes. The three nuclear center of mass coordinates are included among these and their approximate treatment leads to the c.m. correction as explicitly included in the energy functional and as discussed in Section 2.2.3. The next important considerations are the five coordinates for vibration-rotation, either as the five quadrupole momenta or recoupled to total quadrupole coordinate β , triaxiality γ , and three Euler angles [207]). The GCM, or collective Hamiltonian, in these coordinates yields the low-energy quadrupole spectra and consistent with it also the correlated ground state associated with the lowest solution f_0 . An example of spectra will be discussed in Section 3.4.3 and of ground-state correlations in 3.4.2. It is to be noted that octupole modes can also become very soft and accessible to the adiabatic picture, for a typical application see e.g. [208].

What is meant by ‘beyond mean field’ clarifies when we consider in GCM ansatz (22) expressed sums of mean field states. The superposition is necessary for a fully quantum mechanical treatment of the system. TDHF as such can also describe large amplitude motion and it does it in terms of a trajectory $|\Phi(t)\rangle$ which remains at every instant a mean-field state and never goes ‘beyond’. One can say that TDHF represents the classical limit of many-body dynamics. The classical trajectory belongs to the mean-field approach and GCM serves to ‘re-quantize’ the description. There are regimes of collective motion where a semi-classical description suffices, such as fission which had been discussed in Section 3.1.5 and heavy-ion reaction which were sketched in Section 3.2.3. A particularly subtle case are the small amplitude vibrations discussed in Section 3.2.1 and 3.2.2. TDHF allows computation of the frequency spectrum of classical vibrations. The re-quantization is performed unconsciously through the equivalence of classical and quantum-mechanical picture for the harmonic oscillator. That simple equivalence fails for non-harmonic motion which is usually encountered in soft modes and this, in turn, requires the elaborate GCM techniques.

3.4.2 Correlations from soft modes

The impact of collective correlations on bulk properties of semi-magic nuclei is generally very small. That is why these nuclei are preferable used in the fitting of forces. The situation may change, however, when considering the much more sensitive isotopic or isotonic differences. The crucial influence of collective correlations on isotopic differences of radii, the isotopic shifts [210], has been long recognized in many places, e.g. [211, 212]. The effect on energy differences, though less in focus up to now, is not less important. As an example, Figure 14 shows the second energy difference, the two-proton shell gap,

$$\delta_{2p} = E(Z+2, N) - 2E(Z, N) + E(Z-2, N), \quad (23)$$

in Sn isotopes. The results from all spherical calculations agree very nicely with twice the spectral gap at the magic $Z = 50$ shell closure. This confirms the idea behind using the shell gap as a measure of the spectral gap. However, the spherical results are far from the measured values, in both size and trend. As a next step, we allow for (axially) deformed ground states. This lowers the δ_{2p} gap for the isotopes with low neutron number because the neighboring isotones (Cd and Te) gain binding energy through deformation while semi-magic Sn remains spherical. The deformation effect is still insufficient to match experimental gaps. We are obviously in a transitional regime between spherical and deformed shapes where we expect large shape fluctuations and consequently substantial collective correlations. And indeed, the δ_{2p} gaps obtained using correlated ground states match experimental values very nicely. (These calculations were done within the Gaussian Overlap Approximation to GCM, for details see [213].) This example shows that correlation can have a dramatic effect on isotopic (or isotonic) differences. It need not always be that dramatic – a similar study in the Pb isotopes has shown that there the deformation effect suffices to reproduce the data [214]. Nonetheless, a careful check is advisable in any case.

3.4.3 Low energy quadrupole excited states

There is a widespread literature on the computation of low-energy spectra on the basis of SHF or the Gogny model using various variants of the GCM. These deal mainly with low-lying quadrupole excited states, see e.g. [215, 216, 217], sometimes also octupole excitations, see e.g. [208, 218]. Well adjusted modern Skyrme parameterizations provide usually a pertinent description of these soft modes. Their typical performance is demonstrated in Figure 15 taking Sn isotopes as example. Doubly magic ^{132}Sn is clearly distinguished by its large excitation energy. Pairing is inactive in a doubly-close-shell nucleus and the energy spectrum is closely related to shell structure, in particular the shell gap in the single-nucleon spectra. The low lying quadrupole mode in all other isotopes is dominated by the pairing gap. It is no surprise then that many different SHF parameterizations yield very similar results provided that the pairing strength has been calibrated properly for each case. The crucial influence of pairing is demonstrated for SkI3 by reduction of the pairing strength by to 75% of the standard strength. The particularly strong effect seen around neutron number $N = 68$ is related to a semi-shell closure at a point at which the BCS scheme runs into a critical regime close to breakdown.

As discussed above, the results for the excitation energy are generally very satisfying. The transition moments, however, are not yet so well described as is true of most models. This is because the moments are much more sensitive to the collective mass which, in turn, is extremely sensitive to the choice of the collective path [219]. We suspect that moment calculations could be much improved by using the full ATDHF instead of approximating it through CHF. In spite of this unresolved detail, we want to emphasize that self-consistent mean-field models with well adjusted bulk and pairing properties yield directly a pertinent description of large amplitude collective dynamics without the need of additional re-tuning.

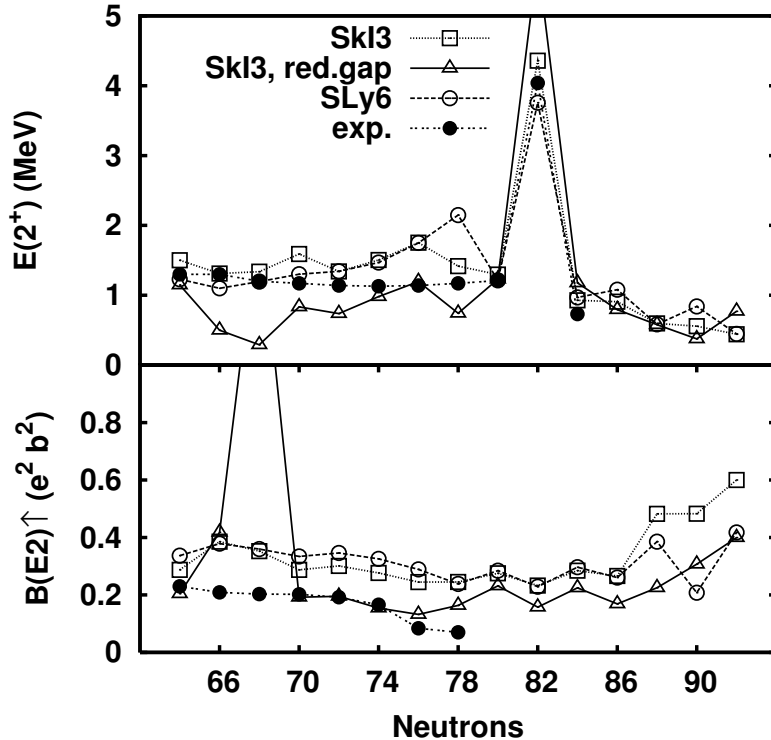


Figure 15: The energy (upper panel) and $B(E2)$ transition moments (lower panel) of the lowest quadrupole state (2^+) in Sn isotopes computed with two different forces as indicated and compares with experimental data. For the force SkI3, we also consider the case of a 75% reduced pairing strength.

4 Infinite matter and astrophysical applications

The concept of infinite nuclear matter has been introduced to nuclear physics as an extrapolation of the almost homogenous conditions in the center of heavy nuclei. In this fully homogeneous matter the difference between neutrons and protons is neglected and no single particle effects are considered. These conditions lead to constant density and the absence of Coulomb energy, pairing and surface effects. These features make it an attractive medium for testing and comparing models of bulk nuclear properties. Infinite nuclear matter is, however, not an observable system and the quantities characterizing its properties are of empirical nature (see Section 4.2.1). There are two limiting states of infinite nuclear matter, symmetric nuclear matter (SNM) with equal number of protons and neutrons and pure neutron matter (PNM) with no protons present. These two states have fundamentally different properties. The energy per particle in SNM reaches a negative minimum value (i.e. it saturates) at a *saturation density* n_0 ($=0.16 \text{ fm}^{-3}$), corresponding to the lowest bound state of SNM (the ground state). On the contrary, the energy per particle in PNM is predicted to be always positive, i.e. PNM as such does not exist in a bound state and represents the highest excited state on nuclear matter. These properties of SNM and PNM place powerful constraints on the parameters of the Skyrme interaction, as will be discussed later.

Asymmetric nuclear matter that lies between the two extremes with the proton/neutron ratio between zero and one has become a popular medium for modeling large fractions of stellar matter in compact objects, in particular in cold neutron stars. Note that the term ‘compact object’ in astrophysics refers to an object whose gravity produces a deep potential well. It is most commonly used to describe neutron stars and black holes but is sometimes also used to refer to white dwarfs. Note that the defining feature is the depth of the potential well and not the strength of gravitational forces (which can be quite modest in the case of high-mass black holes). The deep potential well means that light coming from the surface to an outside observer is significantly redshifted and light rays passing close to the object are significantly bent. The equation of state of nuclear matter is constructed from the calculated density and composition dependence of energy per particle, as discussed in Section 4.2. There

is no direct experimental information available on the behavior of the energy per particle in nuclear matter. Theoretically it exhibits strong dependence on the properties of the interaction between particles present in the matter. In the investigation of this dependence for different parameterizations of the Skyrme interaction, we use as a benchmark the ab-initio calculation with the realistic A18+ δv +UIX* (APR) potential [220]. The APR model is based on the Argonne A18 two-body interaction and includes three-body effects through the Urbana UIX* potential and boost corrections to the two-nucleon interaction which gives leading relativistic effects of order $(v/c)^2$. This interaction is considered as one of the most modern realistic potential used for description of nuclear matter at present.

4.1 Relevance of nuclear properties to physics of compact objects

In order to construct compact star models, it is necessary to have an equation of state (EoS) linking pressure with total energy-density and, to obtain this, expressions must be supplied for the interaction potentials or energy functionals of the particles concerned [221, 222, 223]. The basic ingredient of the EoS, the effective nucleon-nucleon interaction, is not very well known and assumptions need to be made about its nature and form, particularly as regards its behavior as a function of density. In this section we concentrate on the role the non-relativistic phenomenological Skyrme interaction plays in this context, and its limitations. Especially relevant for our discussion are cold, non-rotational neutron stars as naturally occurring compact objects. At around nuclear matter density, neutron star matter can be well-represented as a homogeneous mixture of neutrons, protons, electrons and muons ($n+p+e+\mu$ matter) representing beta-equilibrium matter (BEM). These densities turn out to be crucial for determining the properties of neutron star models with masses near to the widely-used ‘canonical’ value of $1.4 M_{\odot}$. However, models of non-equilibrium systems like core-collapse supernovae, both at sub- and super- nuclear densities, also use EoS based on the Skyrme interaction [224].

We focus here on to what extent SHF fulfills the important requirement that it describes not only finite nuclei but is also valid in infinite nuclear matter. Almost 90 Skyrme functionals were recently tested in nuclear matter and cold ($T=0$) non-rotational neutron star models. Details can be found in [28]. Here we state only the main conclusion drawn in [28] that Skyrme interactions, giving broadly similar agreement with the experimental observables of nuclear ground states as well as with properties of SNM at saturation density, predict widely varying behavior for the observables of both symmetric and asymmetric nuclear matter as a function of particle number density. The underlying property, decisive for the validity of a Skyrme interaction in nuclear matter models, is the density dependence of the symmetry energy. Here we will demonstrate this result and its implications for models of neutron stars on the same set of the Skyrme parameterizations used in the previous sections, SkM*, SLy6, SkP, SKI3, SkI4 and BSk1 as examples.

The requirement that SHF remains applicable in various astrophysical scenarios, utilizing the growing amount and precision of observational data, in particular on neutron stars, places important constraints on the optimal parameter sets. These will be discussed throughout the coming sections.

4.2 Relation to SHF and the Equation of State

The key property of a system for use in EoS models is the total energy per particle $\mathcal{E} = E/A$. As discussed above (see Section 4), nuclear matter is a medium of constant density. This simplifies significantly the total energy defined for finite nuclei by equation (11) in Section 2.2.2. All terms depending on $\Delta\rho$, \mathbf{j} , $\boldsymbol{\sigma}$, and \mathbf{J} vanish. The assumption of absence of the Coulomb force in nuclear matter is in line with the condition for existence of stars, bound together by the gravitational force, many orders or magnitude weaker than the electromagnetic force. The c.m. correction approaches zero in infinite

matter and pairing is neglected as well. Thus the Skyrme energy functional in nuclear matter becomes

$$E = \int d^3 \{n\mathcal{E}_{\text{kin}} + n\mathcal{E}_{\text{Skyrme}}\}, \quad (24a)$$

$$n\mathcal{E}_{\text{Skyrme}} = \frac{B_0 + B_3 n^\alpha}{2} n^2 - \frac{B'_0 + B'_3 n^\alpha}{2} \tilde{n}^2 + B_1 n\tau - B'_1 \tilde{n}\tilde{\tau} \quad (24b)$$

where \mathcal{E}_{kin} is taken in the same form as (11). The terms $\propto B_0, B'_0$ correspond to a zero-range attractive two-body force, terms $\propto B_3, B'_3$ to a density-dependent repulsive force, and those $\propto B_1, B'_1$ are related to the nucleon effective mass. The above expression for $\mathcal{E}_{\text{Skyrme}}$ is a function of 7 variable parameters B_i, B'_i and α . It is sometimes convenient to express them in terms of 9 alternative Skyrme parameters t_i, x_i and α [225] using relations (12).

The relation between finite nuclei and infinite matter is established by considering a finite volume V of homogenous matter containing N neutrons and Z protons, forming $A = N + Z$ nucleons. For matter with $N \neq Z$ the asymmetry parameter is defined as the ratio

$$I = \frac{N - Z}{A} = \frac{n_n - n_p}{n} = \frac{\tilde{n}}{n} \quad (25)$$

Then the proton and neutron number densities are given in terms of I and n as

$$n_p = \frac{Z}{V} = \frac{n}{2}(1 - I) \quad , \quad n_n = \frac{N}{V} = \frac{n}{2}(1 + I) \quad , \quad n = \frac{A}{V} = n_n + n_p \quad (26)$$

Using the expression for the energy E (24a) we define the total energy density of nuclear matter

$$\epsilon(n, I) = n(\mathcal{E} + mc^2) \quad (27)$$

where $\mathcal{E} = E/A$ is the binding energy per particle while $n\mathcal{E} = E/V$ is the energy density, i.e. the energy per volume.

Nuclear matter obeys the standard thermodynamical relation between pressure P and Helmholtz free energy $F = E - TS$ where E is the internal energy (24a) and S is the entropy, namely

$$P = \left. \frac{\partial F}{\partial V} \right|_{T,S} \quad (28)$$

This can be rewritten in terms of n and I in the form

$$P = n^2 \left. \frac{\partial \mathcal{F}(n, I)}{\partial n} \right|_{T,I} \quad , \quad \mathcal{F} = \frac{F}{N} \quad (29)$$

where \mathcal{F} is the free energy per particle. For systems at zero temperature ($T = 0$) the equation (29) reduces to

$$P = n^2 \left. \frac{\partial \mathcal{E}(n, I)}{\partial n} \right|_I \quad (30)$$

The pressure is fully determined by the total energy per particle $\mathcal{E}(n, I)$ and its dependence on the particle number density n and composition I . This relation is often called the equation of state for convenience - it can be very easily converted to the more customary form relating pressure, temperature and volume as demonstrated above. We illustrate, in Figure 16, the energy per particle \mathcal{E} as a function of total nucleon number density n for six different parameterizations of the Skyrme interaction discussed above in Section 3. The calculation has been performed at zero temperature for the two extreme phases of nuclear matter, SNM at $I = 0$ and PNM at $I = 1$. Examination of Figure 16 shows that the density dependence of \mathcal{E} for SNM is calculated to be rather similar for all the selected parameterizations and compares reasonably well with values yielded by the APR model. However this general agreement does not carry over to the predictions for PNM for which the density dependence of \mathcal{E} varies significantly for different SHF parameterizations at densities higher than about 0.2 fm^{-3} and agrees with the APR result only for SLy6.

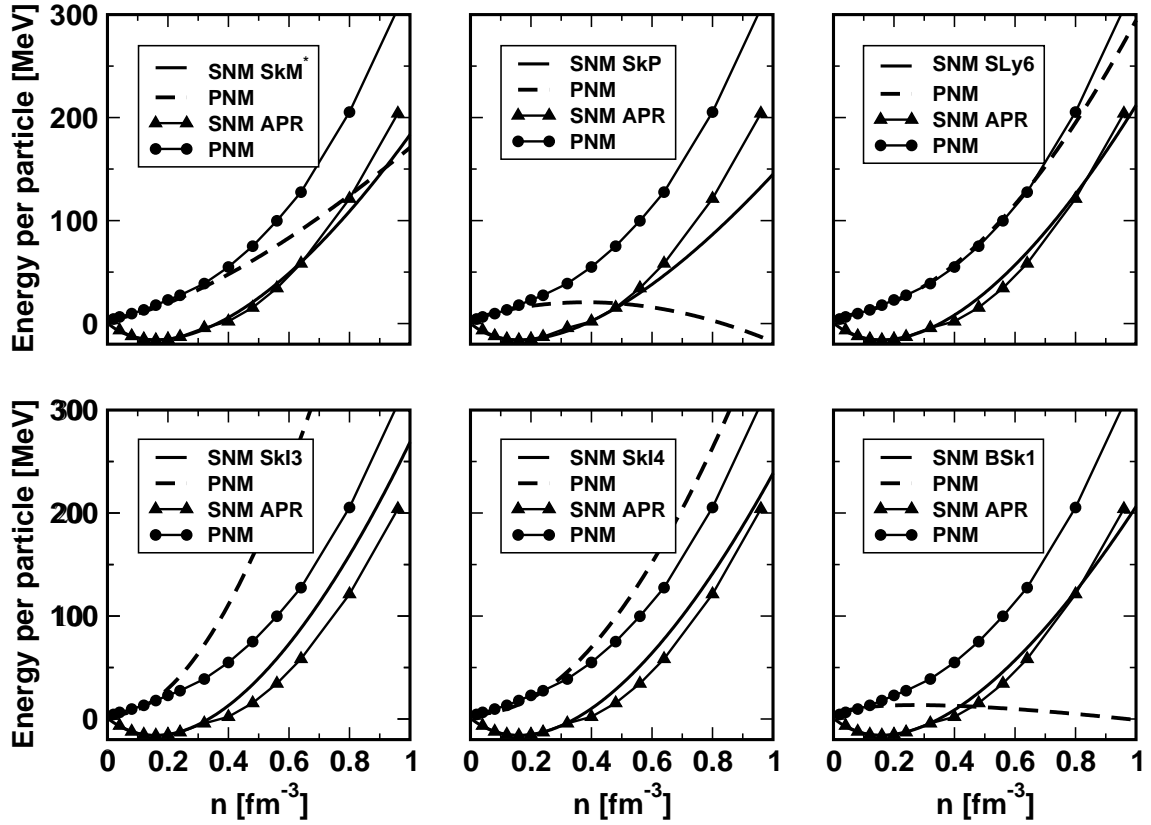


Figure 16: The energy per particle for SNM and PNM is plotted as a function of baryon number density n for SkM*, SkP, SLy6, SkI3, SkI4 and BSk1 Skyrme parameterizations. For comparison, also shown are equivalent curves for SNM (triangles) and PNM (circles) calculated using the APR potential [220]. For more explanations, see text.

4.2.1 Key properties of nuclear matter

Although infinite nuclear matter is not directly observable, the equilibrium parameters of SNM and some properties of asymmetric matter provide a physically plausible and intuitive way to characterize the bulk properties of a model. We consider in the following paragraphs the saturation density of nuclear matter n_0 , the binding energy of SNM \mathcal{E} at this density, the incompressibility modulus K , the symmetry energy a_{sym} and the isoscalar and isovector effective nucleon masses. Currently accepted values are then compared with predictions of the selected Skyrme parameterizations and with selected interaction used in RMF models discussed in Section 2

The energy functional provides the binding as function of the isoscalar and isovector densities, i.e. $\mathcal{E}(n, \tilde{n})$. In SNM, the equilibrium energy and density are defined by the condition

$$\frac{\partial \mathcal{E}}{\partial n} = 0 \quad (31)$$

(the other condition $\partial \mathcal{E} / \partial \tilde{n} = 0$ is automatically satisfied for $\tilde{n} = n_p - n_n = 0$). The best estimate of the density n_0 of symmetric nuclear matter at saturation is based on the comparison of experimental and calculated charge distribution in heavy nuclei. The most precise value $n_0 = 0.16 \pm 0.005 \text{ fm}^{-3}$ is given in [225]. A more conservative value of $0.17 \pm 0.02 \text{ fm}^{-3}$ is given in Ref.[226] where the error bar includes uncertainties in the neutron density distribution and a correction for possible density inhomogeneity in nuclear interior. The value of $0.16 \pm 0.02 \text{ fm}^{-3}$ quoted in [221] is of the same precision as that in Ref. [226].

The accepted value of $\mathcal{E}_0 = \mathcal{E}(n_0, I = 0)$ at saturation (i.e. the minimum value) is taken to be equal to the coefficient of the volume term a_v in the liquid-drop model, obtained by fitting the binding energies of a large number of nuclei. This procedure gives $\mathcal{E}_0 = -(16.0 \pm 0.2) \text{ MeV}$ [225].

The *incompressibility modulus* K is related to the curvature of E/A as [225]

$$K(n) = 9n^2 \frac{\partial^2 \mathcal{E}}{\partial n^2} + 18 \frac{P(n)}{n} \quad (32)$$

The value of $K_\infty = K(n_0)$ at saturation ($P = 0$), represents an important constraint on models of nuclear matter. However K_∞ is a derived quantity and its ‘best’ value is model dependent. Nix and Moller estimate $K_\infty \simeq 240 \text{ MeV}$ [227], while Hartree-Fock + RPA calculations of the giant isoscalar monopole resonance (the breathing mode) [228] imply $K_\infty = (210 \pm 20) \text{ MeV}$ both with the use of Skyrme interactions [229] and with the Gogny potential [230]. The generalized Skyrme interactions [231], fitted both to finite nuclei and the breathing mode energies, give the best results for $K_\infty = (215 \pm 15) \text{ MeV}$. In the non-relativistic approximation, the *speed of ordinary sound* in the nuclear medium is related to the incompressibility modulus K by [221]

$$\frac{v_s}{c} = \frac{dP(n)}{d\epsilon} = \sqrt{\frac{K(n)}{9(mc^2 + \mathcal{E} + \frac{P(n)}{n})}} \quad (33)$$

It is desirable to check the density dependence of the speed of sound as it may exceed the velocity of light at higher densities in non-relativistic models [221] and this unrealistic feature must be avoided.

One of the key properties of nuclear matter is the *symmetry energy*, particularly important in the modeling of nuclear matter and finite nuclei because it depends on the isospin part of the interaction and is relevant for correctly describing nuclei with high values of isospin far from stability. It reads

$$\mathcal{S}(n) = \mathcal{E}(n, I = 0) - \mathcal{E}(n, I = 1) \quad (34)$$

This quantity is related to the *asymmetry coefficient* a_{sym} in the semiempirical mass formula under two assumptions, (i) $\mathcal{E}(n, I = 0)$ is the minimum energy of the matter at given density n and thus in the

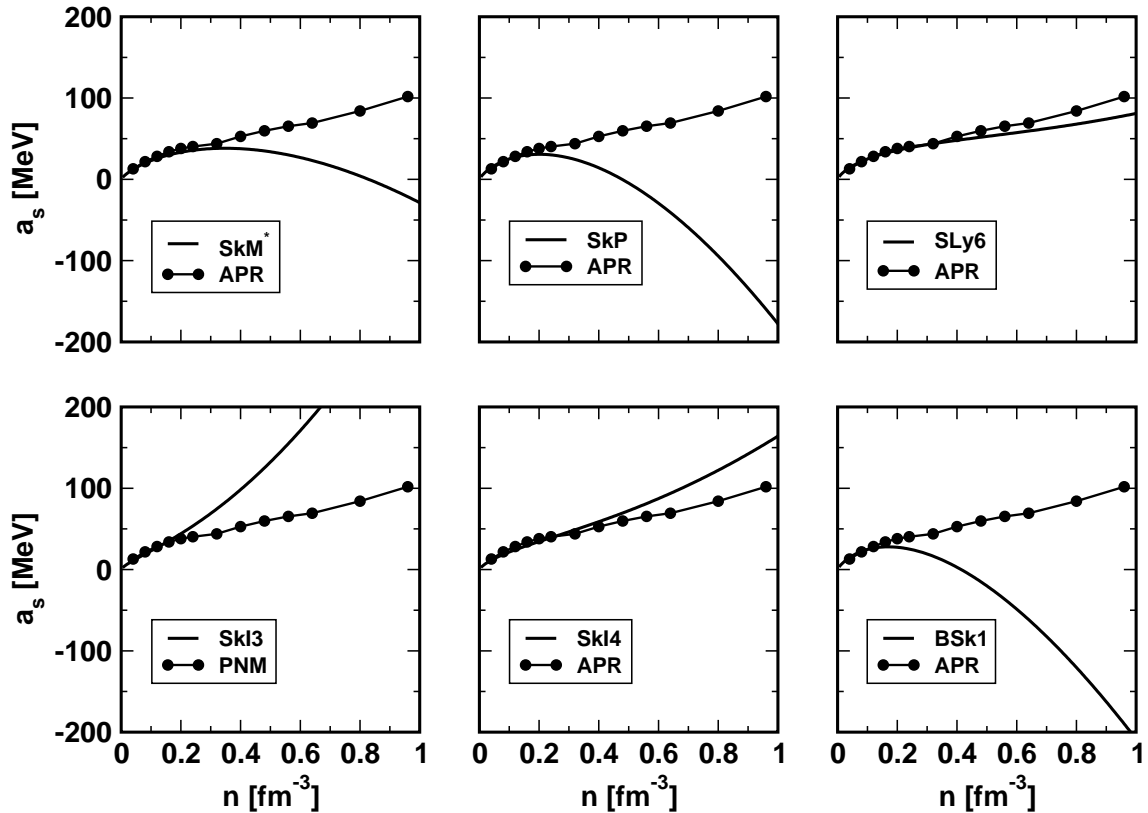


Figure 17: The asymmetry coefficient a_{sym} as a function of particle number density n for the six Skyrme parameterizations compared with the APR [220].

expansion of $\mathcal{E}(n, I)$ about this value with respect to I (or equivalently \tilde{n}) the leading non-zero term is the second derivative term and (ii) all the other derivatives in the expansion are negligible. Then [96]

$$a_{\text{sym}} = \frac{1}{2} \left. \frac{\partial^2 \mathcal{E}}{\partial I^2} \right|_{I=0} = \frac{n^2}{2} \left. \frac{\partial^2 \mathcal{E}}{\partial \tilde{n}^2} \right|_{\tilde{n}=0} . \quad (35)$$

In practice, $\mathcal{E}(n, I)$ contains always a small component $\propto I^4$ [96] and thus expression (35) should be treated as approximation. A value $a_{\text{sym}} = 32.5 \pm 0.5$ MeV is found by fitting a large set of experimental data in the Finite-Range-Droplet-Model (FRDM) [232]. The extrapolation of the various fits for the non-relativistic models (SHF and Gogny) yield typical values of a_{sym} in the region of 27–38 MeV, see [221, 186, 22, 96] and Figure 18. The various RMF parameterization yield values in the 35–42 MeV range, see [233, 22, 96] and Figure 18.

The density variation of the asymmetry energy coefficient a_{sym} , defined by Eqs. (34) and illustrated in Figure 17 is determined by the density dependence of \mathcal{E} in SNM and PNM. We see two distinctly different patterns for the various Skyrme parameterizations; a_{sym} is either growing or decreasing with increasing particle number density. A more detailed analysis even distinguishes between the rate of decrease of a_{sym} with increasing n [28]. The transition to a negative value of a_{sym} indicates that PNM becomes the ground state (which is unphysical [234]), the pressure becomes negative and the matter collapses. This is the case of the SkP and BSk1 parameterizations as shown in Figure 17. Another (early) indicator of a possible collapse of nuclear matter at high densities is too low a value for the derivative of the symmetry energy with respect to particle number density at n_0 (see Table 2). As we will show in the next section that such parameterizations cannot produce neutron-star models with masses as high as the ‘canonical’ $1.4 M_{\odot}$ and so they should be excluded from consideration for astrophysical purposes. Of our sample group this applies to BSk1 and SkP, but there are more examples of Skyrme

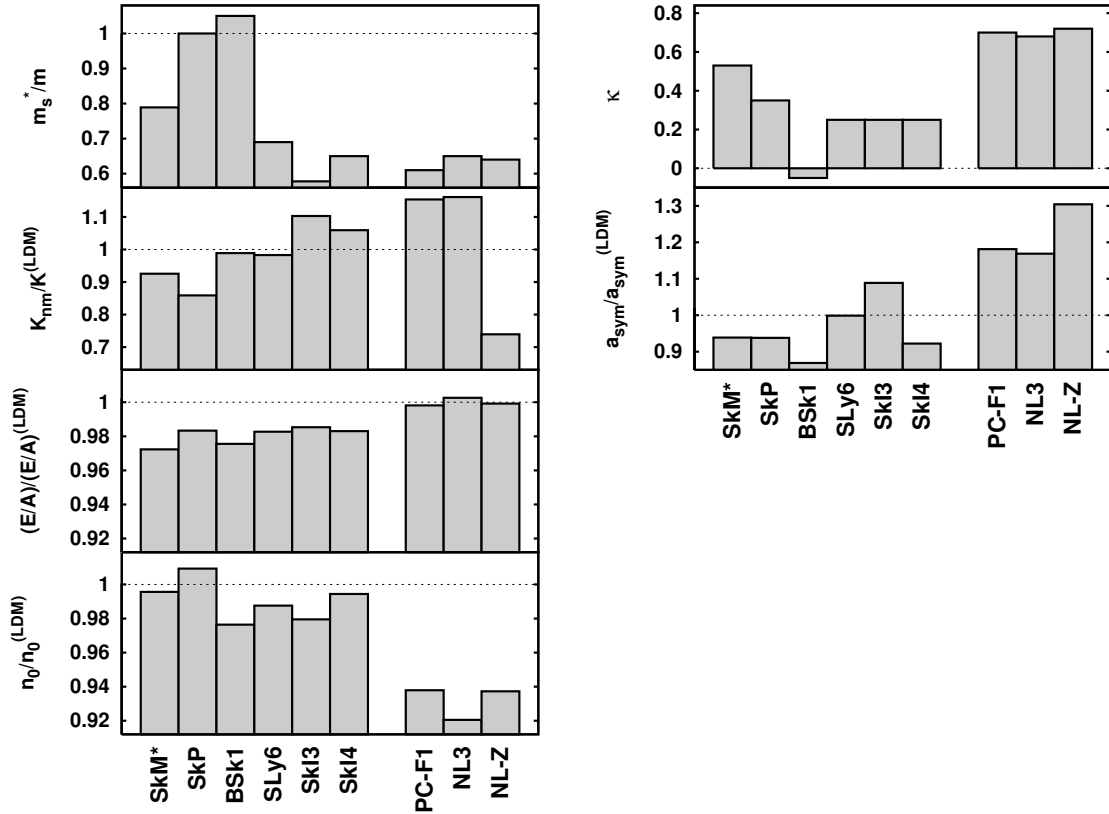


Figure 18: The key properties of nuclear matter: n_0 = saturation density of symmetric nuclear matter; E/A = binding energy per particle; $K_{nm} \equiv K_\infty$ = incompressibility; m_s^*/m = isoscalar effective nucleon mass; a_{sym} = asymmetry coefficient; κ = isovector sum-rule enhancement factor (related to isovector effective mass; Results for n_0 , E/A , K_∞ , m_s^*/m and a_{sym} are shown for a variety of Skyrme and RMF parameterizations (see Table 1) as a ratio to the corresponding LDM values [26, 236]. κ is given in absolute units as LDM value is not available for this quantity.

parameterizations with the same behavior as SkP and BSk1 in nuclear matter, identified as ‘group III’ in [28].

Finally, the *isoscalar* and *isovector* effective nucleon masses in infinite nuclear matter (denoted by m_s^*/m and m_v^*/m respectively, measured in units of the vacuum nucleon mass m) can be written as functions of the Skyrme parameters and the density of the medium. The effective neutron mass in dense asymmetric matter is then given by [235]

$$\frac{\hbar^2}{m_n^*} = (1 + I) \frac{\hbar^2}{m_s^*} - I \frac{\hbar^2}{m_v^*} \quad (36)$$

and similarly for the effective proton mass m_p^* . The isoscalar nucleon mass is deduced from the variation $\partial_\tau E$ of the the energy functional and the isovector effective mass comes from the variation $\partial_\tau E$. The latter can be also formulated in terms of the *isovector sum rule enhancement factor* κ [38] where

$$\frac{m_v^*}{m} = (1 + \kappa) \quad (37)$$

A value of $\kappa = 0$ means no enhancement, i.e. the isovector effective mass equals the bare mass. Typical are slightly positive κ around 0.25 although little is certain about this parameter (for details see [22]).

Figure 18 summarizes the predictions for these basic properties of SNM at saturation density resulting from SHF with our six parameterizations and in RMF using parameterizations PC-F1, NL-3 and

NL-Z in comparison with predictions of the Liquid Drop Model (LDM). Binding energy and saturation density show little variation within the SHF forces and agree well with the LDM values. The RMF differs, slightly but significantly. The reasons are not yet understood. The incompressibility K_∞ shows larger fluctuations, but they gather nicely around a generally accepted value of 230 MeV. The isoscalar effective mass m_s^*/m tends to values below one. It is, however, a vaguely fixed property in SHF as one can see from the large spread of results. Information on excitations is required to better constrain the effective mass, see e.g. [237, 238] for the impact of giant resonances. The RMF always prefers particularly low values which reflects the counteracting interplay of the rather strong scalar and vector fields [94].

The isovector parameters a_{sym} and κ are much less well determined because of the limited extension of isotopic chains in the nuclear landscape. There are systematic differences between SHF and RMF with RMF predicting generally larger values. The SHF values are more consistent with the LDM which gives them somewhat better credibility. Since the standard RMF model has much less flexibility in the isovector channel, it is much harder to fit long isotopic sequences and, in the extreme, sometimes impossible to produce the equation of state for pure neutron matter [239]. For that reason, extensions of the RMF are being developed which provide more isovector flexibility [102, 103].

4.2.2 β -equilibrium matter

In cold neutron stars, as the density increases from about $0.75 n_0$ up to $2-3 n_0$, nuclear matter becomes a system of unbound neutrons, protons and electrons and muons and, if enough time is allowed, will develop equilibrium with respect to weak interactions. All components that are present on a timescale longer than the life-time of the system take part in equilibrium. For example, neutrinos created in weak processes in a cold neutron star do not contribute to the equilibrium conditions as they escape rapidly. In this section we explore insights into the validity of the selected Skyrme parameterizations obtained by investigating the density dependence of the properties this homogenous phase.

BEM is characterized by the following processes:

$$n \leftrightarrow p + e^- \leftrightarrow p + \mu^- \quad .$$

Equilibrium implies that the chemical potentials should satisfy the conditions

$$\mu_n = \mu_p + \mu_e, \quad \mu_\mu = \mu_e \quad , \quad (38)$$

with each chemical potential μ_j defined by

$$\mu_j = \frac{\partial \epsilon}{\partial n_j} \quad (39)$$

where ϵ is the total energy density (27) and the n_j 's are the particle number densities. Particle fractions with respect to the total nucleon number density n are given as:

$$y_j = \frac{n_j}{n} \quad . \quad (40)$$

Charge neutrality of BEM implies $n_p = n_e + n_\mu$.

The composition of BEM has significant impact on the properties of neutron stars. In particular, the value taken by the proton fraction y_p has relevance for neutron star cooling, as discussed in [240]. The proton fraction is related to the asymmetry parameter I , introduced earlier, by $I = 1 - 2y_p$ and can also be expressed in terms of the symmetry energy (34) by [221]

$$\hbar c (3\pi^2 n y_p)^{1/3} = 4\mathcal{S}(n)(1 - 2y_p) \quad . \quad (41)$$

Table 2: Observables of nuclear matter and cold (T=0) non-rotating neutron stars: Calculated maximum mass with corresponding radius and central density, and the radius and binding energy of a 1.4 M_{\odot} star for Skyrme functionals SkM*, SkP, SLy6, SkI3, SkI4 and BSk1. The symmetry energy at saturation density n_0 , $3n_0$ and the derivative of the symmetry energy at the saturation density $\partial a_s/\partial n(n_0)$ are also given. Results for four other EoS based on different models of the nucleon-nucleon interaction, are added for comparison. See text for more explanation.

EoS	$a_s(n_0)$ [MeV]	$a_s(3n_0)$ [MeV]	$\frac{\partial a_s}{\partial n}(n_0)$	M_{\max} [M_{\odot}]	R_{\max} [km]	n_{\max}^{centr} fm $^{-3}$	$\rho_{\max}^{\text{centr}}$ g/cm 3	$R_{1.4M_{\odot}}$ [km]	E_{bin} [10^{53} ergs]
SkM*	30.01	34.02	+95	1.62	8.94	1.66	3.80	10.54	3.09
SkP	29.71	-0.43	+43	0.60	814				
SLy6	32.09	51.84	+99	2.05	10.05	1.19	2.82	11.76	2.58
SkI3	34.27	125.00	+212	2.19	11.19	0.98	2.33	13.56	2.18
SkI4	29.50	98.85	+125	2.15	10.71	1.05	2.49	12.56	2.43
BSk1	27.86	-15.06	+12	0.61	1089				
FP	31	40		1.95	9.0	1.3			
APR	33.94	59.67		2.20	10.01	1.14	2.73	11.47	2.75
BJ				1.85	9.90	1.31	3.06	11.86	2.51
Hybrid				1.45	10.45	1.36	2.76	11.38	2.49

An equation of state for zero-temperature beta-stable nucleon+lepton matter can be constructed from SHF following a procedure described previously, see e.g. [28, 225, 240]. The total energy density of the BEM is written as the sum of the nucleon and lepton contributions[225]:

$$\epsilon(n_p, n_n, n_e, n_\mu) = \epsilon_N(n_p, n_n) + n_n m_n c^2 + n_p m_p c^2 + \epsilon_e(n_e) + \epsilon_\mu(n_\mu) + n_e m_e c^2 + n_\mu m_\mu c^2 \quad (42)$$

where ϵ_N is the total nucleon energy density. The EoS for BEM is determined by two expressions [225]:

$$\rho(n) = \frac{\epsilon(n)}{c^2} \quad , \quad P(n) = n^2 \frac{d(\epsilon/n)}{dn} \quad . \quad (43)$$

where ρ is the mass density of the matter. The form used here for the EoS is obtained by eliminating n between equations (43) and evaluating the pressure as a function of the mass density ρ . This EoS forms input for neutron star models as discussed further in the following section.

For completeness we mention an important involvement of the Skyrme-like interaction in construction of EoS for BEM based on ‘realistic’ potentials (see e.g. [220] and references therein). The APR model produces only a set of numerical results of SNM and PNM energies at given densities but not as an analytic function of densities. Therefore it is necessary to fit the energies to a smooth function of density so that the derivatives needed to obtain chemical potentials (39) and the pressure (29) can be safely calculated. One then needs to interpolate between $y_p = 0.5$ (SNM) and $y_p = 0$ (PNM) results in order to find the value of y_p required by β equilibrium. The smooth function of density used in this manipulation is in the form of a generalized Skyrme interaction FPS especially fitted for this purpose but also used elsewhere [241].

4.3 Neutron Stars

A neutron star is composed of matter at densities ranging from that of terrestrial iron up to several times n_0 and, to describe this theoretically, it is necessary to use a variety of models of atomic and nuclear interactions. From the lowest densities up to 2.4×10^{-4} fm $^{-3}$ ($1.5 \times 10^{-3} n_0$), the neutron drip

point [242]), the matter is in the form of a nuclear lattice with the nuclei going from those of the iron-group up to progressively more neutron-rich ones as density increases. The electrons are initially clustered around the nuclei but form an increasingly uniform free electron gas with increasing density. Beyond the neutron drip point, free neutrons appear. Above $\sim 0.1 \text{ fm}^{-3}$ ($0.75 n_0$), nuclei no longer exist and the matter consists of homogeneous nucleon and electron fluids; with further increases of density, muons appear in coexistence with the neutrons, protons and electrons in beta equilibrium. At even higher densities, heavier mesons and strange baryons are believed to play a role (see e.g.[243] and references therein, [244, 245, 246, 247]). Ultimately, at the center of the star, a quark matter phase may appear, either alone or coexisting with hadronic matter [234, 248, 249, 250].

The SHF based models discussed in this section are used only for modeling the nucleon+lepton phase of neutron-star matter. The lower density region (the neutron star crust) will be discussed in more detail in Section 4.3.3. Since only part of the star is in the homogeneous phase, the calculated EoS needs to be matched, at lower and (possibly) higher densities, onto other EoS reflecting the composition of matter at those densities. For lower densities, the Baym-Bethe-Pethick (BBP) [251] and Baym-Pethick-Sutherland (BPS) EoS [252] is used, matching onto the Skyrme EoS at $n \sim 0.1 \text{ fm}^{-3}$ and going down to $n \sim 6.0 \times 10^{-12} \text{ fm}^{-3}$ ($3.75 \times 10^{-11} n_0$). At densities higher than $\sim 3n_0$, a hadronic EoS, for example the Bethe-Johnson (BJ), [240, 253] is appropriate. Setting up an EoS over the full density range allows calculation of one of the most important observables of a neutron star, the maximum mass. However, this maximum mass will be determined to large extent by the high density EoS and will not be a test of SHF if another EoS, such as BJ, is used. It has been argued that extrapolation of the Skyrme EoS to higher densities is not unreasonable [220, 225] and that the error made by not including the heavy baryons and possible quarks in the calculation may not be significant. We will explore consequences of this extrapolation and will discuss its validity in more detail in Section 4.3.2. We will also investigate star models at around the ‘canonical’ mass of $1.4M_\odot$ and lower in which such high densities are not reached and the applicability of SHF models is more certain.

4.3.1 Cold non-rotational neutron star models

The basic characteristic of non-rotational cold neutron star models is the relationship between the *gravitational mass* M_g and radius R of the neutron star. The most accurately measured masses of neutron stars were, until very recently, consistent with the range 1.26 to 1.45 M_\odot [254]. However, Nice et al. [255] provided a dramatic result for the gravitational mass of the PSR J0751+1807 millisecond pulsar $M_g = 2.1 \pm 0.2 M_\odot$ which makes it the most massive pulsar measured. This observation offers one of the most stringent tests for EoS use in calculation of cold neutron stars. It also sets an upper limit to the mass density, or equivalently, the energy density, inside the star [254]. A lower limit to mass density can be derived using the latest data on the largest observed redshift from a neutron star combined with its observational gravitational mass.

The gravitational mass and the radius are calculated using a tabulated form of the composite EoS with the a chosen Skyrme interaction. The Tolman-Oppenheimer-Volkov equation [256, 257]

$$\frac{dP}{dr} = -\frac{Gm\rho}{r^2} \frac{(1 + P/\rho c^2)(1 + 4\pi r^3 P/mc^2)}{1 - 2Gm/rc^2} \quad (44)$$

is integrated with

$$m(r) = \int_0^r 4\pi r'^2 \rho(r') dr' \quad (45)$$

to obtain sequences of neutron-star models which for any specified central density give directly the corresponding values for the total gravitational mass M_g and radius R of the star (the surface being at the location where the pressure vanishes).

The M_g - R relation is shown in Figure 19 for the SkM*, SLy6, SkI3 and SkI4 parameterizations together with the data for the APR model. Although each predicts a maximum mass it can be seen that only the SLy6 parameterization gives a similar mass-radius relation to APR. The level of disagreement between the other Skyrme based models and the APR is due to variation in the differences between the density dependence of the symmetry energy (asymmetry coefficient a_{sym}) in these models as shown in Figure 17. As discussed above and in detail in [28], the pressure in BEM is determined by the gradient of a_{sym} and so it follows that parameterizations predicting slower growth of a_{sym} with increasing density will give lower pressures for a given density. The size of a neutron star depends on the internal pressure generated by the star matter constituents that acts against the gravitational pressure causing shrinkage of the star. If the internal pressure vanishes (or becomes negative) the star starts to collapse. This is the case of neutron star models based on the SkP and BSk1 Skyrme parameterizations (see Table 2).

Maximum masses obtained from EoS based on SLy6, SkI3 and SkI4 parameterizations are well within the limits set by the new observation reported in [255]. On the other hand, the maximum mass of the neutron star, calculated using the SkM* parameterization is considerably lower than that for the other models shown here as expected considering the density dependence of a_{sym} for this Skyrme model.

It is also important to calculate some other important properties of these neutron star models. The total baryon number A is given by

$$A = \int_0^R \frac{4\pi r^2 n(r) dr}{(1 - 2Gm/rc^2)^{1/2}} \quad . \quad (46)$$

The total baryon number A multiplied by the atomic mass unit $931.50 \text{ MeV}/c^2$ defines the *baryonic mass* M_0 . The binding energy released in a supernova core-collapse, forming eventually the neutron star, is approximately

$$E_{\text{bind}} = (Am_0 - M)c^2 \quad , \quad (47)$$

where m_0 is the mass per baryon of ^{56}Fe . Analysis of data from supernova 1987A leads to an estimate of $E_{\text{bind}} = 3.8 \pm 1.2 \times 10^{53} \text{ erg}$ [258].

A summary of the majority of important parameters of nuclear matter and of neutron star models is given in Table 2 for the six Skyrme parameterizations of our sample. The SHF based models are compared with the APR model and some other established calculations by Bethe-Johnson [253], Friedman and Pandharipande (FP) [259] and Glendenning [234]. Details of these models are beyond the scope of this work and can be found in the original papers. We say here only that the EoS cover a great variety of different physics including non-relativistic realistic potentials [259, 220], existence of strange hyperons in dense matter [253] and quark matter coexisting with relativistic nuclear matter [234]. It is important to compare various models to study the level of sensitivity of nuclear matter and neutron star models to the physics underlying the EoS used. For example, the FP model (still taken as a benchmark in some modern work [127]) uses an old potential $v_{14} + \text{TNI}$ whilst the APR model is based on one of the most modern $\text{Av}18 + \delta v + \text{UIX}^*$ realistic potentials. The relative slope of EoS for the (SNM) and neutron (PNM) with increasing baryon number density differs fundamentally in the two models (see Table 2). At high densities, the FP model predicts decreasing symmetry energy with increasing density in contrast to the APR model. It can be seen that all models predict central energy densities at maximum mass that are within the latest limits set by Lattimer and Prakash [254]. As for the $1.4 M_\odot$ models, we note that all predicted binding energies are somewhat lower than the estimate based on the observation of the 1987A SN [258] and the corresponding radii are within the rather broad observational limits. Neither binding energy nor radius represent a strong constraint on the Skyrme parameterizations at present but increased precision of observation, and, in particular, measurement of the radius of a neutron star independently from its mass, may change the situation.

Apart from the basic mass-radius relation, there are other features of neutron stars that provide the intriguing possibility to constrain EoS and thus the nucleon-nucleon interaction in star matter. With the

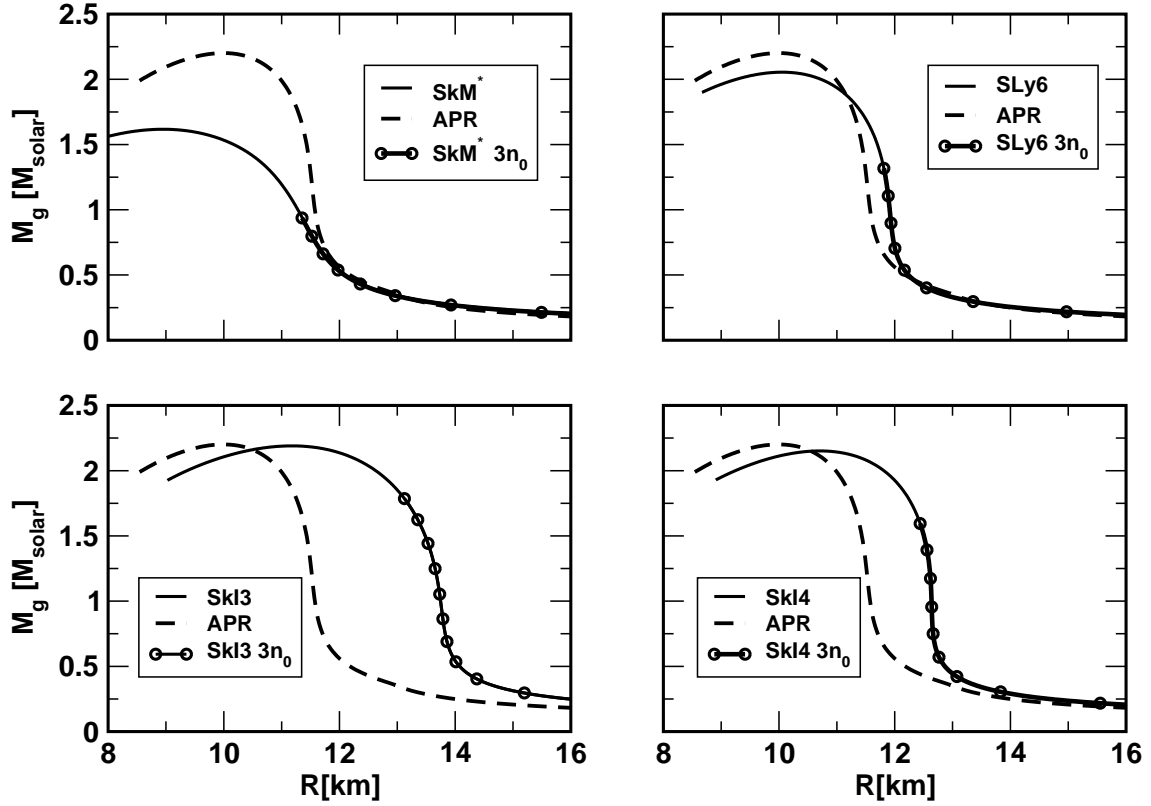


Figure 19: The predicted gravitational masses of non-rotational neutron-stars (measured in solar masses) plotted against radius (in kilometers), calculated for β -stable nucleon+lepton matter using selected Skyrme interactions, supplemented by BBP and BPS EoS's at low densities. The circles indicate a sequence of neutron star models with central density lower than $3n_0$. For more explanation see text.

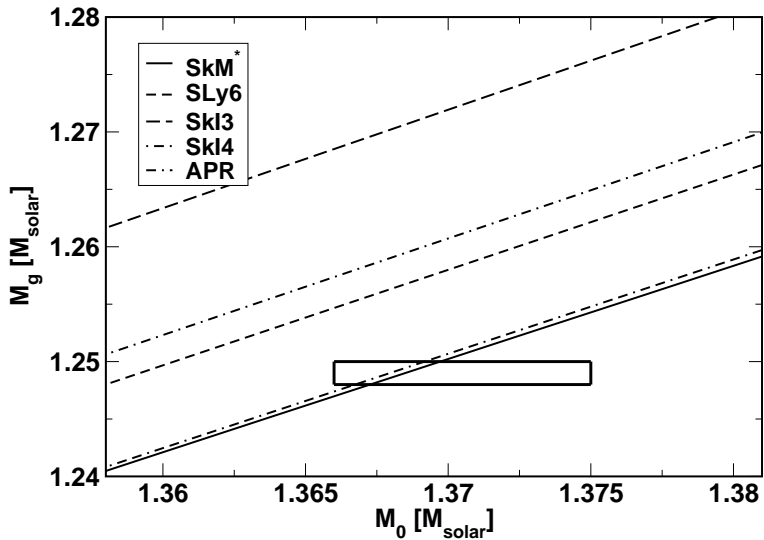


Figure 20: Relation between the gravitational mass M_g of neutron star models and their baryonic mass M_0 for SkM*, SLy6, SkI3 and SkI4 Skyrme parameterizations. The APR model is added for comparison.

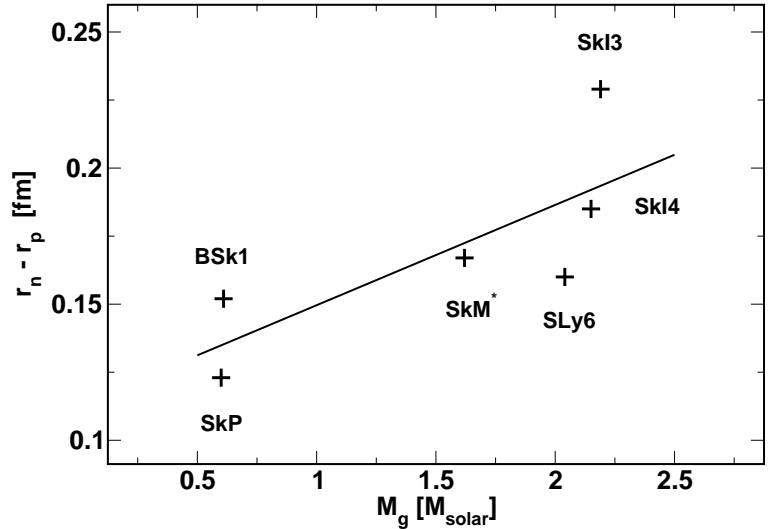
fast increasing quality and volume of observational data, these constraints are of growing importance. We will discuss some of them in the rest of this section.

An interesting possibility has been recently suggested by Lattimer and Schultz [260]. Measurement of the moment of inertia of the Pulsar A in the recently discovered double pulsar system PSR J0737-3039 to $\sim 10\%$ accuracy would allow an accurate estimate of the radius of the star and of the pressure in matter of density in the vicinity of $1\text{--}2 n_0$. This information would provide a strong constraint on the EoS of neutron stars.

Another important constraint has been recently identified [261] in connection with the very precise determination of the gravitational mass of Pulsar B in the system J0737-3039 $M_g = 1.249 \pm 0.001 M_\odot$. Assuming that Pulsar B has formed in an electron-capture supernova, a rather narrow range for the baryonic mass M_0 between $1.366\text{--}1.375 M_\odot$ of the pre-collapse core can be determined. If there is no baryon loss during the collapse, the newly born neutron star will have the same baryonic mass as the progenitor star. For any given EoS for neutron star matter the relation between the gravitational and baryonic mass is calculated. The data for Pulsar B provide a very narrow window which that relation has to satisfy. We show in Figure 20 an application of this constraint to the Skyrme parameterizations discussed in this paper. Of the parameterizations studied in this work, only SkM* passes the test, although it predicts a relatively low maximum mass of a neutron star and yields only modestly growing symmetry energy with baryon number density between n_0 and $3n_0$. This finding seems to be corroborated by the prediction of the neutron skin in ^{208}Pb as shown in Figure 21. Both these results are obtained at relatively low density (below and at nuclear saturation density). The maximum mass of a neutron star is mainly determined by the high density part of the EoS. The fact that the maximum mass of a neutron star calculated using SkM* is rather low may be connected with a the limited validity of the extrapolation procedure of the Skyrme EoS to too high densities beyond $3 n_0$ as will be discussed in more detail in Section 4.3.2. This constraint may be very important for classification of the Skyrme parameterizations because it concerns a relatively low density region where the applicability of the Skyrme interaction is almost certainly valid. The constraint is extremely stringent and may lead to an important restriction of Skyrme parameterizations beyond finite nuclei.

The issue of neutron star cooling mechanisms can, in principle, provide further important constraints on neutron-star models. However, as discussed in more detail previously [240], the cooling processes for both young and old neutron stars are not currently known with any certainty, although several scenarios have been proposed [262, 263]. We explore here the possible relevance of the direct URCA processes (the name URCA stems from the name of a casino in Rio de Janeiro; the neutrino energy loss was likened to losing money at the casino by the authors of the original paper, see

Figure 21: Calculated neutron skin in ^{208}Pb for SkM*, SLy6, SkI3 and SkI4 Skyrme parameterizations is displayed as a function of the maximum mass of a neutron star, calculated using EoS based on the same parameterization. The straight line shows the result of linear regression.



http://en.wikipedia.org/wiki/Urca_process) given by

$$n \longrightarrow p + l + \bar{\nu}_l, \quad p + l \longrightarrow n + \nu_l, \quad (48)$$

(where l stands for the leptons being considered here – electrons and muons) within the context of the Skyrme parameterizations studied in this paper. For this direct URCA process to take place, the relative components of the BEM must satisfy the appropriate conditions for conservation of energy and momentum: $y_n^{1/3} < y_p^{1/3} + y_e^{1/3}$ and $y_n^{1/3} < y_p^{1/3} + y_\mu^{1/3}$. It has been argued that this will be satisfied only at densities n several times larger than the nuclear saturation density n_0 [264, 265, 266] when the proton fraction in BEM reaches a threshold value of $\sim 14\%$. It follows from (41) that the steeper the increase of the symmetry energy with increasing number density, the faster will be the growth of the proton fraction y_p . The results for the examples of the Skyrme parameterizations investigated here are rather interesting. SkM* does not satisfy the conditions for occurrence of the direct URCA process at any density. This is in contrast to SkI3 and SkI4 for which the threshold density (and corresponding mass) for the URCA process to take place is rather low ($n_{\text{URCA}} = 0.26$ ($M_{\text{URCA}} = 0.90 M_\odot$) and 0.50 fm^{-3} ($M_{\text{URCA}} = 1.59 M_\odot$), respectively) and SLy6 for which the direct URCA process can happen only at $n_{\text{URCA}} = 1.18$ ($M_{\text{URCA}} = 2.05 M_\odot$). The latter critical density and mass are equal to those calculated in maximum mass model with the SLy6 EoS. However, we note that there are alternative direct URCA processes involving hyperons and thus this constraint, although interesting, is rather weak. Nevertheless an understanding of the cooling mechanism of neutron stars is important and the Skyrme interaction plays a significant role in these models [262]. We note that very recently a new constraint for the direct URCA cooling mechanism has been suggested, based on analysis of population synthesis scenarios [267, 268]. It finds that direct URCA process (48) should not happen in neutron stars with masses lower than $\sim 1.5 M_\odot$ (see Table 4)

It is intriguing to point out that the correlation between the properties of neutron matter and the neutron skin in finite nuclei, discussed generally in Section 3.1.3, can be extended to the correlation between maximum mass of a neutron star and the neutron skin in neutron heavy nuclei. Models of finite nuclei include surface and Coulomb effects, not present in calculation of the symmetry energy in nuclear matter and yet the distinction between Skyrme parameterizations on the basis of the *density dependence* of the symmetry energy is seen. As demonstrated in Figure 21, the Skyrme parameterizations with the steepest increase of the symmetry energy with growing density that predict the highest maximum mass of the cold neutron star, also predict the thickest neutron skin. We show this effect for Pb^{208} but it also exists in ^{132}Sn , ^{122}Zr , ^{78}Ni and ^{48}Ca , as reported in [269].

The Skyrme interaction has also been employed in a more subtle context of nuclear matter and neutron star theory. The onset of ferromagnetic instabilities in spin-polarized neutron matter at zero

and finite temperature has been investigated and identified for the SLy6 and SkI3 parameter sets [270]. It has been shown that a new constraint on the Skyrme parameters can be derived to avoid these instabilities. The instability with respect to ferromagnetic collapse was also studied in terms of Landau parameters in symmetric and neutron matter and with respect to the constraint that the velocity of sound has to remain smaller than the speed of light [271]. A set of 6 new Skyrme parameterizations has been developed using parameters obeying the suggested constraints. It is interesting to note that all these parameterizations predict decreasing symmetry energy at high densities [28].

4.3.2 Validity of the Skyrme model in high density matter: Hyperons and quark matter in neutron stars?

The current trend in the development of modern effective nuclear interactions is their applicability in finite nuclei as well as in infinite nuclear matter. In particular, the study of asymmetric nuclear matter (with neutron-proton ratio $0 \leq I \leq 1$) and pure neutron matter are of importance as an extrapolation point connecting finite nuclei at the line of stability, nuclei at the neutron drip line and some density regions of neutron stars. One has to realize that all effective nuclear interactions in use today have parameters fitted to known properties of finite nuclei at or close to the stability line and sometime properties of nuclear matter at saturation density. The isospin and density dependence of these parameters is not known. Nevertheless we routinely extend the use of these parameters up to the drip lines and expect them to work. The validity of this procedure is by no means guaranteed. Many aspects of nuclear interactions (apart from surface effects) can be tested in infinite nuclear matter and it is desirable to make such calculations. The usual argument against this procedure is that models like SHF should not be used beyond nuclear saturation density. This is a matter of debate. The general consensus is that relativistic effects are small up to $2-3 n_0$ [225] and the Skyrme interaction is well justified for the description of nuclear matter consisting of nucleons and leptons (no strange baryons or mesons)(see e.g. [225]). Indeed, in the degenerate fermi gas model, even at density $\sim 0.5 \text{ fm}^{-3}$, the relativistic correction to the mean energy of nucleons is about 10% which makes this density acceptable from that point of view. Furthermore, the requirement of low momentum approximation in the derivation of the Skyrme functional [54] sets a limit of about $(\pi k_F^{-1} > m_\pi c = 1.4 \text{ fm})$ which infers the same limiting density of 0.5 fm^{-3} .

However, we reiterate that SHF describes only the *nucleonic* part of star matter. At high density and temperature it is likely that heavy baryons and mesons will emerge at some point and contribute to the total energy of dense matter. Simple estimates of the threshold for Λ and $\Sigma^{\pm,0}$ hyperons just based on their rest-mass, were discussed in [28] showing a possibility that these particles will exist in matter at $3 n_0$ and even below ($1.5-2.0 n_0$). This simple estimate neglects the contribution to the threshold energy from the hyperon-nucleon and hyperon-hyperon interaction, which is unknown at present and has been modeled in a variety of ways, mainly in relativistic models (see e.g. [234, 247, 250]), again predicting hyperon creation close to, or below the $3 n_0$.

Another issue that is of even more wide ranging consequence is the question of the critical density when nucleons will start to loose their identity and (partially) deconfined quark matter will emerge. At densities of about $3 n_0$ the nucleons will start to overlap and formation of six-quark bags and increasing interaction strength between quarks of different nucleons will become more likely. Again, some calculations predict this critical density to be below n_0 [234, 250]. Clearly no model based on nucleon degrees of freedom should be used for the description of matter with a significant deconfined quark component.

Non-nucleonic components in nuclear matter will affect the EoS, in particular they will tend to decrease the slope of \mathcal{E} as a function of density (the EoS softens). As it was shown above, this affects all the observables of dense matter and other quantities like the maximum mass of cold neutron stars. Furthermore, it is important to realize that if we limit the EoS only to hadronic degrees of freedom,

current neutron star models are not strictly speaking valid at the baryon number densities of about 6–10 n_0 , needed to calculate maximum mass models because at these densities nucleons and hyperons are likely to lose their identity as composite particles and make a partial or possibly complete transition to quark matter. Following this logic, the neutron star models shown in Figure 19 should be calculated only up to masses and radii indicated by circles on the M_g – R curves and the maximum mass of cold neutron stars would not be obtainable from such models.

4.3.3 Inhomogeneous matter.

In the previous sections, we discussed applications of SHF to models of homogeneous nuclear matter consisting of unbound baryons and leptons. However, there is a large inhomogeneous phase of matter at lower densities that is present in crusts of neutron stars and forms a part of the collapsing core at type II supernovae. As already mentioned above, at densities below $\sim 6 \times 10^{-11} \text{ fm}^{-3}$ the matter in this ground state consists of ^{56}Fe nuclei arranged in a lattice to minimize their Coulomb energy. A fraction of electrons are bound to the ^{56}Fe nuclei. In the density range $\sim 6 \times 10^{-11} \text{ fm}^{-3} < n < 2.5 \times 10^{-4} \text{ fm}^{-3}$ the equilibrium nuclei, now immersed in a relativistic electron gas but still distributed in a lattice, become more neutron-rich as electron capture and inverse β -decay take place while direct β -decay is inhibited by the lack of unoccupied electron states. At about $2.5 \times 10^{-4} \text{ fm}^{-3}$ (the neutron drip-line) finite nuclei cannot support the neutron excess and start to emit neutrons to continuum neutron states. From this density up to about 0.1 fm^{-3} , where the transition to homogeneous nuclear matter occurs, there are still bound nucleons, coexisting with a free neutron and electron gases. The modeling of this most interesting region is difficult as equilibrium emerges as result of a delicate balance between nuclear surface energy (favoring large nuclei) and the Coulomb energy, the sum of the positive nuclear self-energy and negative lattice-energy, which favors small nuclei. The current understanding is that the nuclei form exotic phases (‘the pasta phase’) like rods, slabs, tubes, inside-out bubbles, spaghetti or lasagna, stabilized by the Coulomb interaction and characterized by various crystal lattice structures [272, 241, 273].

The models used for the description of inhomogeneous matter phase fall into two categories. One uses the semi-empirical mass formula or the compressible liquid drop model (LDM) for the description of finite nuclei and a separate model to calculate the free neutron gas energy density (e.g. [274, 275, 276, 277]). The second category includes self-consistent models that use the same interaction to describe the nuclear matter inside and outside the finite nuclei (e.g. [251, 278, 272, 273]). The advantage of the second class of models is obvious as they include in a consistent way the effect of the external nucleons on nuclei which are not isolated but embedded in the sea of neutrons. The main interest of these calculations has focused on subnuclear densities, in particular the ‘pasta’ phase and the location and properties of the phase transition between homogeneous and inhomogeneous matter. We note that there is no need for a self-consistent calculation of homogeneous matter as in this case the energy per particle \mathcal{E} and related quantities can be expressed analytically (24a).

A major group of models use SHF to determine the ground state energy of matter as a function of density, temperature and proton fraction by minimization of the SHF energy density in coordinate space. In this way the equilibrium energy per particle can be calculated as a continuous function of density and the composition of nuclear matter is determined naturally without *a priori* assumptions about particular physical processes in certain density regions. One of the first models of this kind was developed by Bonche and Vautherin [279] for inhomogeneous matter assuming spherical symmetry (1D space) using the SkM and RPB Skyrme interactions. Later it was adopted by Hillebrandt and Wolff [280] with RATP, Ska and SkM Skyrme parameterizations for tabulation of the EoS in a dense grid of energy density, temperature (or entropy) and electron fraction for use in hydrodynamical codes (for more details see section 4.3.4). Pethick et al. [278] used the Skyrme1’, FPS and FPS21 parameterizations in their EoS. The Gogny parameterization D1 has been also used to construct finite temperature EoS

[281, 282] based on the application of the variational principle to the thermodynamical potential with special attention to the liquid-gas phase transition. A semi-classical approximation to SHF, the ETFSI method, with the parameterizations RATP, SkM* and SkSC4–10 was also applied to derive EoS at finite temperatures for inhomogeneous [283] and homogeneous [284] nuclear matter under conditions appropriate to a collapsing star assuming spherical symmetry. The EoS based on the RMF theory with the TM1 parameter set for the RMF Lagrangian was used in modeling supernova physics by Shen et al., [285]. Both, homogeneous and inhomogeneous, matter are treated within the model. However, the inhomogeneous matter is not calculated fully self-consistently but is approximated as a b.c.c lattice of spherical nuclei and the free energy is minimized with respect to cell volume, proton and neutron radii and surface diffuseness of the nuclei and densities of the outside neutron and electron gases. Menezes and Providência [250] used RMF to construct EOS of mixed stars formed by hadronic and quark matter in β equilibrium at finite temperature. The non-linear Walecka model and the MIT Bag and Nambu-Jona-Lasinio models were used for the hadronic and quark matter, respectively.

The major limitation of the models discussed so far, i.e. the assumption of spherical symmetry for inhomogeneous matter, has been removed in the recent work of Magierski and Heenen [273] who treated cold ($T = 0$) nuclear matter in the density region of the ‘pasta’ phase for the first time fully self-consistently in 3D coordinate space (allowing for triaxial shapes) using SHF with SLy4 and SLy7 parameterizations. The SHF equations were solved in a rectangular box with periodic boundary conditions. This includes naturally shell effects in neutron gas and pairing. In calculation of the Coulomb energy, the model goes beyond the Wigner-Seitz approximation of spherical cells (assumed in all the previously mentioned models) and includes both interactions between nuclei on different lattice sites and between protons and electrons. Unfortunately no comparative study has been done as yet to systematically explore the sensitivity of properties of inhomogeneous matter to the choice of the SHF parameterization in comparison with the other models.

4.3.4 Hot matter and type II (core-collapse) supernova models.

The most sought after constraint on EoS in hot matter would be based on success in modeling a type II core-collapse supernova. There is no doubt that the supernova phenomenon exists in nature and is accompanied by an explosion. Current models fail to reproduce this explosion. One of the possible solutions of this problem lies in the improvement of the EoS since the EoS at subnuclear densities controls the rate of collapse, the amount of de-leptonization and thus the size of the collapsing core and the bounce density. During the supernova collapse and the birth of a proto-neutron star the matter can reach temperatures up to 20 MeV and thus the finite temperature EoS is used. The density at bounce of the collapsing core (for a detailed description of the core collapse mechanism see e.g. [286]) goes up to $1.5\text{--}2.0 n_0$ and thus includes both homogeneous and inhomogeneous phases and the phase transition between the two. Moreover, it may be just reaching the threshold for the appearance of exotic components, like strange baryons and mesons, with possibly a phase transition to quark matter at the upper end of the density region. The timescale for supernova collapse is believed to be of order of a second and the matter does have enough time to reach β equilibrium throughout the rapid changes. Thus the calculation has to be performed for a fixed ratio of neutrons and protons, usually y taken $y_p \sim 0.3$ [286] and a relevant range of densities and temperatures. There are so far two examples of a finite temperature EoS, based on SHF, for use in supernova simulation codes. The early calculations of Hillebrandt and Wolff, mentioned in the previous section, used a spherically symmetrical SHF model (1D) [280]. As a new development, Newton and Stone [224, 287] extended the previous SHF 3D calculation [273] to finite temperature and wide range of densities for use in supernova simulation models. The calculation scheme (using SkM* at present) treats the finite nuclei and the neutron gas in the ‘pasta’ phase as one entity and naturally allows effects such as (i) neutron drip, which results in an external neutron gas, (ii) the variety of exotic nuclear shapes expected for extremely neutron

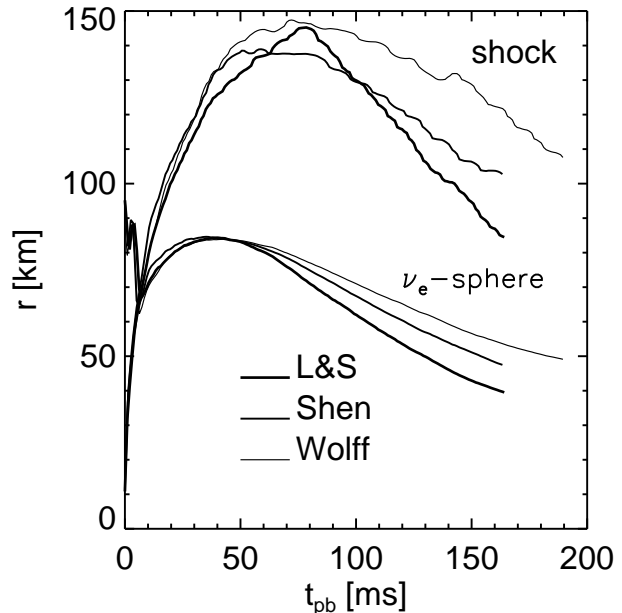


Figure 22: Shock positions and neutrino sphere radii of ν_e as a function of time after bounce for collapse simulations of a $15 M_{\odot}$ progenitor star with three EoS. The figure has adopted from [288]. See text for more explanations.

heavy nuclei including, but not confined to, the ‘spaghetti’ and ‘lasagne’ phases previously identified, and (iii) the subsequent dissolution of these structures into homogeneous nuclear matter. The EoS is calculated across phase transitions without recourse to interpolation techniques between density regimes described by different physical models [287]. The elimination (or significant smoothing) of the phase transitions has serious consequences, e.g., for neutrino transport in the ‘pasta’ phase. It is clear that neutrino-nucleon and neutrino-nucleus cross-sections cannot be considered just as contributions from finite isolated nuclei and free neutron and electron gas, but the complex density distribution of particles will have to be taken into account.

An interesting comparison has been made recently by Janka *et al.* [288] who followed the development of the shock radius and electron neutrino luminosity over the first 200 ms after core collapse using three different EoS, Lattimer and Swesty [277] based on LDM, Shen *et al.* [285] using RMF and Hillebrandt and Wolff [280] utilizing SHF; the differences found may be seen as an example of sensitivity of some predictions of supernova simulation models to the choice of EoS.

5 Summarizing constraints on Skyrme parameterizations

In this Section we draw together various constraints which are applicable to confine the choice of SHF parameterizations and make some suggestions concerning their implementation. This is a rather long list which is, to some extent, still under development. In fact, all practical adjustments of the Skyrme parameters up to now have started from fitting a subset of these constraints, mainly the gross properties of binding (Section 5.1.1), selected information on spin-orbit splitting (Section 5.1.2), data on odd-even staggering for pairing (Section 5.1.4), and occasionally nuclear matter properties. The other features listed here are usually inspected a posteriori. The extensive list of check-points presented here has never been utilized in fitting procedures in full before.

All observables in finite systems (see Section 5.1) have to be checked for possible correlation effects from soft modes (see Section 3.4). Gross properties are generally robust while details as, e.g., isotopic and isotonic differences are more likely to be affected.

5.1 Finite nuclei

5.1.1 Gross properties: energy, charge radii

The most important features to be properly reproduced are the nuclear bulk properties:

binding energy E_B ,
charge r.m.s. radius r_{ch} ,
charge diffraction radius R_{ch} , and
charge surface thickness σ_{ch} .

These are usually considered in a large selection of spherical (doubly magic and semi-magic) nuclei. Thus nuclei which are likely to carry sizeable correlations should be excluded. This holds, e.g., for nuclei with $N = Z$ because of a rather large Wigner energy. Light nuclei should also be scrutinized for correlation effects. The best possible selection of experimental data is still a question of debate.

5.1.2 Spin-orbit splitting

The spin-orbit splitting is automatically provided in RMF but has to be adjusted ‘by hand’ in SHF. Experimental data for this adjustment are taken from the spectra of doubly-magic nuclei, for levels which are close to the Fermi energy and thus rather free from polarization and correlation effects. Up to now, almost all fits have considered spin-orbit splittings only in ^{16}O and ^{208}Pb . Other options for which good data exist, such as ^{40}Ca , ^{48}Ca , ^{90}Zr , or ^{132}Sn , should be exploited.

5.1.3 Neutron radii

Information on neutron radii r_n and/or neutron skin $r_n - r_p$ are most useful to pin down the isovector properties of the parameterization, particularly the symmetry energy a_{sym} . The problem here is that r_n is deduced from model-dependent analysis of scattering experiments. To overcome this obstacle, direct modeling of the scattering process by SHF should be considered.

5.1.4 Energy differences

The odd-even staggering of binding energies in medium heavy and heavy nuclei is used to adjust the pairing strength. It is recommended to use the staggering from the five-point difference formula to minimize perturbation from competing polarization (Jahn-Teller effect) [73].

Two-proton and two-neutron separation energies can supply information on shell structure, particularly on the magnitude of shell gaps. A proper description is crucial for the predictive value of SHF in application to the r-process (see Section 3.3). However, one has to be aware of possible correlation effects on this quantity (see Section 3.4.2).

5.1.5 Isotopic shifts

The isotope shift in radii of Pb can be used a test of the strength of the isovector spin-orbit force [56].

Much information is contained in other chains to, such as the negligible difference in charge radii between ^{40}Ca and ^{48}Ca , or the large shift in certain regions of, e.g., Sr or Hg isotopes. However, these chains are likely to include sizeable correlation effects.

5.1.6 Deformations

More advanced test cases can be found in properties of deformed nuclei, their ground state deformations and rotational bands. A possible selection may be:

- deformation in heaviest nuclei (^{264}Hs),
- triaxial deformation (^{138}Sm , ^{188}Os),
- octupole deformation ($^{222,224}\text{Th}$, ^{146}Ba),
- super-deformed states ($^{192,194}\text{Hg}$, ^{194}Pb , ^{238}U),
- hyper-deformed states (^{232}Sm),
- prolate-oblate competition ($^{184,186}\text{Pt}$, $^{184,186}\text{Hg}$),
- spherical-to-deformed transition in heavy Zr isotopes $^{96,98,100}\text{Zr}$, and/or fission barriers in actinides.

Deformation properties are often sensitive to details of the shell structure and constitute extremely critical tests. Nuclei with well developed stable deformation are generally well described within a mean-field model. Transitional regime, although very interesting, has to be investigated for possible influence of correlation effects.

5.1.7 Excitation properties

Excitation properties provide a rich pool of information. Giant resonances in heavy nuclei are closely related to key properties of nuclear matter such as incompressibility (isoscalar monopole), symmetry energy (isovector dipole), or effective mass (isoscalar quadrupole). The isovector dipole resonance in light nuclei is not yet under control and presents a big puzzle (see Section 3.2.1).

Excitation with unnatural parity as, e.g., the Gamow-Teller resonances can serve to fix the not so well known properties of SHF in the spin channel (see Section 3.2.2). There is still a long road ahead in exploiting these aspects.

Low-energy quadrupole excitations carry combined information on shell structure (near doubly magic nuclei) and on pairing. However, the modeling has yet to be improved in order to truly optimize the large amplitude collective path (see Section 3.4.1).

5.2 Nuclear matter and neutron star models

The constraints on nuclear matter properties are of two types. The first concerns expected values of some empirical quantities at nuclear saturation density n_0 . These values and/or their lower and upper limits, coming from merging data obtained from LDM or indirectly from experiments as discussed in Section 4.2.1, are summarized in Table 3. The LDM values are an extrapolation from finite nuclei data, similarly as the various SHF values. They serve merely as an orientation to the extent that models which deviate too much from these ‘commonly accepted values’ are to be questioned.

The second type of constraint is given by the *density dependence* of energy per particle \mathcal{E}_0 , the asymmetry coefficient $a_{\text{sym}}(n_0)$, the isoscalar effective nucleon mass m_s^*/m and derived quantities like the pressure, incompressibility and the velocity of sound in SNM, PNM and BEM. There is no firmly based set of values of these quantities and their various dependences. The best that can be done is to compare their predicted values to a ‘realistic’ *ab initio* theoretical model. However, they have a profound effect on the EoS used in neutron star models which can indeed in turn can be tested against observational data. Although the data are still lacking desired accuracy and are related to each other (usually as a function of the star mass), they have already proven to be powerful enough to eliminate some EoS (and thus Skyrme parameterizations) from use in neutron star models [28] although they perform well in finite nuclei. Considerable progress in increasing the quality of data on cold neutron stars is expected in the near future when, for example, there is hope to have independent values of

Table 3: Summary of constraints from nuclear matter at saturation density. The “commonly accepted values” are taken from the LDM as published in [26, 236]. The calculated values for the Skyrme parameterizations used in the review are given for illustration. All symbols are explained in the text.

Constraint	LDM	SkM*	SkP	SLy6	SkI3	SkI4	BSk1
n_0 [fm ⁻³]	0.16 ± 0.01	0.160	0.163	0.159	0.158	0.160	0.157
\mathcal{E}_0 [MeV]	-16.1 ± 0.1	-15.77	-15.95	-15.92	-15.98	-15.94	-15.80
K_∞ [MeV]	230 ± 20	217.5	201.9	230.8	259.0	249.1	232.1
$a_{\text{sym}}(n_0)$ [MeV]	31 ± 1.5	30.06	30.02	32.00	34.89	29.54	27.82
m_s^*/m	1.0	0.79	1.00	0.69	0.58	0.65	1.05

Table 4: Summary of constraints from properties of cold neutron stars. Fulfilment of some of these constraints for the sample Skyrme parameterizations is indicated by ‘+’ (fulfilled), ‘(+)’ (fulfilled but the constraint is weak), ‘-’ (failed). ‘0’ stays for undecided as either the constraints is uncertain at present or the property was not tested for the parameterization in question. Symbols are explained in the text.

Constraint	Expected value	SkM*	SkP	SLy6	SkI3	SkI4	BSk1
M_{max} [M _⊙]	2.1 ± 0.2 0	-	+	+	+	-	
R_{max} [km]	8–15	+	-	+	+	+	-
$R_{1.4\odot}$ [km]	9–16	+	-	+	+	+	-
E_{bin} [10 ⁵³ ergs]	3.8 ± 1.2	0	-	0	0	0	-
$\rho_{\text{max}}^{\text{centr}}$ [10 ¹⁵ gcm ⁻³]	0.5–4.0	(+)	-	(+)	(+)	(+)	-
M_0 [M _⊙]	1.356 < 1.375	+	-	-	-	-	-
M_{URCA} [M _⊙]	> 1.5	0	-	+	0	+	-

neutron star radii rather than values determined as a function of the gravitational mass. The recently proposed method of its independent determination could be realized in a few years [260]. We list in table 4 the main constraints based on neutron star models.

Certain other constraints, such as those connected with polarized nuclear matter and its ferromagnetic collapse, have not been quantified as yet for the majority for SHF models and are yet to be explored. We mention that very recently [268] a similar set of constraints has been suggested for testing effective interactions used in EoS based on RMF models.

5.3 Supernova simulations

The most powerful constraint on the SHF equation of state would be achieving the explosion of the core-collapse supernova model. It is important to reiterate that the density region at which this collapse is expected to happen (1.5–2.0 n_0) is well within the expected window of validity of the SHF model beyond the saturation density. However these tests are rather complicated as there are certain other factors in the supernova process that may affect the occurrence of the explosion and their relation with the EoS are not fully established. However, supernova physics offers a new ground for testing the SHF models which is just starting to be explored [190].

6 Conclusions

The application of the Skyrme Hartree-Fock model (SHF) to finite nuclei, nuclear matter and in astrophysical contexts has been critically surveyed, with occasional consideration links of its relativistic cousin, the relativistic mean-field model, and to ab-initio models. SHF provides an effective energy-functional which is motivated by many-body theory and leaves about 6–12 free parameters which are adjusted phenomenologically. The functional is universal in the sense that it, in principle, applicable to all nuclei (except the very light) irrespective to their shape or shell structure. The current models usually calculate static and dynamical properties of even-even nuclei exactly and approximate models for odd-A and odd-odd nuclei in some fashion, although an exact approach is in principle possible and is waiting to be implemented in SHF codes. Static observables include nuclear ground state binding energies, profile and shape of charge and neutron density distributions, nuclear radii and fission barriers. The SHF models provide, in the small-amplitude limit of TDHF, useful information on the excitation spectrum, particularly on the various giant resonances which form important features of the nuclear excitation spectrum. Moreover, the large amplitude limit of TDHF covers a wide range of phenomena, low-lying collective modes, fission, rotational bands, fusion and nuclear collisions.

The overall global agreement of the SHF model with existing data is overwhelmingly good. Local discrepancies in SHF predictions, however, exist which is fully understandable because the effective functionals has a simple analytical form and is preferably appropriate for reproducing smooth trends. Moreover, the isospin and density dependence of these parameters is not yet well known. It is often observed that local deviation between SHF calculation and experiment is not statistical but exhibits systematic trends which indicate aspects for future improvement (see Section 3.1.1). As an example, discrepancies between experimental and calculated two-neutron-separation energies may originate in detailed, but locally important, physics like shell effects, shape fluctuations and level densities at the Fermi surface to which global observables have limited sensitivity. Similarly, the whole range of dynamical nuclear properties is reproduced well by the SHF model, again with exception which constitute major challenges yet to be addressed (see Section 3.2). For example, no SHF parameterization can simultaneously reproduce the average peak position of the GDR in heavy and light nuclei.

Discrepancies between results of SHF calculation and experimental data often originate from correlations beyond mean field (see Section 3.4). There is a large potential for systematic investigation of these effects that may lead to better understanding of the limitations of the SHF and similar self-consistent mean-field models. Another major improvement can be achieved by gradual elimination of imperfections in fitting of the Skyrme energy functional. It is well known that due to mutual correlation between the variable parameters of the Skyrme functional, there is, in principle, an infinite number of combinations of the parameters which could be fitted to experimental data and produce results with an equally satisfactory agreement with experiment. There exists already a great manifold of such sets in the literature and it is very difficult to make a well founded choice between them, in particular in calculations of properties of finite nuclei. This situation is not unique to SHF but a generic problem of all types of nuclear effective energy functionals. It is caused by the fact that an ab-initio derivation of the functionals is hindered by the uncertainty in the true nature and form of the genuine nucleon-nucleon interaction in the nuclear environment.

One way forward in confining the manifold of permissible parameterizations is to systematically increase the amount and variety of experimental data used in the fitting process. Attempts to use only one selected type of observable in fitting, like nuclear masses, and to ignore all the other experimental data, did not meet with real success. The common practice adopted in fitting of most parameterizations is to use ground state properties of magic or semi-magic nuclei in the hope that these nuclei will be least affected by correlations beyond the mean field and that many effects like shape fluctuation, shell effects and pairing may be neglected. The increasing amount of experimental information on nuclei far from stability allows to include more stringent information, particularly concerning isovector properties of the

effective interactions. This should improve steadily the extrapolative power of SHF which is at present still rather unsatisfactory (i.e. the deviation between predictions of different SHF parameterizations is increasing with growing distance from the stability line which causes extrapolation of SHF models to the drip-line regions lacking credibility). Establishing more reliable extrapolations is the major challenge for future development because that is desperately needed for a variety of astrophysical applications, like understanding the r-process. The same holds for the construction of SHF based EoS for description of nuclear matter under extreme conditions of high density and temperature that exists in neutron star and supernovae. Similarly, in terrestrial ‘extreme’ conditions, reliable EoS are desirable for modeling of heavy-ion collision processes and investigations of super-heavy nuclei.

We believe it would be very beneficial to develop modern Skyrme parameter sets that would satisfy simultaneously the extended set of constraints summarized in Section 5. Although this will not create a *unique* set of the Skyrme parameters, it will give the best chance to create a model that would be applicable on a global scale. It has been shown in Section 4 that properties of nuclear matter even at densities below $3 n_0$ offer a sensitive test of the Skyrme parameterizations. It is plausible that extension of the SHF models to systems with high values of isospin, like cold neutron stars, would provide a distant extrapolation point with the closed-shell stable nuclei at the other extreme and the neutron-drip-line nuclei between the two. This development may even give us a better insight into the physical connection between Skyrme parameters (or their selected combinations) and some nuclear properties and thus give more control over the model. As long as a quantitative performance of more fundamental models of nuclear interactions, perhaps based on subnucleon degrees of freedom, is still ahead in the future, up-to-date SHF models are likely to remain an important tool in low-energy nuclear physics and astrophysics for some time to come.

7 Acknowledgements

We wish to thank N. J. Stone for reading of the manuscript and many constructive suggestions. Helpful comments of D. M. Brink, D. Dean, P. Guichon, W. R. Hix, P. Klüpfel, K.-L. Kratz, J. C. Miller and B. Pfeiffer are gratefully acknowledged. This work has been supported by US DOE grant DE-FG02-94ER40834, from DOE Scientific Discovery through Advanced Computing Grant, and from the BMBF (project 06 ER 124).

A Appendix 1

A.1 Parameters of the sample group of Skyrme parametrisations in nuclear matter calculations

Parameters of the Skyrme parametrizations SkM*, SkP, SLy6, SkI3, SkI4 and BSk1 are listed in Table 5.

Table 5: Parameters of the sample Skyrme interactions. For definitions see (11,12).

Skyrme	B_0	B'_0	B_1	B'_1	B_3	B'_3	α
SkM*	-1983.75	-780.28	2924.06	974.69	34.688	34.063	0.166667
SkP	-2198.78	-1161.17	3507.93	1592.67	-0.000	44.642	0.166667
SLy6	-1859.63	-1642.67	2563.69	3170.43	58.621	-26.016	0.166667
SkI3	-1322.16	-712.47	1519.91	1816.40	96.258	-63.957	0.25
SkI4	-1391.87	-839.84	1819.43	1995.55	69.927	-37.655	0.25
BSk1	-1372.84	-1006.74	2520.88	2223.54	-6.277	0.000	0.333333

Skyrme	t_0	t_1	t_2	t_3	x_0	x_1	x_2	x_3	α
SkM*	-2645.00	410.00	-135.00	15595.00	0.090	0.000	0.000	0.000	0.166667
SkP	-2931.70	320.62	-337.41	18708.96	0.292	0.653	-0.537	0.181	0.166667
SLy6	-2479.50	462.18	-448.61	13673.00	0.825	-0.465	-1.000	1.355	0.166667
SkI3	-1762.88	561.61	-227.09	8106.20	0.308	-1.172	-1.091	1.293	0.25
SkI4	-1855.83	473.83	1006.86	9703.61	0.405	-2.889	-1.325	1.145	0.25
BSk1	-1830.45	262.97	-296.45	13444.70	0.600	-0.500	-0.500	0.823	0.333333

References

- [1] R. Machleidt and I. Slaus, J. Phys. G **27** (2001), R69.
- [2] W. H. Dickhoff and H. Müther, Rep. Prog. Phys. **55** (1992), 1947.
- [3] H. Heiselberg and Vijay Pandharipande, Annual Review of Nuclear and Particle Science **50** (2000), 481.
- [4] M. Lutz, B. Friman, and Ch. Appel, Phys. Lett. **B474** (2000), 7.
- [5] N. Kaiser, S. Fritsch, and W. Weise, Nucl. Phys. **A700** (2002), 343.
- [6] W. Weise, Nucl. Phys. **A751** (2005), 565.
- [7] H. Bohr, C. Providencia, and J. da Providencia, Phys. Rev. **C71** (2005), 055203.
- [8] P. Navratil, J. P. Vary, and B. R. Barrett, Phys. Rev. C **62** (2000), 054311.
- [9] C. Forseen, P. Navratil, W. E. Ormand, and E. Caurier, Phys. Rev. **C71** (2005), 044312.
- [10] S. C. Pieper and R. B. Wiringa, Phys. Rev. **C70** (2004), 054325.
- [11] M. Wloch, D.J. Dean, J.R. Gour, M. Hjorth-Jensen, K. Kowalski, T. Papenbrok, and P. Piecuch, Phys. Rev. Lett. **94** (2005), 212501.

- [12] R. Roth, H. Hergert, P Papakonstantinou, T. Neff, and H. Feldmeier, PRC **72** (2005), 034002.
- [13] P. Navratil, private communication, 2006.
- [14] P. Möller, J. R. Nix, and K.-L. Kratz, At. Data Nucl. Data Tables **66** (1997), 131.
- [15] W. D. Myers and W. J. Swiatecki, Annual Review of Nuclear and Particle Science **32** (1982), 309.
- [16] S. G. Nilsson and I. Ragnarsson, *Shapes and shells in nuclear structure*, Cambridge University Press, Cambridge, 1995.
- [17] P. Möller, J.R. Nix, W.D. Myers, and W.J. Swiatecki, At. Data Nucl. Data Tab. **59** (1995), 185.
- [18] S. E. Koonin, D. J. Dean, and K. Langanke, Phys. Rep. **278** (1997), 1.
- [19] I. Zh. Petkov and M. V. Stoitsov, *Nuclear density functional theory*, Clarendon Press, Oxford, 1991.
- [20] P.-G. Reinhard, Inst. Phys. Conf. Ser. **132** (1992), 157.
- [21] R. M. Dreizler and E. K. U. Gross, *Density functional theory*, Springer, Berlin, Heidelberg, New York, 1990.
- [22] M. Bender, P.-H. Heenen, and P.-G. Reinhard, Rev. Mod. Phys. **75** (2003), 121.
- [23] M. Brack and P. Quentin, Nucl. Phys. **A361** (1981), 35.
- [24] M. Brack, C. Guet, and H.-B. Haakansson, Phys. Rep. **123** (1985), 275.
- [25] Y. Aboussir, J. M. Pearson, A. K. Dutta, and F. Tondeur, Nucl. Phys. **A549** (1992), 155.
- [26] W. D. Myers and W. Światecki, Phys. Rev. C **58** (1998), 3368.
- [27] ———, Phys. Rev. C **60** (2000), 054313.
- [28] J. Rikowska Stone, J. C. Miller, R. Koncewicz, P. D. Stevenson, and M. R. Strayer, Phys. Rev. **C68** (2003), 034324.
- [29] G. Dissertori, I.G. Knowels, and M. Schmelling, *Quantum chromodynamics: High energy experiments and theory*, Clarendon Press, Oxford, 2003.
- [30] P.-G. Reinhard and C. Toepffer, Int. J. Mod. Phys. **E3** (1994), 435.
- [31] V. R. Pandharipande, I. Sick, and P. K. A. deWitt Huberts, Rev. Mod. Phys. **69** (1997), 981.
- [32] H. Kümmel, K. Lührmann, and J. Zabolitzky, Phys. Rep. **36** (1978), 1.
- [33] R. D. Mattuck and A. Theumann, Adv. Phys. **20** (1971), 721.
- [34] R. Brockmann and R. Machleidt, Phys. Rev. C **42** (1990), 1965.
- [35] P.-G. Reinhard and D. Drechsel, Z. Phys. **A290** (1979), 85.
- [36] W.M. Alberico, A. Molinari, R. Cenni, and M.B. Johnson, Ann. Phys.(NY) **138** (1982), 178.
- [37] A.D. Jackson, A. Lande, and R.A. Smith, Phys. Rep. **86** (1982), 55.

- [38] P. Ring and P. Schuck, *The nuclear many-body problem*, Springer–Verl., New York, Heidelberg, Berlin, 1980.
- [39] P.-G. Reinhard and K. Goeke, *Rep. Prog. Phys.* **50** (1987), 1.
- [40] Giu Do Dang, A. Klein, and N. R. Walet, *Phys. Rep.* **335** (2000), 93.
- [41] H. Reinhardt, *Nucl. Phys. A* **369** (1981), 122.
- [42] K. Goeke, P.-G. Reinhard, and H. Reinhardt, *Nucl. Phys.* **A378** (1982), 474.
- [43] ———, *Phys. Lett.* **118B** (1982), 1.
- [44] A. Klein and E.R. Marshalek, *Rev. Mod. Phys.* **63** (1991), 375.
- [45] C. Toepffer and P.-G. Reinhard, *Ann. Phys.* **181** (1988), 1.
- [46] C. Fuchs, *Prog. Part. Nuc. Phys.* **56** (2006), 1.
- [47] T.T.S. Kuo and E. Osnes, *Nucl Phys. A* **205** (1973), 1.
- [48] J. W. Negele and D. Vautherin, *Phys. Rev.* **C5** (1972), 1472.
- [49] S. Weisgerber and P.-G. Reinhard, *Z. Phys. D* **23** (1992), 275.
- [50] P.-G. Reinhard and E. W. Otten, *Nucl. Phys.* **A420** (1984), 173.
- [51] T. H. R. Skyrme, *Phil. Mag.* **1** (1956), 1043.
- [52] ———, *Nucl. Phys.* **9** (1959), 615.
- [53] D. Vautherin and D. M. Brink, *Phys. Lett.* **32B** (1970), 149.
- [54] ———, *Phys. Rev.* **C5** (1972), 626.
- [55] S. Krewald, V. Klemt, J. Speth, and A. Faessler, *Nucl Phys. A* **281** (1977), 166.
- [56] P.-G. Reinhard and H. Flocard, *Nucl. Phys.* **A584** (1995), 467.
- [57] Y. M. Engel, D. M. Brink, K. Goeke, S. J. Krieger, and D. Vautherin, *Nucl. Phys.* **A249** (1975), 215.
- [58] J. C. Slater, *Phys. Rev.* **81** (1951), 385.
- [59] K. Rutz, M. Bender, P.-G. Reinhard, and J. A. Maruhn, *Phys. Lett.* **B468** (1999), 1.
- [60] A. Sulaksono, T. Bürvenich, J. A. Maruhn, P.-G. Reinhard, and W. Greiner, *Ann. Phys. (N.Y.)* **308** (2003), 354.
- [61] K. W. Schmid and P.-G. Reinhard, *Nucl. Phys.* **A530** (1991), 283.
- [62] M. N. Butler, D. W. L. Sprung, and J. Martorell, *Nucl. Phys.* **A422** (1984), 157.
- [63] F. Barranco, R. A. Broglia, G. Gori, E. Vigezzi, P. F. Bortignon, and J. Terasaki, *Phys. Rev. Lett.* **83** (1999), 2147.
- [64] J. Terasaki, H. Flocard, P.-H. Heenen, and P. Bonche, *Phys. Rev. C* **55** (1997), 1231.

- [65] J. Dobaczewski, W. Nazarewicz, and P.-G. Reinhard, Nucl. Phys. **A693** (2001), 361.
- [66] J. Dechargé and D. Gogny, Phys. Rev. **C21** (1980), 1568.
- [67] P. Ring, Prog. Part. Nucl. Phys. **37** (1996), 193.
- [68] J. Błocki and H. Flocard, Nucl. Phys. **A273** (1976), 45.
- [69] T. Gonzalez-Llarena, J. L. Egido, G. A. Lalazissis, and P. Ring, Phys. Lett. **B379** (1996), 13.
- [70] J. Dobaczewski, H. Flocard, and J. Treiner, Nucl. Phys. **A422** (1984), 103.
- [71] P. Bonche, H. Flocard, P.-H. Heenen, S. J. Krieger, and M. S. Weiss, Nucl. Phys. **A443** (1985), 39.
- [72] S. J. Krieger, P. Bonche, H. Flocard, P. Quentin, and M. S. Weiss, Nucl. Phys. **A517** (1990), 275.
- [73] M. Bender, K. Rutz, P.-G. Reinhard, and J. A. Maruhn, Eur. Phys. J. **A8** (2000), 59.
- [74] M. Anguiano, J. L. Egido, and L. M. Robledo, Nucl. Phys. **A696** (2001), 467.
- [75] J. Dobaczewski and J. Dudek, Comput. Phys. Commun. **131** (2000), 164.
- [76] V. Blum, G. Lauritsch, J. A. Maruhn, and P.-G. Reinhard, J. Comput. Phys. **100** (1992), 364.
- [77] P.-G. Reinhard, Computational Nuclear Physics 1 – Nuclear Structure (K. Langanke, J. A. Maruhn, and S. E. Koonin, eds.), Springer, Berlin, Heidelberg, New York, 1991, p. 28.
- [78] K. Rutz, M. Bender, P.-G. Reinhard, J. A. Maruhn, and W. Greiner, Nucl. Phys. **A634** (1998), 67.
- [79] J. Friedrich and N. Vögler, Nucl. Phys. **A373** (1982), 192.
- [80] J. L. Friar and J. W. Negele, Adv. Nucl. Phys. **8** (1975), 219.
- [81] G. G. Simon, C. Schmitt, F. Borkowski, and V. H. Walther, Nucl. Phys. **A333** (1980), 381.
- [82] V. H. Walther, private communication, 1986.
- [83] P.-G. Reinhard, Phys. Lett. **A169** (1992), 281.
- [84] S. Mizutori, J. Dobaczewski, G. A. Lalazissis, W. Nazarewicz, and P.-G. Reinhard, Phys. Rev. C **61** (2000), 044326.
- [85] M. Samyn, S. Goriely, P.-H. Heenen, J. M. Pearson, and F. Tondeur, Nucl. Phys. **A700** (2002), 142.
- [86] W. Satuła, J. Dobaczewski, and W. Nazarewicz, Phys. Rev. Lett. **81** (1998), 3599.
- [87] E. Chabanat, P. Bonche, P. Haensel, J. Meyer, and R. Schaeffer, Nucl. Phys. **A635** (1998), 231, Nucl. Phys. **A643**, 441(E).
- [88] J. Friedrich and P.-G. Reinhard, Phys. Rev. C **33** (1986), 335.
- [89] W. Satuła, D. J. Dean, J. Gary, S. Mizutori, and W. Nazarewicz, Phys. Lett. **B407** (1997), 103.
- [90] J. Bartel, P. Quentin, M. Brack, C. Guet, and H.-B. Hakansson, Nucl. Phys. **A386** (1982), 79.

- [91] T. Bürvenich, D. Madland, J. A. Maruhn, and P.-G. Reinhard, Phys. Rev. C **65** (2002), 044308.
- [92] M. Rufa, P.-G. Reinhard, J. A. Maruhn, W. Greiner, and M. R. Strayer, Phys. Rev. C **38** (1988), 390.
- [93] G. A. Lalazissis, J. König, and P. Ring, Phys. Rev. C **55** (1997), 540.
- [94] P.-G. Reinhard, Rep. Prog. Phys. **52** (1989), 439.
- [95] Y. K. Gambhir, P. Ring, and A. Thimet, Ann. Phys. (NY) **198** (1990), 132.
- [96] P.-G. Reinhard, M. Bender, W. Nazarewicz, and T. Vertse, **73** (2006), 014309.
- [97] J. Boguta and A. R. Bodmer, Nucl. Phys. **A292** (1977), 413.
- [98] B. D. Serot and J. D. Walecka, Phys. Lett. **87B** (1979), 172.
- [99] ———, Adv. Nucl. Phys. **16** (1986), 1.
- [100] D. Vretenar, A.V. Afanasjev, G.A. Lalazissis, and P. Ring, Phys. Rep. **409** (2005), 101.
- [101] T. Hoch and P. Manakos, Z. Phys. **A337** (1990), 383.
- [102] S. Typel and H. H. Wolter, Nucl. Phys. **A656** (1999), 331.
- [103] F. Hofmann, C. M. Keil, and H. Lenske, Phys. Rev. C **64** (2001), 034314.
- [104] T. Niksic, D. Vretenar, G.A. Lalazissis, and P. Ring, Phys. Rev. C **69** (2004), 047301.
- [105] M. Thies, Nucl. Phys. **A460** (1986), 636.
- [106] D. Gogny, P. Pires, R. De, and Tourreil, Phys. Lett. **32B** (1970), 591.
- [107] M. Baldo, C. Maieron, P. Schuck, and X. Vinas, Nucl. Phys. A **736** (2004), 241.
- [108] J. P. Perdew, K. Burke, and M. Ernzerhof, Phys. Rev. Lett. **77** (1996), 3865.
- [109] L. G. Cao, U. Lombardo, C. W. Shen, and N. Van Giai, **73** (2006), 014313.
- [110] M. Serra, T. Otsuka, Y. Akaishi, P. Ring, and S. Hirose, Prog. Theor. Phys. **113** (2005), 1009.
- [111] J. Rong, Z.-Y. Ma, and N.V. Giai, Phys. Rev. C **73** (2006), 014614.
- [112] C. Maieron, M. Baldo, G. F. Burgio, and H. J. Schultze, Phys. Rev. **D70** (2004), 043010.
- [113] R. M. Aguirre and A. L. De Paoli, Phys. Rev. **C68** (2003), 055804.
- [114] J. O. Andersen and M. Strickland, Phys. Rev. **D66** (2002), 105001.
- [115] P. A. M. Guichon and A. W. Thomas, Phys. Rev. Lett. **93** (2004), 132502.
- [116] P. A. M. Guichon, K. Saito, E. N. Rodionov, and A. W. Thomas, Nucl. Phys. **A601** (1996), 349.
- [117] P. A. M. Guichon, H. H. Matevosyan, N. Sandulescu, and A. W. Thomas, arXiv:nucl-th/0603044 (2006).
- [118] M. Bender, K. Rutz, P.-G. Reinhard, J. A. Maruhn, and W. Greiner, Phys. Rev. C **60** (1999), 034304.

- [119] P. Pfeiffer, K. L. Kratz, F. K. Thielemann, and W. B. Walters, Nucl. Phys. **A688** (2001), 308.
- [120] B. Chen, J. Dobaczewski, K.-L. Kratz, K. Langanke, P. Pfeiffer, F.-K. Thielemann, and P. Vogel, Phys. Lett. **355B** (1995), 37.
- [121] M. Anselment, W. Faubel, S. Göring, A. Hanser, G. Meisel, H. Rebel, and G. Schatz, NPA **451** (1986), 471.
- [122] N. Tajima, P. Bonche, H. Flocard, P.-H. Heenen, and M. S. Weiss, Nucl. Phys. **A551** (1993), 434.
- [123] M. M. Sharma, G. A. Lalazissis, and P. Ring, Phys. Lett. **B317** (1993), 9.
- [124] M. M. Sharma, G. A. Lalazissis, J. König, and P. Ring, Phys. Rev. Lett. **74** (1995), 3744.
- [125] B. C. Clark and L. J. Kerr, Phys. Rev. E **68** (2003), 031204.
- [126] C. J. Batty, E. Friedman, H. J. Gils, and H. Rebel, Adv. Nucl. Phys. **19** (1989), 1.
- [127] B. A. Brown, Phys. Rev. Lett. **85** (2000), 5296.
- [128] S. Typel and B. A. Brown, Phys. Rev. C **64** (2001), 027302.
- [129] P.-G. Reinhard, Nucl. Phys. **A649** (1999), 305c.
- [130] D. Vretenar, N. Paar, T. Niksic, and P. Ring, Phys. Rev. Lett. **91** (2003), 2625021.
- [131] A. T. Kruppa, M. Bender, W. Nazarewicz, P.-G. Reinhard, T. Vertse, and S. Ówiok, Phys. Rev. C **61** (2000), 034313.
- [132] M. Bender, W. Nazarewicz, and P.-G. Reinhard, Phys. Lett. **515** (2001), 42.
- [133] H. J. Specht, Rev. Mod. Phys. **46** (1974), 773.
- [134] H. Flocard, P. Quentin, D. Vautherin, M. Vénéroni, and A. K. Kerman, Nucl. Phys. **A231** (1974), 176.
- [135] J.-F. Berger, M. Girod, and D. Gogny, Nucl. Phys. **A428** (1984), 23c.
- [136] V. Blum, J. A. Maruhn, P.-G. Reinhard, and W. Greiner, Phys. Lett. **323B** (1994), 262.
- [137] K. Rutz, J. A. Maruhn, P.-G. Reinhard, and W. Greiner, Nucl. Phys. **A590** (1995), 680.
- [138] M. Bender, K. Rutz, P.-G. Reinhard, and J. A. Maruhn, Eur. Phys. J. **A7** (2000), 467.
- [139] P.-G. Reinhard, Nucl. Phys. **A261** (1976), 291.
- [140] A. Mamdouh, J. M. Pearson, M. Rayet, and F. Tondeur, Nucl. Phys. **A644** (1998), 389.
- [141] T. Bürvenich, M. Bender, J.A. Maruhn, and P.-G. Reinhard, Phys. Rev. C **69** (2004), 014307.
- [142] M. Bender, private communication, 2004.
- [143] Yu. Ts. Oganessian et al., Phys. Rev. Lett. **83** (1999), 3154.
- [144] ———, Nature **400** (1999), 209.
- [145] ———, Phys. Rev. C **63** (2001), 011301(R).

- [146] J. W. Negele, Rev. Mod. Phys. **54** (1982), 913.
- [147] K. T. R. Davies, K. R. Sandhya Devi, S. E. Koonin, and M. R. Strayer, *TDHF calculations of heavy-ion collisions*, Treatise on Heavy-Ion Physics, Vol. 3 Compound System Phenomena (D. A. Bromley, ed.), Plenum Press, New York, 1985, p. 3.
- [148] G. Colo, Nguyen Van Giai, and H. Sagawa, Phys. Lett. **363B** (1995), 5.
- [149] J. P. Blaizot, D. Gogny, and B. Grammaticos, Nucl. Phys. **A265** (1976), 315.
- [150] J. P. Blaizot and D. Gogny, Nucl. Phys. **A284** (1977), 429.
- [151] Z.-Y. Ma, Nguyen Van Giai, A. Wandelt, D. Vretenar, and P. Ring, Nucl. Phys. **A686** (2001), 173.
- [152] P. Ring, Zhong-Yu Ma, Nguyen Van Giai, D. Vretenar, A. Wandelt, and Li-Gang Cao, Nucl. Phys. **A694** (2001), 249.
- [153] G. F. Bertsch, P. F. Bortignon, and R. A. Broglia, Rev. Mod. Phys. **55** (1983), 287.
- [154] P.-G. Reinhard, H. L. Yadav, and C. Toepffer, Nucl. Phys. **A458** (1986), 301.
- [155] J.A. Maruhn, P.-G. Reinhard, P. Stevenson, I. Stone, and M.R. Strayer, Phys. Rev. C **71** (2005), 064328.
- [156] D. Vretenar, N. Paar, P. Ring, and G. A. Lalazissis, Phys. Rev. C **63** (2001), 047301.
- [157] P.-G. Reinhard and Y. K. Gambhir, Ann. Phys. (Leipzig) **1** (1992), 598.
- [158] P.-G. Reinhard, Ann. Phys. (Leipzig) **1** (1992), 632.
- [159] P.-G. Reinhard and J. Friedrich, Z. Phys. A **321** (1985), 619.
- [160] M. Brack, Phys. Lett. **123B** (1983), 143.
- [161] D. Bohle, A. Richter, W. Steffen, A. E. L. Dieperink, N. Lo Iudice, F. Palumbo, and O. Scholten, Phys. Lett. **B137** (1984), 27.
- [162] N. Lo Iudice, Prog. Part. Nucl. Phys. **28** (1997), 556.
- [163] F. Osterfeld, Rev. Mod. Phys. **64** (1992), 491.
- [164] K. Langanke, G. Martinez-Pinedo, J. M. Sampaio, D. J. Dean, W. R. Hix, O. E. B. Messer, A. Mezzacappa, H. T. Janka M. Liebendorf, and M. Rampp, Phys. Rev. Lett. **90** (2003), 241102.
- [165] W. R. Hix, O. E. B. Messer, A. Mezzacappa, M. Liebendorf, J. M. Sampaio, K. Langanke, G. Martinez-Pinedo, and D. J. Dean, Phys. Rev. Lett. **91** (2003), 201102.
- [166] M. Bender, J. Dobaczewski, J. Engel, and W. Nazarewicz, Phys. Rev. C **65** (2002), 054322.
- [167] Nguyen Van Giai and H. Sagawa, Phys. Lett. **106B** (1981), 379.
- [168] J. Engel, M. Bender, J. Dobaczewski, W. Nazarewicz, and R. Surman, Phys. Rev. C **60** (1999), 014302.
- [169] N. Paar, T. Niksic, T. Marketin, D. Vretenar, and P. Ring, Eur. Phys. J. A **25** (2005), 531.

- [170] S.-J. Lee, A. S. Umar, K. T. R. Davies, M. R. Strayer, and P.-G. Reinhard, Phys. Lett. **196B** (1987), 419.
- [171] P.-G. Reinhard, A. S. Umar, K. T. R. Davies, M. R. Strayer, and J.-S. Lee, Phys. Rev. **C37** (1988), 1026.
- [172] Y. Abe, S. Ayik, P.-G. Reinhard, and E. Suraud, Phys. Rep. **275** (1996), 49.
- [173] A.S. Umar and V.E. Oberacker, preprint arXiv:nucl-th/0603038, 2006.
- [174] R. V. F. Janssens and Teng Lek Khoo, Annual Review of Nuclear and Particle Science **41** (1991), 321.
- [175] C. Baktash, B. Haas, and W. Nazarewicz, Annual Review of Nuclear and Particle Science **45** (1995), 485.
- [176] X.-L. Han and C.-L. Wu, At. Data Nucl. Data Tables **73** (1999), 43.
- [177] J. Fleckner, U. Mosel, P. Ring, and H.-J. Mang, Nucl. Phys. **A331** (1979), 288.
- [178] A. V. Afanasjev, D. B. Fossan, G. J. Lane, and I. Ragnarsson, Phys. Rep. **322** (1999), 1.
- [179] S. Frauendorf, Rev. Mod. Phys. **73** (2001), 463.
- [180] A. V. Afanasjev, J. König, and P. Ring, Nucl. Phys. **A 608** (1996), 107.
- [181] F. K. Thielemann et al., Prog. Part. Nucl. Phys **46** (2001), 5.
- [182] K. L. Kratz, P. Moller, and B. Pfeiffer, ApJ **403** (1993), 216.
- [183] K. L. Kratz, F. K. Thielemann, W. Hillebrandt, P. Moller, V. Harms, A. Wöhr, and J. W. Truran, J. Phys. G:Nucl. Phys. Supl **14** (1988), S331.
- [184] Y. Aboussir, J. M. Pearson, A. K. Dutta, and F. Tondeur, At. Data Nucl. Data Tables **61** (1995), 127.
- [185] J. M. Pearson et al., Phys. Lett. **B387** (1996), 455.
- [186] F. Tondeur, S. Goriely, J. M. Pearson, and M. Onsi, Phys. Rev. **C62** (2000), 024308.
- [187] S. Goriely, F. Tondeur, and J. M. Pearson, At. Data Nucl. Data Tables **77** (2001), 311.
- [188] M. Samyn, S. Goriely, M. Bender, and J. M. Pearson, At. Data Nucl. Data Tables **77** (2001), 311.
- [189] S. Goriely, M. Samyn, J. M. Pearson, and M. Onsi, Nucl. Phys. **A750** (2005), 425.
- [190] J. Rikowska Stone, J. Phys. G **31** (2005), R211.
- [191] G. Audi and A. H. Wapstra, Nucl. Phys. **A595** (1995), 409.
- [192] K. L. Kratz and B. Pfeiffer, private communication (2006).
- [193] K. L. Kratz, Nuclear Physics Issues of r-Process Nucleosynthesis, AIP Conf. Proc. 819, 2006, p. 409.
- [194] J. Engel, M. Bender, J. Dobaczewski, W. Nazarewicz, and R. Surman, Phys. Rev. **C60** (1999), 014302.

- [195] J. Dobaczewski and J. Dudek, Phys. Rev. **C52** (1995), 1827.
- [196] P. Moller and J. Randrup, Nucl. Phys. **A514** (1990), 1.
- [197] I. N. Borzov, S. A. Fayans, E. Krömer, and D. Zawischa, Nucl. Phys. **A621** (1997), 307c.
- [198] B. Chen, J. Dobaczewski, K. L. Kratz, K. Langanke, B. Pfeiffer, F. K. Thielemann, and P. Vogel, Phys. Lett. **355** (1995), 37.
- [199] R. K. Wallace and S. E. Woosley, Astrophys. J. Supplement **45** (1981), 389.
- [200] H. Schatz et al., Phys. Rep. **294** (1998), 167.
- [201] H. Schatz, L. Bildsten, A. Cumming, and M. Wiescher, ApJ **524** (1999), 1014.
- [202] B. A. Brown, R. R. C. Clement, H. Schatz, A. Volya, and W. A. Richter, Phys. Rev. **C65** (2002), 045802.
- [203] B. A. Brown, W. A. Richter, and R. Lindsay, Phys. Lett. **B483** (2000), 49.
- [204] M. Baranger and M. Vénéroni, Ann. Phys. (NY) **114** (1978), 123.
- [205] K. Goeke and P.-G. Reinhard, Ann. Phys. (NY) **112** (1978), 328.
- [206] P. Bonche, J. Dobaczewski, H. Flocard, P.-H. Heenen, and J. Meyer, Nucl. Phys. **A510** (1990), 466.
- [207] W. Greiner and J. A. Maruhn, *Kernmodelle*, Theoretische Physik, vol. 11, Verl. Harri Deutsch, Thun, Frankfurt am Main, 1995.
- [208] J. Skalski, P.-H. Heenen, P. Bonche, H. Flocard, and J. Meyer, Nucl. Phys. **A551** (1993), 109.
- [209] T. Radon, H. Geissel, G. Münzenberg, B. Franzke, Th. Kerscher, F. Nolden, Yu. N. Novikov, Z. Patyk, C. Scheidenberger, F. Attallah, K. Beckert, T. Beha, F. Bosch, H. Eickhoff, M. Falch, Y. Fujita, M. Hausmann, F. Herfurth, H. Irnich, H. C. Jung, O. Klepper, C. Kozhuharov, Yu. A. Litvinov, K. E. G. Löbner, F. Nickel, H. Reich, W. Schwab, B. Schlitt, M. Steck, K. Sümmerer, T. Winkler, and H. Wollnik, Nucl. Phys. A **677** (2000), 75.
- [210] E. W. Otten, *Nuclear radii and moments of unstable isotopes*, Treatise on Heavy-Ion Science (D. A. Bromley, ed.), vol. VIII, Plenum Press, New York and London, 1989, p. 517.
- [211] M. Girod and P.-G. Reinhard, Nucl. Phys. **A384** (1982), 179.
- [212] P. Bonche, J. Dobaczewski, H. Flocard, and P.-H. Heenen, Nucl. Phys. **A530** (1991), 149.
- [213] P. Fleischer, P. Klüpfel, T. Cornelius, T.J. Bürvenich, S. Schramm, J.A. Maruhn, and P.-G. Reinhard, Eur. Phys. J. A **22** (2004), 363.
- [214] M. Bender, T. Cornelius, G.A. Lalazissis, J. A. Maruhn, W. Nazarewicz, and P.-G. Reinhard, Eur. Phys. J. A **14** (2002), 23.
- [215] R. R. Rodriguez-Guzmán, J. L. Egido, and L. M. Robledo, Phys. Rev. C **62** (2000), 054319.
- [216] P.-H. Heenen, P. Bonche, J. Dobaczewski, and H. Flocard, Nucl. Phys. **A561** (1993), 367.
- [217] P. Fleischer, P. Klüpfel, P.-G. Reinhard, and J. A. Maruhn, Phys. Rev. C **70** (2004), 054321.

- [218] P.-H. Heenen, J. Skalski, P. Bonche, and H. Flocard, *Phys. Rev. C* **50** (1994), 802.
- [219] P.-G. Reinhard, F. Grümmer, and K. Goeke, *Z. Phys.* **A317** (1984), 339.
- [220] A. Akmal, V. R. Pandharipande, and D. G. Ravenhall, *Phys. Rev.* **C58** (1998), 1804.
- [221] H. Heiselberg and M. Hjorth-Jensen, *Phys. Rep.* **328** (2000), 328.
- [222] J. M. Lattimer and M. Prakash, *Phys. Rep.* **334** (2000), 121.
- [223] H. Heiselberg and V. Pandharipande, *Annual Review of Nuclear and Particle Science* **50** (2000), 481.
- [224] J. R. Stone, *Open Issues in Understanding of Core-Collapse Supernova Theory* (A. Mezzacappa and G. M. Fuller, eds.), World Scientific, 2006, p. 318.
- [225] E. Chabanat, P. Bonche, P. Hansel, J. Meyer, and R. Schaeffer, *Nucl. Phys.* **A627** (1997), 710.
- [226] C. Mahaux and R. Sartor, *Nuclear matter and Heavy Ion Collisions* (M. Soyeur et al, ed.), NATO ASI Series B: Physics, Vol 205, 1989, p. 1.
- [227] J. R. Nix and P. Moller, *Exotic Nuclei and Atomic Masses* (M. de Saint Simon and O. Sorlin, eds.), Editions Frontieres Gif-sur-Yvette, 1995, p. 1.
- [228] J. P. Blaizot, *Phys. Rep.* **64** (1980), 171.
- [229] J. Meyer P. Gleissl, M. Brack and P. Quentin, *Ann. Phys. (NY)* **197** (1990), 205.
- [230] J. Decharge J. P. Blaizot, J. F. Berger and M. Girod, *Nucl. Phys.* **A591** (1995), 435.
- [231] J. M. Pearson M. Farine and F. Tondeur, *Nucl. Phys.* **A615** (1997), 135.
- [232] W. J. Swiatecki P. Moller, W. D. Meyers and J. Treiner, *At. Data Nucl. Data Tables* **59** (1995), 225.
- [233] C. M. Ko Bao-An Li and Z. Ren, *Phys. Rev. Lett.* **78** (1997), 1644.
- [234] N. K. Glendenning, *Compact Stars*, Springer, Berlin, Heidelberg, New York, 2000.
- [235] M. Farine, J. M. Pearson, and F. Tondeur, *Nucl. Phys.* **A696** (2001), 396.
- [236] W. D. Myers and W. Światecki, *Phys. Rev. C* **57** (1998), 3020.
- [237] O. Bohigas, A. M. Lane, and J. Martorell, *Phys. Rep.* **51** (1979), 267.
- [238] E. Chabanat, P. Bonche, P. Haensel, J. Meyer, and R. Schaeffer, *Nucl. Phys.* **A627** (1997), 710.
- [239] J. D. Walecka, *Ann. Phys. (N.Y.)* **83** (1974), 497.
- [240] J. Rikowska Stone, P. D. Stevenson, J. C. Miller, and M. R. Strayer, *Phys. Rev.* **C65** (2002), 064213.
- [241] C. P. Lorentz, D. G. Ravenhall, and C. J. Pethick, *Phys. Rev. Lett.* **70** (1993), 379.
- [242] G. Baym, C. Pethick, and P. Sutherland, *ApJ* **170** (1977), 299.
- [243] W. D. Arnett and R. L. Bowers, *Astrophys. J. Supplement* **33** (1977), 415.

- [244] V. R. Pandharipande, Nucl. Phys. **A178** (1971), 123.
- [245] S. Balberg, I. Lichtenstadt, and G. B. Cook, Astrophys. J. Supplement **121** (1999), 515.
- [246] R. B. Wiringa, Rev. Mod. Phys. **65** (1993), 231.
- [247] F. Hofmann, C. M. Keil, and H. Lenske, Phys. Rev. **C64** (2001), 025804.
- [248] K. Iida and K. Sato, Phys. Rev. **C58** (1998), 2538.
- [249] G. F. Burgio, P. K. Sahu M. Baldo, and H. J. Schulze, Phys. Rev. **C66** (2002), 025802.
- [250] D. P. Menezes and C. Providencia, Phys. Rev. **C68** (2003), 035804.
- [251] G. Baym, H. Bethe, and C. Pethick, Nucl. Phys. **A175** (1971), 225.
- [252] G. Baym, C. Pethick, and P. Sunderland, ApJ **170** (1971), 299.
- [253] H. A. Bethe and M. B. Johnson, Nucl. Phys. **A230** (1974), 1.
- [254] J. M. Lattimer and M. Prakash, Phys. Rev. Lett. **94** (2005), 111101.
- [255] D. J. Nice, E. M. Splaver, I. H. Stairs, O. Löhmer, A. Jessner, M. Kramer, and J. M. Cordes, ApJ **634** (2005), 1242.
- [256] R. C. Tolman, Proc. Natl. Acad. Sci. USA **20** (1934), 3.
- [257] J. R. Oppenheimer and G. M. Volkov, Phys. Rev. **55** (1939), 374.
- [258] R. Schaffer, Y. Declais, and S. Julian, Nature **300** (1987), 142.
- [259] B. Friedman and V. R. Pandharipande, Nucl. Phys. **A361** (1981), 502.
- [260] J. M. Lattimer and B. F. Schultz, ApJ **629** (2005), 979.
- [261] Ph. Podsiadlowski, J. D. M. Dewi, P. Lesaffre, J. C. Miller, W. G. Newton, and J. R. Stone, Mon. Not. R. Astron. Soc. **361** (2005), 1243.
- [262] D. Page, J. M. Lattimer, M. Prakash, and A. W. Steiner, The Astrophysical Journal, Supplement **155** (2004), 623.
- [263] P. B. Jones, Phys. Rev. **D64** (2001), 084003.
- [264] C. J. Pethick, Rev. Mod. Phys. **64** (1992), 1133.
- [265] M. Prakash, M. Prakash, J. M. Lattimer, and C. J. Pethick, Astrophys. J. Lett. **390** (1992), L77.
- [266] M. Prakash, Physics Reports **242** (1994), 191.
- [267] S. Popov, H. Grigorian, R. Turolla, and D. Blaschke, Astrom. and Astrophys. **448** (2006), 327.
- [268] T. Klähn et al., arXiv:nucl-th/0602038 (2006).
- [269] J. Fletcher, J. R. Stone, and J. C. Miller, in preparation.
- [270] A. Rios, A. Polls, and I. Vidana, Phys. Rev. **C71** (2005), 055802.
- [271] J. Margueron, J. Navarro, and Nguyen Van Gai, Phys. Rev. **C66** (2002), 014303.

- [272] K. Oyamatsu, Nucl. Phys. **A561** (1993), 431.
- [273] P. Magierski and P. H. Heenen, Phys. Rev. **65** (2002), 045804.
- [274] H. A. Bethe, G. Börner, and K. Sato, Astron. Astrophys. **7** (1970), 279.
- [275] D. Q. Lamb, J. M. Lattimer, C. J. Pethick, and D. G. Ravenhall, Phys. Rev. Lett. **41** (1978), 1623.
- [276] J. M. Lattimer, C. J. Pethick, D. G. Ravenhall, and D. Q. Lamb, Nucl. Phys. **A432** (1985), 646.
- [277] J. M. Lattimer and F. D. Swesty, Nucl. Phys. **A535** (1991), 331.
- [278] C. J. Pethick, D. G. Ravenhall, and C. P. Lorenz, Nucl. Phys. **A584** (1995), 675.
- [279] P. Bonche and D. Vautherin, Nucl. Phys. **A372** (1981), 496.
- [280] W. Hillebrandt and R. G. Wolff, Nucleosynthesis:Challenges and New Developments (D. Arnett and J. W. Truran, eds.), Univ. Chicago Press, 1985, p. 131.
- [281] J. Heyer, T. T. S. Kuo, J. P. Shen, and S. S. Wu, Physics Letters **B202** (1988), 465.
- [282] J. Ventura, A. Polls, and et al., Nucl. Phys. **A545** (1992), 247.
- [283] M. Onsi, H. Przysieznik, and J. M. Pearson, Phys. Rev. **C55** (1997), 3139.
- [284] ———, Phys. Rev. **C50** (1994), 460.
- [285] H. Shen, H. Toki, K. Oyamatsu, and K. Sumiوشي, Nucl. Phys. **A637** (1998), 435.
- [286] A. Mezzacappa, Annual Review of Nuclear and Particle Science **55** (2005), 467.
- [287] W. G. Newton, DPhil Thesis, Oxford University (2006).
- [288] H. T. Janka, R. Buras, K. Kifonidis, A. Marek, and M. Rampp, Proceedings IAU Coll. Vol. 192 (J. M. Marcaide and K. W. Weiler, eds.), Springer Verlag, 2003.